JYU DISSERTATIONS 823

Cliona Shakespeare

Seeing the Light

Towards Optical Readout
of Donor Spins in Silicon

UNIVERSITY OF JYVÄSKYLÄ
FACULTY OF MATHEMATICS
AND SCIENCE

JYU DISSERTATIONS 823

Cliona Shakespeare

Seeing the Light

Towards Optical Readout of Donor Spins in Silicon

Esitetään Jyväskylän yliopiston matemaattis-luonnontieteellisen tiedekunnan suostumuksella
julkisesti tarkastettavaksi yliopiston Ylistönrinteen salissa FYS1
syyskuun 20. päivänä 2024 kello 12.

Academic dissertation to be publicly discussed, by permission of
the Faculty of Mathematics and Science of the University of Jyväskylä,
in Ylistönrinne, auditorium FYS1, on September 20, 2024 at 12 o'clock noon.

JYVÄSKYLÄN YLIOPISTO
UNIVERSITY OF JYVÄSKYLÄ

JYVÄSKYLÄ 2024

Editors
Ilari Maasilta
Department of Physics, University of Jyväskylä
Ville Korkiakangas
Open Science Centre, University of Jyväskylä

ISBN 978-952-86-0290-3 (PDF)
URN:ISBN:978-952-86-0290-3
ISSN 2489-9003

Permanent link to this publication: http://urn.fi/URN:ISBN:978-952-86-0290-3

ABSTRACT

Shakespeare, Cliona
Seeing the Light: Towards Optical Readout of Donor Spins in Silicon

Quantum computation is a rapidly growing field with multiple functional proof of concept devices. As none of them have shown a provable advantage over classical systems, however, there is ample room for investigation of alternate platforms. One such possible platform is a donor spin in Si, which has been demonstrated to have long coherence times and high control fidelities, as well as having a large pre-existing manufacturing base. Its chief drawback is a lack of a convenient readout and coupling mechanism. We aim to solve this by introducing optical coupling via an optomechanical quantum bus, where the spin state is coupled to an optomechanical resonator, the mechanical resonance frequency of which is affected by the spin state and is also optically observable.

To accomplish this, we have investigated how our optomechanical system of choice is affected by a number of factors necessary for the functioning of the system. We investigated the effect of amorphisation caused by ion implantation on the optical and mechanical resonances and confirmed that a post-implantation anneal will recover the desired behavior. We also confirmed that the optical resonance will survive in presence of a micromagnet, in place for improved coupling of spins to mechanics. As the readout involves incident illumination and thus absorption, we additionally investigated the magnitude of photothermal effects as a function of incident power.

In this thesis, I also present the necessary theoretical background on optomechanics, both radiation pressure and photothermal, and the spin picture, from the basics of a two-level system to the dressing required to couple our spins to the mechanics. Finally, I discuss the design of the optomechanical device and its fabrication, including common failure states and steps I took to avoid them.

This dissertation is composed of an introductory text and three publications — one of which has been published, one of which is submitted for publication, and one of which is a manuscript that will soon be submitted.

Keywords: optomechanics, quantum computing, optics, nanoscale physics, quantum physics

TIIVISTELMÄ (ABSTRACT IN FINNISH)

Shakespeare, Cliona
Valoa näkyvissä: Kohti donorispinien optista uloslukua piissä

Kvanttilaskenta on nopeasti kasvava ala, jolla on useita toimivia pieniä kvanttitietokoneita. Koska yksikään niistä ei ole kuitenkaan osoittanut pystyvänsä johonkin, mihin klassinen tietokone ei pysty, on tilaa tarkastella vaihtoehtoisia toteutusmalleja. Eräs sellainen on donorispini piissä, jolla on tutkitusti pitkä koherenssiaika ja korkea kontrollifideliteetti, sekä valmiiksi löytyvä suuri valmistuskapasiteetti. Sen huonoin puoli on kätevien luenta- ja kytkentämekanismien puute. Pyrimme ratkaisemaan tämän toteuttamallä optisen kytkennän optomekaanisen kvanttiväylän kautta, jossa spinin tila on kytketty optomekaaniseen resonaattoriin, jonka mekaaninen resonanssitaajuus riippuu spinin tilasta ja on optisesti mitattavissa.

Saadaksemme tämän aikaan olemme tutkineet, miten jotkin koko systeemimme toimivuudelle välttämättömät tekijät vaikuttavat valitsemamme optomekaaniseen systeemiin. Tutkimme ioni-implantaation aiheuttaman amorfisaation vaikutuksia optiseen ja mekaaniseen resonanssiin ja varmistimme, että implantaation jälkeinen hehkutus palauttaa toivotun käytöksen. Varmistimme myös, että optinen resonanssi säilyy paremman spini-mekaniikka -kytkennän tuovan mikromagneetinkin kanssa. Koska ulosluku vaatii sisääntulevaa säteilyä ja siten absorptiota, tutkimme lisäksi, miten fototermisen voiman suuruus riippui sisääntulevasta tehosta.

Tässä väitöskirjassa esittelen myös tarvittavan teoreettisen taustan sekä säteilypaine- että fototermisestä optomekaniikasta ja spinikuvasta kaksitilasysteemin perusteista spinit mekaniikkaan kytkevään dressaukseen. Viimeiseksi käsittelen optomekaanisen resonaattorimme (design) ja valmistusta, mukaanlukien yleisiä epäonnistumisia ja mitä tein välttääkseni ne.

Tämä väitöskirja koostuu johdanto-osiosta ja kolmesta julkaisusta, joista yksi on jo julkaistu, yksi on lähetetty, ja yksi on manuskripti, joka lähetetään kohta lehteen.

Avainsanat: optomekaniikka, kvanttilaskenta, optiikka, nanofysiikka, kvanttifysiikka

Author
Cliona Shakespeare
Department of Physics and Nanoscience Center
University of Jyväskylä
Finland

Supervisors
Prof. Juha Muhonen
Department of Physics and Nanoscience Center
University of Jyväskylä
Finland

Reviewers
Assist. Prof. Bas Hensen
Leiden Institute of Physics
Leiden University
Netherlands

Prof. Mika Sillanpää
Centre of Excellence in Quantum Technology
Department of Applied Physics
Aalto University
Finland

Opponent
Prof. Ralf Riedinger
Institute for Quangum Physics
University of Hamburg
Germany

PREFACE

I wish to thank my supervisor, professor Juha Muhonen and my esteemed opponent, prof. Ralf Riedinger, as well as the pre-examiners of the thesis, prof. Bas Hensen and prof. Mika Sillanpää.

When I moved to Jyväskylä in January 2019 and started at the Nanoscience Center the month after, all that greeted me in the lab was a PI, an empty optical table, and various RF components inherited from the depths of the past. Even the cryostat only arrived in June. Now, five years later, I shall leave behind me a group with multiple members and a lab with three optical table setups, two associated with a cryostat and one with a vacuum chamber. During this time I have also acquired a black belt in Shorinji Kempo and lost all my grandparents and also my father. Unrelatedly, there was also a global pandemic.

Nonetheless, I have enjoyed my time in Jyväskylä, filled with uninvited events global and personal though it has been. The city is nice and compact, very friendly to biking, and the one city in Finland that has a lighting designer, leading to beautifully mood-lit roads and bicycle paths. Many a night have I sat entranced, watching the blue and orange lights of the Kuokkala bridge reflected on the black water.

My stay in the NSC has also been excellent, bifurcated by the pandemic though it has been. For that, I have to thank my group mates past and present, Henri, Charles, Arvind, Teemu, Harsh, Milla, Antti, and Simeoni, as well as my other colleagues at the NSC current and former, amongst them Johanna, Henna, Amar, Laura, Kalle, and Lars. On the academic side, I wish to thank our collaborators in the Netherlands and Australia: prof. Ewold Verhagen's group at AMOLF, especially Jesse Slim, and prof. Andrea Morello and prof. Jarryd Pla's groups at UNSW, especially James Slack-Smith.

Jyväskylä, June 2024

Cliona Shakespeare

LIST OF INCLUDED ARTICLES

PI Cliona Shakespeare, Teemu Loippo, Henri Lyyra and Juha T Muhonen *The effects of ion implantation damage to photonic crystal optomechanical resonators in silicon*. Materials for Quantum Technology **1** 045003 2021.

PII Cliona Shakespeare, Arvind S. Kumar and Juha T Muhonen *Thermal relaxation time and photothermal optomechanical force in sliced photonic crystal silicon nanobeams*. Manuscript (2024).

PIII Henri Lyyra, Cliona Shakespeare, Simeoni Ahopelto, Teemu Loippo, Reetu Inkilä, Pyry Runko, and Juha Muhonen *Optomechanical quantum bus for donor spins in silicon*. Manuscript (2024).

Author’s contribution

I performed the data analysis and half of the measurements for [**PI**], all the measurements and the simulations for [**PII**], and the magnet sample fabrication and data analysis for the optomechanical measurements for Section V of [**PIII**]. I participated in the writing of the text for all publications.

LIST OF FIGURES

CONTENTS

1 INTRODUCTION

The first quantum revolution was born of the realization that a wave is also a particle and a particle a wave, and heralded the advent of technologies that underpin present-day civilization [1]. Realizing that an electron is also a wave gave us tunneling and thus both a limit to current transistor geometry and a new transistor paradigm [2]; realizing that light is also a particle gave us the laser [3, 4] and thus a plethora of applications from telecommunications [5] to dentistry [6]. This, however, was merely the vanguard of a new physics. The quantum regime contains ground that is yet to be conquered [7].

The network of information technology that encircles the globe and enables a plethora of things — such as the writing of this very thesis — is based on the humble bit. It is a binary system that is on or off, up or down, and by manipulation of collections of those bits, humankind has touched the Moon [8] and simulated the interactions of subatomic particles [9]. Yet while these classical bits are excellent for many sorts of algorithm, they have their limitations. Humankind has been placing more and more bits on each square millimeter of silicon chip, but eventually, the size of the electron and its propensity to tunnel out of its desired bounds will draw this development to a halt [2].

Enter the quantum architecture. A quantum bit, or qubit, is not merely an on/off signal one can think of as an arrow that points up or down, depending on whether the signal is on or off. Instead, it is an arrow that can point not only up or down, but in all possible directions, including directly to the side, as a superposition of up and down. With this new medium of computation, certain things become algorithmically easier: simulations of the quantum world, of course [10], but also the factorization of large numbers [11] and searching databases [12] or linked trees [13].

As of 2024, quantum computing is in its infancy. Several proof of concept systems have been built, but none so far have unambiguously demonstrated an advantage over extant classical systems. One of the limitations is geometric: current classical systems use the presence or absence of an electrical signal as the states of their bit. These electrical signals can then easily be routed towards and away from each other, making interactions between any two bits easy to arrange.

Transporting quantum data, on the other hand, is significantly harder, so currently only qubits physically adjacent to each other can interact, limiting system scalability. Current frontrunners for qubit architecture also involve millikelvin temperatures or fabrication processes with low yields.

The ideal qubit, then, would be something that piggybacks off the ready-made fabrication solutions of yesteryear as far as possible to enable rapid scale-up and quick integration with extant technology. Our proposal is to take advantage of the honed fabrication technologies of the semiconductor and chip industries and make a qubit out of doped silicon. One of the common dopants in the semiconductor industry is phosphorus, whose surplus electron acts as a donor spin with an excellent coherence time when embedded in a Si lattice [14]. Alas, P and other V-group donors do not have any optical transitions in Si, which means non-contact readout and optical manipulation are not available, unlike for *e.g.* the competing platform of nitrogen vacancy centers in diamond [15, 16], which can be controlled wholly through optics [17, 18]. Extant readout methods for donor spins in Si are limited to single electron transistors [19, 20], which require precision microfabrication that has yet to be replicated by other research groups. Other extant platforms for spin state detection are the Auger decay signal from excitons [21, 22] and single lead quantum dots [23]. All of these are electrically based detection schemes that require electrical (or galvanic) contact between the sample and the outside world.

Our proposal is to leave out the electrical cables to the sample and instead manufacture an optical readout. We sidestep the lack of intrinsic optical coupling by coupling the spin state coherently to something that does couple to light. This chain-style coupling additionally enables us to set our optical readout frequency at the telecom wavelength of 1550 nm to readily transport information across the globe. The means of coupling chosen herein is optomechanics, where we couple the mechanical system to the spin state, through which the information is transmitted to the optical system and thence to the wider world.

Stated above is the motivation behind the work presented herein. While the end goal is still unachieved, I present several articles published on the pathway towards our quantum bit. The first, **[PI]**, is on the effects of ion implantation damage on the optomechanical resonator. The second, **[PII]**, deals with photothermal forces that come from the absorption of photons in the optical cavity, and connects experimental observations with Monte Carlo simulations of phonon exit times in an effort to quantify the photothermal effect on our optomechanical resonators. The third, **[PIII]**, focuses on the coupling of donor spin qubits to the mechanical motion of an optomechanical resonator, including two different means of doing so, strain and micromagnets, and how the micromagnets affect the optical cavity mode.

Before the articles at the end, I expand upon the theoretical background of the work. The first chapter is on cavity optomechanics, which is what allows us optical readout of a mechanical state. For thoroughness and greater clarity, I have chosen to include intermediate steps in the derivation of formulae. The second chapter begins with a brief introduction to two-level systems before talking of the preparation of the spin state and coupling it to mechanics. Finally, as the path from idea to industry requires the creation of a functional device, I conclude with a section on fabrication so as to document some of the potential pitfalls an experimentalist might encounter. I also talk about the design process of the magnets and nanobeams and the tradeoffs we have chosen to make in the design of our devices.

2 CAVITY OPTOMECHANICS

That light could exert a force on matter was first postulated by Kepler in the 17th century [24]. Five centuries of scientific progress later, optomechanics is a thriving field and the principle of coupling an optical cavity to a mechanical resonator — cavity optomechanics — is what underlies all three articles included in this thesis. An optomechanical device is the bridge with which we connect the state of the spin qubit with the optical readout. Article [**PI**] is concerned with the effects of ion implantation, necessary for introduction of spin qubits, on this bridge, while article [**PII**] discusses the effects of heating due to photon absorption. Article [**PIII**] includes a brief investigation of the effects of a micromagnet, another aspect necessary for our readout, on the optomechanical device. Here I introduce the principles behind the bond of mechanical motion and light that defines any optomechanical device, as well as briefly discussing the device type of our choice.

2.1 Radiation pressure force

Light, massless though it may be, carries momentum [25]. The transferrance of this momentum to an illuminated object is known as the radiation pressure force.

Let us begin with an optical cavity consisting of two semipermeable mirrors at distance L from each other. As the momentum of a photon is h/λ, when it reflects off a mirror, it gives the mirror a momentum of $2h/\lambda$ [26]. For a fixed mirror, that is that; for a freely moving mirror like a solar sail [27], the mirror will slowly head off into the void between the stars. If, however, the mirror is on the surface of a mechanical oscillator (*e.g.* a diaphragm) or otherwise spring coupled to an unperturbed location, the initial displacement will make it oscillate. A schematic of this can be seen in Figure 1. One can think of this as a cavity that changes its own length. For an unperturbed optical cavity, the resonance frequency directly depends on the cavity length L, so that the resonance wavelength $\lambda = 2L$ for the fundamental mode. A periodic change in the length of the cavity will thus also change the resonance frequency. This will show up as phase noise in the optical resonance frequency [28].

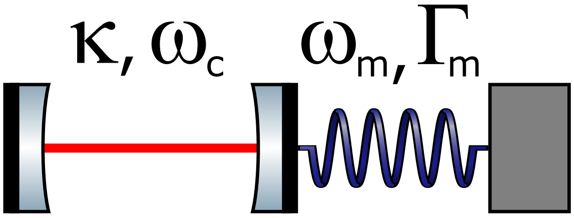

FIGURE 1 A schematic view of an optomechanical resonator.

2.1.1 The Hamiltonian

Now let us consider the Hamiltonian of an optomechanical cavity. This consists of three parts: the term for the optical cavity, the term for the mechanical cavity, and the term for the interaction between them. The optical term is simply the number of photons in the optical cavity n times the energy per photon $\hbar\omega_c$:

$$H_L = \hbar\omega_c n \tag{1}$$

The subscript c will be used throughout to describe the optical cavity, as o would be confused with 0 and L will henceforth be reserved for the incident field. ω_c is thus the resonance frequency of the optical cavity.

On the mechanical side, we can imagine our system as a mass m spring coupled to a location with a spring constant k. A displacement causes an increase in potential energy due to the deformation of the spring, which is then transformed into kinetic energy as the mass returns towards its neutral position. This energy is then again transformed into kinetic energy as the mass overshoots, leading to oscillations at a frequency of $\omega_m = \sqrt{k/m}$. In the absence of an optomechanical coupling, the Hamiltonian for this mechanical system is

$$H_M = \frac{p^2}{2m} + \frac{m\omega_m^2}{2}x^2 \tag{2}$$

where p, m, and x are the mechanical resonator's momentum, mass, and displacement, respectively, and ω_m is the resonance frequency of the mechanical resonator. The subscript m will be dedicated for the mechanical resonator throughout.

The optomechanical coupling term comes from the change in potential energy of the mechanical resonator caused by the optical field. Each photon exerts a force of $F = \hbar\frac{d\omega_c}{dx}$. The interaction Hamiltonian is thus

$$H_{OM} = \hbar G x n \tag{3}$$

where we have defined the optical frequency shift per displacement $G = \frac{d\omega_c}{dx}$.

Moving to the quantum picture, we introduce the raising and lowering operators for the optical field, $\hat{a}^\dagger$ and $\hat{a}$, and mechanical field, $\hat{b}^\dagger$ and $\hat{b}$. As a reminder, $\hat{b}^\dagger\hat{b}$ is the number operator for the field, the position operator is

$\hat{x} = x_{ZPF}(\hat{b} + \hat{b}^{\dagger})$, and the momentum operator is $\hat{p} = -im\omega_m x_{ZPF}(\hat{b} - \hat{b}^{\dagger})$, where $x_{ZPF} = \sqrt{\frac{\hbar}{2m\omega_m}}$ is the zero-point fluctuation amplitude of the mechanical resonator. It is also the spread of the coordinate in the ground state. With the mechanical vacuum state denoted by $|0\rangle$, $\langle 0| \hat{x}^2 |0\rangle = x_{ZPF}^2$. Using the number operator for the optical field, we get the Hamiltonian of the photon ensemble:

$$H_L = \hbar\omega_c \hat{a}^{\dagger}\hat{a} \tag{4}$$

We can thus write our combined Hamiltonian $H_L + H_M + H_{OM}$ as

$$\begin{aligned}\hat{H} = \hbar\omega_c \hat{a}^{\dagger}\hat{a} + \frac{-m^2\omega_m^2 x_{ZPF}^2(\hat{b} - \hat{b}^{\dagger})^2}{2m} + \frac{m\omega_m^2}{2} x_{ZPF}^2(\hat{b} + \hat{b}^{\dagger})^2 \\ + \hbar G x_{ZPF}(\hat{b} + \hat{b}^{\dagger})\hat{a}^{\dagger}\hat{a}\end{aligned} \tag{5}$$

Let us begin by simplifying the mechanical term:

$$\begin{aligned}
&\frac{-m^2\omega_m^2 x_{ZPF}^2(\hat{b} - \hat{b}^{\dagger})^2}{2m} + \frac{m\omega_m^2}{2} x_{ZPF}^2(\hat{b} + \hat{b}^{\dagger})^2 \\
=&\frac{1}{2} m\omega_m^2 x_{ZPF}^2 \left(-(\hat{b} - \hat{b}^{\dagger})^2 + (\hat{b} + \hat{b}^{\dagger})\right) \\
=&\frac{1}{2} m\omega_m^2 \frac{\hbar}{2m\omega_m} \left(-(\hat{b} - \hat{b}^{\dagger})^2 + (\hat{b} + \hat{b}^{\dagger})\right) \\
=&\frac{1}{4}\hbar\omega_m \left(-(\hat{b} - \hat{b}^{\dagger})^2 + (\hat{b} + \hat{b}^{\dagger})\right) \\
=&\frac{1}{4}\hbar\omega_m \left(-\hat{b}^2 - (\hat{b}^{\dagger})^2 + \hat{b}^{\dagger}\hat{b} + \hat{b}\hat{b}^{\dagger} + \hat{b}^2 + (\hat{b}^{\dagger})^2 + \hat{b}^{\dagger}\hat{b} + \hat{b}\hat{b}^{\dagger}\right) \\
=&\frac{1}{4}\hbar\omega_m \left(2\hat{b}^{\dagger}\hat{b} + 2\hat{b}\hat{b}^{\dagger}\right) \\
=&\frac{1}{4}\hbar\omega_m \left(2\hat{b}^{\dagger}\hat{b} + 2(\hat{b}^{\dagger}\hat{b} + 1)\right) \\
=&\hbar\omega_m \hat{b}^{\dagger}\hat{b} + \frac{1}{2}\hbar\omega_m
\end{aligned}$$

where we use first the definition of x_{ZPF}, then simple arithmetic, and finally the commutation property $[\hat{b}, \hat{b}^{\dagger}] = 1$ of the creation and annihilation operators to achieve the desired result. The term $\frac{1}{2}\hbar\omega_m$ at the end is an offset from the vacuum energy and will be disregarded for the rest of our treatment. By additionally defining the single-photon optomechanical coupling strength $g_0 = G x_{ZPF}$, we find that

$$\hat{H} = \hbar\omega_c \hat{a}^{\dagger}\hat{a} + \hbar\omega_m \hat{b}^{\dagger}\hat{b} + \hbar g_0 \hat{a}^{\dagger}\hat{a}(\hat{b} + \hat{b}^{\dagger}) \tag{6}$$

The final step of our treatment of the Hamiltonian shall be switching to a frame rotating at the laser frequency ω_L. The unitary transformation $\hat{U} = \exp\left(i\omega_L \hat{a}^{\dagger}\hat{a}t\right)$ is applied to the Hamiltonian to generate a new Hamiltonian $\hat{H} =$

$\hat{U}\hat{H}_{old}\hat{U}^\dagger + i\hbar\frac{\partial \hat{U}}{\partial t}$. As $\hat{U}$ commutes with all terms of Equation 6 [26], the transformation is simple:

$$\hat{H} = -\hbar\Delta\hat{a}^\dagger\hat{a} + \hbar\omega_m\hat{b}^\dagger\hat{b} - \hbar g_0\hat{a}^\dagger\hat{a}(\hat{b} + \hat{b}^\dagger) \tag{7}$$

where $\hat{a}$ is now in the rotating frame, *i.e.* $\hat{a}_{here} = e^{i\omega_L t}\hat{a}_{orig}$, and

$$\Delta = \omega_L - \omega_c \tag{8}$$

is the detuning of the laser from the cavity resonance. Note that there are two different sign conventions for the detuning; I follow the convention Aspelmeyer *et al.* [28] use in all cases where there are competing standards.

2.1.2 Equations of motion

As in our case, we are using the optomechanical cavity as an optical probe of the mechanics and thus are most interested in the emitted field, I shall now turn to input-output theory. This has the additional benefit of being able to deal with noise and a coherent laser drive [29]. Let us first cover the optical field amplitude $\hat{a}$. We choose our definition of optical decay rate κ so that $\hat{a}$ experiences decay at a rate of $\kappa/2$. The decay can be decomposed into a contribution from the input coupling κ_{ex} and other processes κ_0 so that $\kappa = \kappa_{ex} + \kappa_0$. (Later, we shall separate out absorption as κ_a from κ_0.) In the rotating frame, we can thus write

$$\dot{\hat{a}} = -\frac{\kappa}{2}\hat{a} + (i\Delta + G\hat{x})\hat{a} + \sqrt{\kappa_{ex}}\hat{a}_{in} + \sqrt{\kappa_0}\hat{f}_{in} \tag{9}$$

where $\hat{a}_{in}$ is the field incident to the cavity, for instance a coherent laser drive, and $\hat{f}_{in}$ is a noise term. The equation is presented in the rotating frame. The equivalent equation for the mechanical field is

$$\dot{\hat{b}} = \left(-i\omega_m - \frac{\Gamma_m}{2}\right)\hat{b} + ig_0\hat{a}^\dagger\hat{a} + \sqrt{\Gamma_m}\hat{b}_{in} \tag{10}$$

where Γ_m is the damping term for the mechanical motion and $\hat{b}_{in}$ is the field incident from the mechanical bath. If the resonator is not weakly damped, *i.e.* the assumption $\omega_m \gg \Gamma_m$ is not valid, then the treatment in Equation 10 does not apply and the mechanical field will have to be treated through the displacement $\hat{x}$ [28].

2.1.3 Linearization

In our applications, the number of photons in the cavity is sufficiently large that the cavity cannot distinguish between them. In such cases, it is possible to simplify the equations of motion by splitting the cavity field $\hat{a}$ into an average amplitude $\alpha = \langle\hat{a}\rangle = \sqrt{\bar{n}_{cav}}$ and a fluctuating term $\delta\hat{a}$ so that $\hat{a} = \alpha + \delta\hat{a}$. The optomechanical part of the Hamiltonian in Equation 7 then becomes

$$\hat{H}_{OM} = -\hbar g_0(\alpha + \delta\hat{a})^\dagger(\alpha + \delta\hat{a})(\hat{b} + \hat{b}^\dagger) \tag{11}$$

where the product of the optical terms can be expanded to

$$\begin{aligned}\hat{H}_{OM} =& -\hbar g_0|\alpha|^2(\hat{b}+\hat{b}^\dagger)\\ &-\hbar g_0(\alpha^*\delta\hat{a}+\alpha\delta\hat{a}^\dagger)(\hat{b}+\hat{b}^\dagger)\\ &-\hbar g_0\delta\hat{a}^\dagger\delta\hat{a}(\hat{b}+\hat{b}^\dagger)\end{aligned}$$

where the first term describes the contribution of an average radiation pressure force and can be discarded with an appropriate shift to the origin of the displacement coordinate and the final term can be omitted, as the fluctuations are assumed to be small. This leaves us with the middle term. As the number of photons in the cavity $\bar{n}_{cav}$ is real, so is its square root; *i.e.* $\alpha^* = \alpha = \sqrt{\bar{n}_{cav}}$. We can thus write

$$\bar{H}_{OM} = -\hbar g_0\sqrt{\bar{n}_{cav}}(\delta\hat{a}+\delta\hat{a}^\dagger)(\hat{b}+\hat{b}^\dagger) \tag{12}$$

as the linearized Hamiltonian for the optomechanical interaction.

We can additionally linearize the optomechanical equations of motion. We first linearize the optical field operator:

$$\begin{aligned}\dot{\hat{a}}(t) =& -\frac{\kappa}{2}a(t)+i\Delta_0 a(t)+iGx(t)a(t)+\sqrt{\kappa_e}a_{in}(t)+\sqrt{\kappa_0}\hat{f}_{in}\\ \dot{\alpha}+\dot{\delta\hat{a}}(t) =& -\frac{\kappa}{2}(\alpha+\delta\hat{a}(t))+i\Delta_0(\alpha+\delta\hat{a}(t))+iG(\bar{x}+\delta\hat{x}(t))(\alpha+\delta\hat{a}(t))\\ &+\sqrt{\kappa_e}(\alpha_{in}+\delta\hat{a}'_{in}(t))+\sqrt{\kappa_0}\hat{f}_{in}\end{aligned}$$

We remove $\dot{\alpha}$, as α by definition does not have a time dependence and its time derivative is zero:

$$\begin{aligned}\dot{\delta\hat{a}}(t) =& -\frac{\kappa}{2}\alpha-\frac{\kappa}{2}\delta\hat{a}(t)+i\Delta_0\alpha+i\Delta_0\delta\hat{a}(t)+iG\bar{x}\alpha+iG\alpha\delta\hat{x}(t)\\ &+iG\bar{x}\delta\hat{a}(t)+iG\delta\hat{a}(t)\delta\hat{x}(t)+\sqrt{\kappa_e}(\alpha_{in}+\delta\hat{a}'_{in}(t))+\sqrt{\kappa_0}\hat{f}_{in}\end{aligned}$$

We remove the second-order fluctuation term $\delta\hat{x}(t)\delta\hat{a}(t)$:

$$\begin{aligned}\dot{\delta\hat{a}}(t) =& -\frac{\kappa}{2}\alpha-\frac{\kappa}{2}\delta\hat{a}(t)+i\Delta_0\alpha+i\Delta_0\delta\hat{a}(t)+iG\bar{x}\alpha+iG\alpha\delta\hat{x}(t)+iG\bar{x}\delta\hat{a}(t)\\ &+\sqrt{\kappa_e}(\alpha_{in}+\delta\hat{a}'_{in}(t))+\sqrt{\kappa_0}\hat{f}_{in}\end{aligned}$$

Rearrangement of terms:

$$\begin{aligned}\dot{\delta\hat{a}}(t) =& \left[-\frac{\kappa}{2}+i\Delta_0+iG\bar{x}\right](\alpha+\delta\hat{a}(t))+iG\alpha\delta\hat{x}(t)\\ &+\sqrt{\kappa_e}\alpha_{in}+\sqrt{\kappa_e}\delta\hat{a}'_{in}(t)+\sqrt{\kappa_0}\hat{f}_{in}\end{aligned}$$

We now go to the modified drive detuning $\Delta = \Delta_0 + G\bar{x}$:

$$\dot{\delta\hat{a}}(t) = \left[-\frac{\kappa}{2} + i\Delta\right](\alpha + \delta\hat{a}(t)) + iG\alpha\delta\hat{x}(t) + \sqrt{\kappa_e}\alpha_{in} + \sqrt{\kappa_e}\delta\hat{a}'_{in}(t) + \sqrt{\kappa_0}\hat{f}_{in}$$

If one solves Equation 9 for the steady state amplitude under monochromatic laser illumination, where $\langle\hat{a}_{in}\rangle$ is the amplitude of the incident laser and $\hat{f}_{in} = 0$, one discovers a value of $\alpha = \frac{\sqrt{\kappa_e}\alpha_{in}}{\frac{\kappa}{2} - i\Delta}$. This can be inserted into the previous equation to yield:

$$\begin{aligned}\dot{\delta\hat{a}}(t) &= \left[-\frac{\kappa}{2} + i\Delta\right]\frac{\sqrt{\kappa_e}\alpha_{in}}{\frac{\kappa}{2} - i\Delta} + \left[-\frac{\kappa}{2} + i\Delta\right]\delta\hat{a}(t) + iG\alpha\delta\hat{x}(t) + \sqrt{\kappa_e}\alpha_{in} + \sqrt{\kappa_e}\delta\hat{a}'_{in}(t) + \sqrt{\kappa_0}\hat{f}_{in}\\ &= -\sqrt{\kappa_e}\alpha_{in} + \left[-\frac{\kappa}{2} + i\Delta\right]\delta\hat{a}(t) + iG\alpha\delta\hat{x}(t) + \sqrt{\kappa_e}\alpha_{in} + \sqrt{\kappa_e}\delta\hat{a}'_{in}(t) + \sqrt{\kappa_0}\hat{f}_{in}\end{aligned}$$

We notice that $\sqrt{\kappa_e}\alpha_{in}$ cancels itself out. We additionally notice that as $\alpha = \sqrt{\bar{n}_{cav}}$ and thus as $g = g_0\sqrt{\bar{n}_{cav}}$, $\alpha = \frac{g_0}{g_0}\sqrt{\bar{n}_{cav}} = \frac{g}{g_0}$. Likewise, $g_0 = Gx_{ZPF}$ and thus $G = \frac{g_0}{x_{ZPF}}$, so that $G\alpha = \frac{g}{x_{ZPF}}$, leading to $iG\alpha\delta\hat{x}(t) = i\frac{g}{x_{ZPF}}\delta\hat{x}(t)$.

Finally, we redefine the origin so that the time-average position $\bar{x} = 0$ and thus $\delta\hat{x}(t) = \hat{x}(t)$. As $\hat{x} = x_{ZPF}(\hat{b} + \hat{b}^\dagger)$, this lets us write $i\frac{g}{x_{ZPF}}\delta\hat{x}(t) = ig(\hat{b} + \hat{b}^\dagger)$. Thus we arrive at the final form:

$$\dot{\delta\hat{a}}(t) = \left[-\frac{\kappa}{2} + i\Delta\right]\delta\hat{a}(t) + ig(\hat{b} + \hat{b}^\dagger) + \sqrt{\kappa_e}\delta\hat{a}'_{in}(t) + \sqrt{\kappa_0}\hat{f}_{in} \tag{13}$$

For the mechanical portion, we shall treat it in terms of displacement $x = 2x_{ZPF}\,\mathrm{Re}\left\{\left\langle\hat{b}\right\rangle\right\}$.

$$\ddot{x} + \Gamma_m\dot{x} + \omega_m^2 x = \frac{1}{m_{eff}}F_{tot}(t), \tag{14}$$

where $F_{tot}(t)$ is the sum of all forces acting on the displacement. Ignoring thermal fluctuations, we can say that $F_{tot}(t) = F_{rp} = \hbar G|\alpha|^2$. To linearize, we write $x(t)$ as $\bar{x} + \delta x(t)$. The left side thus becomes

$$\begin{aligned}&\ddot{x}(t) + \Gamma_m\dot{x}(t) + \omega_m^2 x(t)\\ =&\ddot{\bar{x}} + \ddot{\delta x}(t) + \Gamma_m\left(\dot{\bar{x}} + \dot{\delta x}(t)\right) + \omega_m^2\left(\bar{x} + \delta x(t)\right)\\ =&\ddot{\delta x}(t) + \Gamma_m\dot{\delta x}(t) + \omega_m^2\left(\bar{x} + \delta x(t)\right)\end{aligned}$$

Again, we choose our coordinates so that the time-average position $\bar{x}$ is zero:

$$\ddot{\delta x}(t) + \Gamma_m\dot{\delta x}(t) + \omega_m^2\delta x(t) = \frac{1}{m_{eff}}F_{rp}(t)$$

The right side contains a prefactor of $\frac{1}{m_{eff}}$ and the radiation pressure force $F_{rp}(t) = \hbar G|\alpha|^2$, which we can also linearize:

$$\begin{aligned}F_{rp}(t) =&\hbar G(\alpha+\delta\hat{a}(t))^{\dagger}(\alpha+\delta\hat{a}(t))\\ =&\hbar G(\alpha^{*}\alpha+\alpha^{*}\delta\hat{a}(t)+\delta\hat{a}^{\dagger}(t)\alpha+\delta\hat{a}^{\dagger}(t)\delta\hat{a}(t))\end{aligned}$$

Discarding the second-order fluctuations and knowing that $\alpha^{*}\alpha = |\alpha|^{2}$:

$$F_{rp}(t) =\hbar G|\alpha|^{2}+\hbar G(\alpha^{*}\delta\hat{a}(t)+\delta\hat{a}^{\dagger}(t)\alpha).$$

The full form of the linearized mechanical displacement is thus

$$\ddot{\delta x}(t)+\Gamma_{m}\dot{\delta x}(t)+\omega_{m}^{2}\left(\bar{x}+\delta x(t)\right)=\frac{1}{m_{eff}}\left[\hbar G(\alpha^{*}\delta\hat{a}(t)+\delta\hat{a}^{\dagger}(t)\alpha)\right]. \tag{15}$$

Let us now present these in frequency space. For that, we will perform a Fourier transformation, first on the optical field:

$$\mathcal{F}\{\dot{\delta\hat{a}}(t)\} =\mathcal{F}\left\{\left[-\frac{\kappa}{2}+i\Delta\right]\delta\hat{a}(t)+iG\alpha\delta\hat{x}(t)+\sqrt{\kappa_{e}}\delta\hat{a}_{in}'(t)+\sqrt{\kappa_{0}}\hat{f}_{in}\right\} \tag{16}$$

$$-i\omega\delta\hat{a}(\omega)=\left(i\Delta-\frac{\kappa}{2}\right)\delta\hat{a}(\omega)+iG\alpha x(\omega) \tag{17}$$

and then on the mechanical position:

$$\mathcal{F}\left\{\delta\ddot{x}(t)+\Gamma_{m}\delta\dot{x}(t)+\omega_{m}^{2}\left(\bar{x}+\delta x(t)\right)\right\} =\mathcal{F}\left\{\frac{1}{m_{eff}}\left[\hbar G(\alpha^{*}\delta\hat{a}(t)+\delta\hat{a}^{\dagger}(t)\alpha)\right]\right\} \tag{18}$$

$$-\omega^{2}x(\omega)+\omega_{m}^{2}x(\omega)-i\omega\Gamma_{m}x(\omega) =\frac{1}{m}\hbar G(\alpha^{*}\delta\hat{a}(\omega)+\alpha(\delta\hat{a}(\omega)^{*})(\omega)) \tag{19}$$

$$m\left[-\omega^{2}+\omega_{m}^{2}-i\omega\Gamma_{m}\right]x(\omega) =\hbar G(\alpha^{*}\delta\hat{a}(\omega)+\alpha\delta\hat{a}(\omega)(-\omega)^{*}) \tag{20}$$

From this, we can express $\delta\hat{a}(\omega)$ in terms of $x(\omega)$:

$$\begin{aligned}\delta\hat{a}(\omega) =&\frac{-iG\alpha}{i(\omega+\Delta)+\frac{\kappa}{2}}x(\omega)\\ =&\frac{G\alpha}{(\omega+\Delta)+i\frac{\kappa}{2}}x(\omega)\end{aligned}$$

and then insert this into the equation for $x(\omega)$ to receive:

$$\begin{aligned}m\left[-\omega^{2}+\omega_{m}^{2}-i\omega\Gamma_{m}\right]x(\omega) =&\hbar G(\alpha^{*}\frac{G\alpha}{\Delta+\omega+i\frac{\kappa}{2}}+\alpha\frac{G\alpha^{*}}{\Delta-\omega-i\frac{\kappa}{2}}\\ =&\hbar G^{2}|\alpha|^{2}\left(\frac{1}{\Delta+\omega+i\frac{\kappa}{2}}+\frac{1}{\Delta-\omega-i\frac{\kappa}{2}}\right)\end{aligned}$$

Armed with this result, we can now move on to the next step.

2.1.4 Optomechanical spring equations

What we measure is not the position of the mechanics, but rather the resonance frequencies optical and mechanical, as well as their dampings. The detection of the output signal is discussed in Section 2.4; here, I shall look at the generated signal at the mechanical resonator.

Let us begin with the mechanical susceptibility $\chi_m(\omega)$, where $x = \chi_m(\omega)F$. In the absence of optomechanical coupling, it is of the form $\chi_m(\omega) = \frac{1}{m(\omega_m^2 - \omega^2 - i\omega\Gamma_m)}$. With the optomechanical contribution, the original susceptibility is modified so that $\chi_{eff}^{-1}(\omega) = \chi_m^{-1}(\omega) + \Sigma(\omega)$. $\Sigma(\omega)$ can be directly taken from the formula for $x(\omega)$, where knowing that $\hbar G^2|\alpha|^2 = 2m\omega_m g^2$, we get:

$$\Sigma(\omega) = 2m\omega_m g^2 \left(\frac{1}{\Delta + \omega + i\frac{\kappa}{2}} + \frac{1}{\Delta - \omega - i\frac{\kappa}{2}} \right). \tag{21}$$

We can also define $\Sigma(\omega)$ in a form along the lines of the original susceptibility:

$$\Sigma(\omega) \equiv m\omega[2\delta\omega_m(\omega) - i\delta\Gamma_m(\omega)], \tag{22}$$

so that the optically induced shift in the mechanical frequency is $\delta\omega_m(\omega) = \frac{\mathrm{Re}\{\Sigma(\omega)\}}{2m\omega}$ and the shift in the mechanical damping is $\delta\Gamma_m(\omega) = -\frac{\mathrm{Im}\{\Sigma(\omega)\}}{m\omega}$. Using the definition of $\Sigma(\omega)$ from Equation 21, we then receive the forms for $\delta\omega_m$ and $\delta\Gamma_m$:

$$\delta\omega_m(\omega) = g^2 \frac{\omega_m}{\omega} \left[\frac{\Delta + \omega}{(\Delta + \omega)^2 + \kappa^2/4} + \frac{\Delta - \omega}{(\Delta - \omega)^2 + \kappa^2/4} \right] \tag{23}$$

$$\delta\Gamma_m(\omega) = g^2 \frac{\omega_m}{\omega} \left[\frac{\kappa}{(\Delta + \omega)^2 + \kappa^2/4} - \frac{\kappa}{(\Delta - \omega)^2 + \kappa^2/4} \right], \tag{24}$$

where $\delta\omega_m$ and $\delta\Gamma_m$ describe the changes to the mechanical resonance frequency and mechanical damping, respectively, caused by the radiation pressure. This phenomenon is also known as the optical spring, shown in Figure 3.

The above equations are valid for all regimes where the linear approximation is applicable. We can, however, simplify them further by making certain assumptions about the cavity. If the incident illumination is small enough ($g \ll \kappa$), then one can assume that the perturbation caused by the optomechanical force is small, *i.e.* that $\omega = \omega_m$, and thus

$$\delta\omega_m = \bar{n}_{cav} g_0^2 \left[\frac{\Delta + \omega_m}{(\Delta + \omega_m)^2 + \kappa^2/4} + \frac{\Delta - \omega_m}{(\Delta - \omega_m)^2 + \kappa^2/4} \right] \tag{25}$$

$$\delta\Gamma_m = \bar{n}_{cav} g_0^2 \left[\frac{\kappa}{(\Delta + \omega_m)^2 + \kappa^2/4} - \frac{\kappa}{(\Delta - \omega_m)^2 + \kappa^2/4} \right], \tag{26}$$

where we have also used the knowledge that $g = \sqrt{\bar{n}_{cav}} g_0$.

We can further simplify these equations if $\kappa \gg \omega_m$. A large κ means that the probing of the cavity must be done over a larger range of ω_L and therefore Δ, so that $\Delta \pm \omega \approx \Delta$. This is known as the bad cavity limit or Doppler regime. In this regime, Equation 25 can be further simplified to

$$\delta\omega_m(\Delta) = \bar{n}_{cav} g_0^2 \frac{2\Delta}{\Delta^2 + \kappa^2/4}. \tag{27}$$

Performing the substitution for Equation 25 reveals that, at the bad cavity limit, $\delta\Gamma_m = 0$.

2.2 Photothermal force

Though radiation pressure is the most widely known force of light acting upon matter, illumination is the genesis of other forces as well. While the optical gradient force [30] and Doppler force [31] can be used for optomechanics, besides the aforementioned radiation pressure force, the force of greatest concern for our samples is the photothermal force, due to the high laser intensities used for readout. The characterization and quantification of the photothermal effect in our samples is the focus of article [**PII**].

The photothermal force arises from heating caused by cavity photon absorption. It is thus a dissipative force. It can nonetheless be used to enhance optomechanical coupling [32] and even, paradoxically, for feedback cooling of an optomechanical resonator to its mechanical ground state [32, 33]. Its mechanism of action is the thermal strain caused by heating from the absorbed photons. This strain causes deflection that affects the mechanical mode. The strength and phase difference from the radiation pressure force depend on the geometry and thermal properties of the sample.

While it is possible to do a full treatment of the thermal modes surface and volume [34], for the purposes of optomechanics, deriving an optomechanical equation of motion for a time-delayed force allows one to fit one's optomechanical data with parameters describing the thermal response [35]. Let us begin by writing the equation for the photothermal force:

$$F_{pt}(t) = \frac{\hbar G \beta}{\kappa_a \tau} \int_{-\infty}^{t} e^{-\frac{t-t'}{\tau}} \hat{a}_{abs}^{\dagger}(t') \hat{a}_{abs}(t')\, dt', \tag{28}$$

where we separate out the optical decay channel κ_a for photons lost to absorption, with $\hat{a}_{abs}(t) = \sqrt{\kappa_a}\hat{a}(t) - \hat{a}'_{abs}(t)$ the field operator characterizing the photons absorbed into the mechanical resonator, where $\hat{a}'_{abs}(t)$ is the field operator for the vacuum noise introduced to the system through photon absorption. The other parameters are β, which describes the relative strength of the photothermal and radiation pressure forces $F_{pt} = \beta F_{rp}$, and the thermal decay rate τ. It is possible for the photothermal force to act in direct opposition to the radiation pressure force, in which case β will be negative [35, 36].

We shall now derive the photothermal equations equivalent to Equations 23. As many portions of the derivation are identical, for the sake of space, I shall only treat the photothermal force itself before deriving the equations from the mechanical susceptibility.

2.2.1 Linearization

The first step is linearization of the photothermal force. We again write $\hat{a} = \alpha + \delta\hat{a}$, so that $\hat{a}_{abs}(t) = \sqrt{\kappa_a}\alpha + \sqrt{\kappa_a}\delta\hat{a} - \hat{a}'_{abs}(t)$ and insert this into Equation 28 to yield

$$F_{pt}(t) = \frac{\hbar G\beta}{\kappa_a\tau}\int_{-\infty}^{t} e^{-\frac{t-t'}{\tau}} \left[\left(\sqrt{\kappa_a}\alpha^* + \sqrt{\kappa_a}\delta\hat{a}^\dagger(t) - \delta\hat{a}'^\dagger_{abs}(t)\right)\right.$$
$$\left.\left(\sqrt{\kappa_a}\alpha + \sqrt{\kappa_a}\delta\hat{a}(t) - \delta\hat{a}'_{abs}(t)\right)\right] dt' \quad (29)$$

Let us take an excursion into simplifying the integrand:

$$\begin{aligned}
&\left(\sqrt{\kappa_a}\alpha^* + \sqrt{\kappa_a}\delta\hat{a}^\dagger(t) - \delta\hat{a}'^\dagger_{abs}(t)\right)\left(\sqrt{\kappa_a}\alpha + \sqrt{\kappa_a}\delta\hat{a}(t) - \delta\hat{a}'_{abs}(t)\right)\\
=&\kappa_a\left[\alpha^*\alpha + \alpha^*\delta\hat{a}(t) + \delta\hat{a}^\dagger(t)\alpha + \delta\hat{a}^\dagger(t)\delta\hat{a}\right]\\
&+\sqrt{\kappa_a}\left[-\alpha^*\delta\hat{a}'_{abs}(t) - \alpha\delta\hat{a}'^\dagger_{abs}(t) - \delta\hat{a}^\dagger(t)\delta\hat{a}'_{abs}(t) - \delta\hat{a}(t)\delta\hat{a}'^\dagger_{abs}(t)\right]\\
&+\delta\hat{a}'^\dagger_{abs}(t)\delta\hat{a}'_{abs}(t)
\end{aligned}$$

We ignore all second-order fluctuations and rearrange to receive:

$$\begin{aligned}
&\kappa_a\left[\alpha^*\alpha + \alpha^*\delta\hat{a}(t) + \delta\hat{a}^\dagger(t)\alpha\right] + \sqrt{\kappa_a}\left[-\alpha^*\delta\hat{a}'_{abs}(t) - \alpha\delta\hat{a}'^\dagger_{abs}(t)\right]\\
=&\kappa_a|\alpha|^2 + \kappa_a\left[\alpha^*\delta\hat{a}(t) + \delta\hat{a}^\dagger(t)\alpha\right] - \sqrt{\kappa_a}\left[\alpha^*\delta\hat{a}'_{abs}(t) + \alpha\delta\hat{a}'^\dagger_{abs}(t)\right]
\end{aligned}$$

The first term of $\kappa_a|\alpha|^2$ is a constant representing a constant photothermal force and can be discarded with an appropriate shift to the origin of the displacement coordinate. We re-insert the above integrand (save for $\kappa_a|\alpha|^2$) into the integral and take κ_a out of the integrand:

$$\begin{aligned}
F_{pt}(t) =&\frac{\hbar G\beta}{\kappa_a\tau}\int_{-\infty}^{t} e^{-\frac{t-t'}{\tau}}\left[\kappa_a\left[\alpha^*\delta\hat{a}(t) + \delta\hat{a}^\dagger(t)\alpha\right] - \sqrt{\kappa_a}\left[\alpha^*\delta\hat{a}'_{abs}(t) + \alpha\delta\hat{a}'^\dagger_{abs}(t)\right]\right] dt'\\
F_{pt}(t) =&\frac{\hbar G\beta}{\tau}\int_{-\infty}^{t} e^{-\frac{t-t'}{\tau}}\left[\alpha^*\delta\hat{a}(t) + \delta\hat{a}^\dagger(t)\alpha - \frac{1}{\sqrt{\kappa_a}}\left[\alpha^*\delta\hat{a}'_{abs}(t) + \alpha\delta\hat{a}'^\dagger_{abs}(t)\right]\right] dt'.
\end{aligned}$$

2.2.2 Spring equations

Again we begin with the mechanical susceptibility to derive the optomechanical spring equations. As before, $\chi^{-1}_{eff}(\omega) = \chi^{-1}_m(\omega) + \Sigma'(\omega)$; this time, though, $\Sigma'(\omega)$ includes both a radiation pressure and photothermal contribution. $\Sigma'(\omega)$ can be written as $\left(1 + \frac{\beta}{1-i\omega_m\tau}\right)\Sigma(\omega)$, so that, ignoring the noise terms,

$$\Sigma'(\omega) = \left(1 + \frac{\beta}{1 - i\omega_m\tau}\right) 2m\omega_m g^2\left(\frac{1}{\Delta + \omega + i\frac{\kappa}{2}} + \frac{1}{\Delta - \omega - i\frac{\kappa}{2}}\right).$$

As before, the shift in the mechanical resonance frequency is $\delta\omega_m(\omega) = \frac{\mathrm{Re}\{\Sigma'(\omega)\}}{2m\omega}$ and the shift in the mechanical damping is $\delta\Gamma_m(\omega) = -\frac{\mathrm{Im}\{\Sigma'(\omega)\}}{m\omega}$. We begin by opening out $\Sigma'(\omega)$ so that we may sort by power of i:

$$\Sigma'(\omega) = \left(1 + \frac{\beta}{1 - i\omega_m\tau}\right) 2m\omega_m g^2 \left(\frac{1}{\Delta + \omega + i\frac{\kappa}{2}} + \frac{1}{\Delta - \omega - i\frac{\kappa}{2}}\right) \tag{30}$$

$$= 2m\omega_m g^2 \left(1 + \beta\frac{1 + i\omega_m\tau}{1 + \omega_m^2\tau^2}\right) \left(\frac{\Delta + \omega - i\frac{\kappa}{2}}{(\Delta + \omega)^2 + \frac{\kappa^2}{4}} + \frac{\Delta - \omega + i\frac{\kappa}{2}}{(\Delta - \omega)^2 + \frac{\kappa^2}{4}}\right) \tag{31}$$

We can partition the real and imaginary parts of the photothermal force and write

$$\beta\frac{1 + i\omega_m\tau}{1 + \omega_m^2\tau^2} = \frac{\beta}{1 + \omega_m^2\tau^2} + \frac{i\beta\omega_m\tau}{1 + \omega_m^2\tau^2}.$$

Now we shall pick out $\mathrm{Re}\{\Sigma'(\omega)\}$ and $\mathrm{Im}\{\Sigma'(\omega)\}$. We shall for the moment ignore the prefactor $2m\omega_m g^2$, as that is a real number which can be reapplied later, and simply open up the product and classify based on power of i:

$$\begin{aligned}
&\left(1 + \frac{\beta}{1 + \omega_m^2\tau^2} + \frac{i\beta\omega_m\tau}{1 + \omega_m^2\tau^2}\right) \left(\frac{\Delta + \omega - i\frac{\kappa}{2}}{(\Delta + \omega)^2 + \frac{\kappa^2}{4}} + \frac{\Delta - \omega + i\frac{\kappa}{2}}{(\Delta - \omega)^2 + \frac{\kappa^2}{4}}\right) \\
&= \left(1 + \frac{\beta}{1 + \omega_m^2\tau^2}\right) \left(\frac{\Delta + \omega}{(\Delta + \omega)^2 + \frac{\kappa^2}{4}} + \frac{\Delta - \omega}{(\Delta - \omega)^2 + \frac{\kappa^2}{4}}\right) \\
&\quad + i\left(1 + \frac{\beta}{1 + \omega_m^2\tau^2}\right) \left(\frac{-\frac{\kappa}{2}}{(\Delta + \omega)^2 + \frac{\kappa^2}{4}} + \frac{\frac{\kappa}{2}}{(\Delta - \omega)^2 + \frac{\kappa^2}{4}}\right) \\
&\quad + i\left(\frac{\beta\omega_m\tau}{1 + \omega_m^2\tau^2}\right) \left(\frac{\Delta + \omega}{(\Delta + \omega)^2 + \frac{\kappa^2}{4}} + \frac{\Delta - \omega}{(\Delta - \omega)^2 + \frac{\kappa^2}{4}}\right) \\
&\quad + i^2\left(\frac{\beta\omega_m\tau}{1 + \omega_m^2\tau^2}\right) \left(\frac{-\frac{\kappa}{2}}{(\Delta + \omega)^2 + \frac{\kappa^2}{4}} + \frac{\frac{\kappa}{2}}{(\Delta - \omega)^2 + \frac{\kappa^2}{4}}\right)
\end{aligned}$$

As $i^2 = -1$, we arrive at the following form for $\delta\omega_m = \frac{\mathrm{Re}\{\Sigma'(\omega)\}}{2m\omega}$:

$$\begin{aligned}
\delta\omega_m = \frac{\omega_m}{\omega} g^2 \Bigg[&\left(1 + \frac{\beta}{1 + \omega_m^2\tau^2}\right) \left(\frac{\Delta + \omega}{(\Delta + \omega)^2 + \frac{\kappa^2}{4}} + \frac{\Delta - \omega}{(\Delta - \omega)^2 + \frac{\kappa^2}{4}}\right) \\
&- \left(\frac{\beta\omega_m\tau}{1 + \omega_m^2\tau^2}\right) \left(\frac{\frac{\kappa}{2}}{(\Delta - \omega)^2 + \frac{\kappa^2}{4}} - \frac{\frac{\kappa}{2}}{(\Delta + \omega)^2 + \frac{\kappa^2}{4}}\right)\Bigg]
\end{aligned} \tag{32}$$

We can likewise find $\delta\Gamma_m(\omega) = -\frac{\mathrm{Im}\{\Sigma'(\omega)\}}{m\omega}$:

$$\begin{aligned}
\delta\Gamma_m = -2\frac{\omega_m}{\omega} g^2 \Bigg[&\left(1 + \frac{\beta}{1 + \omega_m^2\tau^2}\right) \left(\frac{\frac{\kappa}{2}}{(\Delta - \omega)^2 + \frac{\kappa^2}{4}} - \frac{\frac{\kappa}{2}}{(\Delta + \omega)^2 + \frac{\kappa^2}{4}}\right) \\
&+ \left(\frac{\beta\omega_m\tau}{1 + \omega_m^2\tau^2}\right) \left(\frac{\Delta + \omega}{(\Delta + \omega)^2 + \frac{\kappa^2}{4}} + \frac{\Delta - \omega}{(\Delta - \omega)^2 + \frac{\kappa^2}{4}}\right)\Bigg]
\end{aligned} \tag{33}$$

Both Equation 32 and Equation 33 differ from their pure radiation pressure equivalents in Equation 23 and Equation 24. One can think of it as the photothermal force affecting not only the magnitude of the shifts in the mechanical resonance frequency and damping, but also the phase.

If we again investigate the situation where the laser drive is weak enough that we can restrict our analysis to the original oscillation frequency ($\omega = \omega_m$), we can simplify Equations 32 and 33 into

$$\begin{aligned}\delta\omega_m = g^2 \Bigg[&\left(1 + \frac{\beta}{1+\omega_m^2\tau^2}\right)\left(\frac{\Delta+\omega_m}{(\Delta+\omega_m)^2+\frac{\kappa^2}{4}} + \frac{\Delta-\omega_m}{(\Delta-\omega_m)^2+\frac{\kappa^2}{4}}\right) \\ &- \left(\frac{\beta\omega_m\tau}{1+\omega_m^2\tau^2}\right)\left(\frac{\frac{\kappa}{2}}{(\Delta-\omega_m)^2+\frac{\kappa^2}{4}} - \frac{\frac{\kappa}{2}}{(\Delta+\omega_m)^2+\frac{\kappa^2}{4}}\right)\Bigg] \end{aligned} \tag{34}$$

and

$$\begin{aligned}\delta\Gamma_m = -2g^2 \Bigg[&\left(1 + \frac{\beta}{1+\omega_m^2\tau^2}\right)\left(\frac{\frac{\kappa}{2}}{(\Delta-\omega_m)^2+\frac{\kappa^2}{4}} - \frac{\frac{\kappa}{2}}{(\Delta+\omega_m)^2+\frac{\kappa^2}{4}}\right) \\ &+ \left(\frac{\beta\omega_m\tau}{1+\omega_m^2\tau^2}\right)\left(\frac{\Delta+\omega_m}{(\Delta+\omega_m)^2+\frac{\kappa^2}{4}} + \frac{\Delta-\omega_m}{(\Delta-\omega_m)^2+\frac{\kappa^2}{4}}\right)\Bigg]. \end{aligned} \tag{35}$$

At the bad cavity limit ($\Delta \pm \omega \approx \Delta$), a cavity with photothermal forces will have both $\delta\omega_m$ and $\delta\Gamma_m$ be nonzero:

$$\delta\omega_m = g^2\left(1+\frac{\beta}{1+\omega_m^2\tau^2}\right)\frac{2\Delta}{\Delta^2+\frac{\kappa^2}{4}} \tag{36}$$

$$\delta\Gamma_m = -2g^2\left(\frac{\beta\omega_m\tau}{1+\omega_m^2\tau^2}\right)\frac{2\Delta}{\Delta^2+\frac{\kappa^2}{4}}. \tag{37}$$

A key thing to note with all photothermal effects is that the magnitude of the photothermal force depends on the incident power via the absorption rate. It is thus possible to observe drastically different optomechanical responses in a single resonator at different powers. Observed changes could come solely from the change in radiation pressure effects caused by the increase in cavity photons; however, true elimination of photothermal effects from consideration requires quantitative analysis. One such case and using Monte Carlo phonon ray tracing simulations to fix a value for τ are the focus of article [**PII**].

2.3 Interferometer

Now let us take a step out of the realm of theory and consider an experimentalist's concerns. The optomechanical system described above is all fine and dandy, yet that which cannot be measured cannot be proven to exist. How, then, does one measure an optomechanical cavity?

If one's application does not require information about the phase, one may simply shine a laser on the resonator and measure the reflected power. If one does desire phase referencing, like we do for reasons that will become clear in Section 2.4, this requires building an interferometer. At its most basic, homodyne interferometry involves shining light on a sample and then interfering the reflected light with light which is phase coherent and of identical frequency with the sample branch in a 50/50 beam splitter. The outputs of the beam splitter are then gathered, and from the intensity difference between them, information about the phase difference can be gleaned. For a Michelson or Mach-Zehnder interferometer, both the sample and reference beams come from the same light source, split by a 50/50 beam splitter into a sample branch and a reference branch, usually referred to as the local oscillator. This sort of setup is visualized in Figure 2.

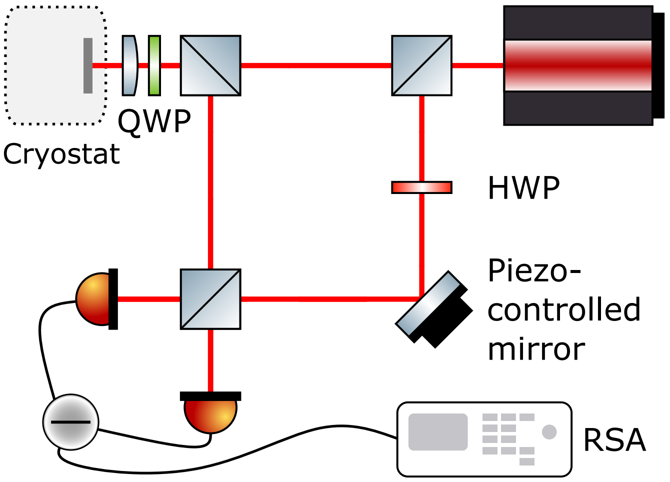

FIGURE 2 A schematic of a Michelson-type homodyne interferometer. A laser beam is split into two branches, one of which reflects off the sample before being reunited with the reference branch. The interference between these two branches can reveal characteristics of the sample. Image from **[PI]**, reproduced under the license CC BY 4.0.

Mathemathically, we shall start with the beam splitter. The incident fields are the field reflected from the sample, $\hat{a}_s$, and the reference field $\hat{a}_{LO}$, where LO stands for local oscillator. The outgoing fields are designated $\hat{a}_+$ and $\hat{a}_-$, so that

$$\hat{a}_\pm = \frac{1}{\sqrt{2}} \left(\hat{a}_{LO} \pm \hat{a}_s \right). \tag{38}$$

The Hamiltonian of the beam splitter is

$$H = |\hat{a}_+|^2 - |\hat{a}_-|^2 = i(\hat{a}_s^* \hat{a}_{LO} - \hat{a}_{LO}^* \hat{a}_s) \tag{39}$$

Let us now look at $\hat{a}_s$ and $\hat{a}_{LO}$ in more detail. The signal branch optical intensity $\hat{a}_s$ depends on the cavity optical field $\hat{a}$ and the cavity outcoupling efficiency

κ_{out} so that $\hat{a}_s = \sqrt{\kappa_{out}}\hat{a}$. We return again to the linearized version of Equation 9 and its steady state solution of $\alpha = \frac{\sqrt{\kappa_e}\alpha_{in}}{\frac{\kappa}{2}-i\Delta}$, giving us $\alpha_s = \sqrt{\kappa_{out}}\frac{\sqrt{\kappa_e}\alpha_{in}}{\frac{\kappa}{2}-i\Delta}$.

$$\alpha = \frac{\sqrt{\kappa_{in}}\alpha_{in}}{-i\Delta(t) + \frac{\kappa}{2}} = \frac{\sqrt{\kappa_{in}}\alpha_{in}(i\Delta + \frac{\kappa}{2})}{\Delta^2 + \frac{\kappa^2}{4}} \tag{40}$$

For $\hat{a}_{LO}$, we write separately the intensity $\alpha_{LO} \equiv |\hat{a}_{LO}|$ and the phase $e^{i\phi}$, so that $\hat{a}_{LO} = \alpha_{LO}e^{i\phi}$. We additionally declare the phase ϕ to be the phase difference between $\hat{a}_{LO}$ and $\hat{a}_s$, which is what enables us to write α_{in} instead of $\hat{a}_{in}$. We then substitute $\hat{a}_{LO} = \alpha_{LO}e^{i\phi}$ and Equation 40 into Equation 39, giving us

$$\begin{aligned}
H =& i(\hat{a}_s^*\hat{a}_{LO} - \hat{a}_{LO}^*\hat{a}_s) \\
=& i\alpha_{LO}\left(\frac{\sqrt{\kappa_e\kappa_{out}\alpha_{in}}(-i\Delta + \kappa/2)}{\Delta^2 + \kappa^2/4}e^{i\phi} - \frac{\sqrt{\kappa_e\kappa_{out}\alpha_{in}}(i\Delta + \kappa/2)}{\Delta^2 + \kappa^2/4}e^{-i\phi}\right) \\
=& \sqrt{\kappa_e\kappa_{out}}\alpha_{in}\alpha_{LO}i\left(\frac{\kappa/2 - i\Delta}{\kappa^2/4 + \Delta^2}e^{i\phi} - \frac{\kappa/2 + i\Delta}{\kappa^2/4 + \Delta^2}e^{-i\phi}\right) \\
=& \sqrt{\kappa_e\kappa_{out}}\alpha_{in}\alpha_{LO}\frac{1}{\kappa^2/4 + \Delta^2}\left(\Delta(e^{i\phi} + e^{-i\phi}) + \frac{\kappa}{2}i(e^{i\phi} - e^{-i\phi})\right) \\
=& \sqrt{\kappa_e\kappa_{out}}\alpha_{in}\alpha_{LO}\frac{1}{\kappa^2/4 + \Delta^2}\left(2\Delta\cos\phi + 2\frac{\kappa}{2}\sin\phi\right) \\
=& \sqrt{\kappa_e\kappa_{out}}\alpha_{in}\alpha_{LO}\frac{1}{\kappa^2/4 + \Delta^2}\left(2\Delta\cos\phi + 2\frac{\kappa}{2}\sin\phi\right) \\
=& \sqrt{\kappa_e\kappa_{out}}\alpha_{in}\alpha_{LO}\left(2\frac{\Delta}{\kappa^2/4 + \Delta^2}\cos\phi + 2\frac{\kappa/2}{\kappa^2/4 + \Delta^2}\sin\phi\right) \\
=& \sqrt{\kappa_e\kappa_{out}}\alpha_{in}\alpha_{LO}\left(2\frac{1}{\kappa^2/4\Delta + \Delta}\cos\phi + 2\frac{1}{\kappa/2 + 2\Delta^2/\kappa}\sin\phi\right) \\
=& \sqrt{\kappa_e\kappa_{out}}\frac{\alpha_{LO}\alpha_{in}}{1 + (2\Delta/\kappa)^2}\left(\frac{2\Delta}{\kappa}\cos\phi + \sin\phi\right),
\end{aligned}$$

whence we can see that, given the correct phase difference ϕ between the signal and local oscillator branches, the detuning Δ is explicitly detected.

2.4 Power spectral density

An interested reader's attention might now turn to the question of what, exactly, it is that we have measured with our interferometer. We have performed a Fourier transform on the difference of the two signals outgoing from the second beam splitter. The result is the power spectral density (PSD) $S_{\Delta\Delta}(\omega)$ of the signal emitted by the resonator, where Δ is the modified drive detuning $\Delta_0 + G\bar{x}$. We thus see that $\Delta \propto x$, allowing us to approximate that $S_{\Delta\Delta}(\omega) \approx S_{xx}(\omega)$; *i.e.* that the PSD we measure shows the frequency components of the mechanical motion of the optomechanical resonator, visible as increases in PSD intensity with width Γ_m, as shown in Figure 3.

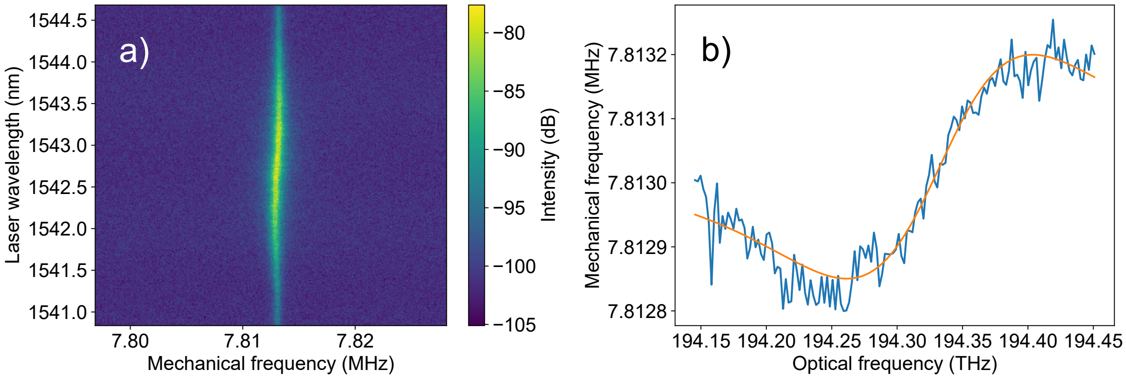

FIGURE 3 a) An example noise power spectral density spectrum of a weakly damped resonator, measured interferometrically. b) The extracted mechanical resonance frequency as a function of incident optical frequency (blue) and the pure radiation pressure optical spring (orange) fit according to Equation 23.

Let us now go over the mathematics. First, we shall begin with how mechanical motion can be detected through $S_{xx}(\omega)$. If we measure the position $x(t)$ over a time period t', then the gated Fourier transform over a finite time interval t' is

$$\mathcal{F}\left(x(t)\right) = \frac{1}{t'}\int_0^{t'} x(t)e^{i\omega t}dt \tag{41}$$

Next, we apply the Wiener-Khinchin theorem. For physicists, it says that a function's autocorrelation is given by the Fourier transform of the absolute square of the function, and that the spectral decomposition of the autocorrelation function comes from the spectral decomposition of the process generating the function. (Mathematicians, of course, have to worry about convergence and other such minor issues.) In other words,

$$S_{xx}(\omega) = \left\langle |x(\omega)|^2 \right\rangle, \tag{42}$$

with $S_{xx}(\omega)$ defined as

$$S_{xx}(\omega) = \int_{-\infty}^{\infty} \langle x(t)x(0)\rangle e^{i\omega t}dt, \tag{43}$$

and thus

$$\int_{-\infty}^{\infty} \frac{1}{2\pi} S_{xx}(\omega)d\omega = \langle x^2\rangle, \tag{44}$$

i.e. the variance of the mechanical displacement $\langle x^2\rangle$ is given by the area under the noise spectrum.

There is more, however. As per the fluctuation-dissipation theorem, the thermodynamical fluctuations of a system depend on its susceptibility [37]. In the classical case, for the Brownian motion of a mechanical system in thermal equilibrium, this can be written as

$$S_{xx}(\omega) = 2\frac{k_B T}{\omega}\,\mathrm{Im}\{\chi_{xx}(\omega)\}, \tag{45}$$

where $\chi_{xx}(\omega)$ is the mechanical susceptibility. For weakly damped resonators ($\Gamma_m \ll \omega_m$), such as those treated in papers **[PI]**, **[PII]**, and **[PIII]**, this yields Lorentzian peaks of width Γ_m and area $\langle x^2 \rangle \sim T$ at the frequency $\omega = \omega_m$ in the noise power spectral density, which we detect interferometrically.

2.5 Sliced nanobeam optomechancal resonator

Let us now end our look at optomechanics with a final excursion from theory to reality. If we wish to measure something, it must first exist. This means creating an optical cavity whose resonance frequency depends on mechanical motion. For this, we use suspended thin layers of Si, whereon we create an optical cavity, using a photonic crystal structure, and a mechanical resonator, using a nanobeam. More details on the fabrication and design are given in Chapter 4. The device type discussed herein and measured in Figure 3 is shown in Figure 4.

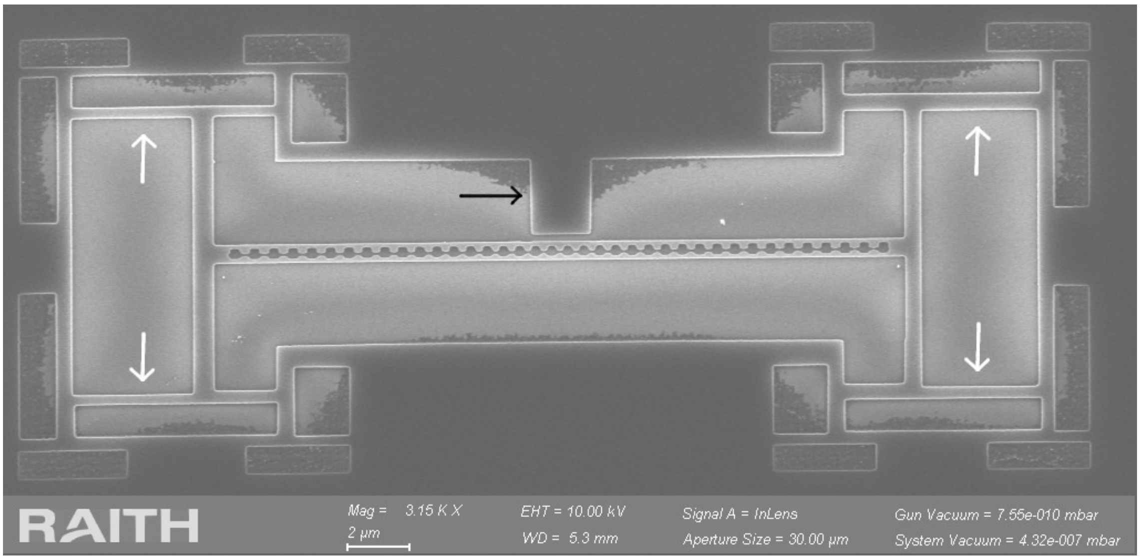

FIGURE 4 An example sliced nanobeam photonic crystal cavity. Note the strain relief structures (indicated by white arrows) surrounding the nanobeam on either side and the balcony (black arrow) for introduction of a micromagnet, the purpose of which shall be elaborated upon in Section 3.4.2.

The device is a photonic crystal fabricated out of silicon. The periodic alteration in refractive index between air (n=1) and Si (n=3.98) creates an optical cavity that only supports one mode. By grading the periodicity or other parameters, the ends have a different supported mode than the center, functioning as Bragg mirrors that confine the desired optical mode to the center of the beam, a simulation of which is shown in Figure 5.

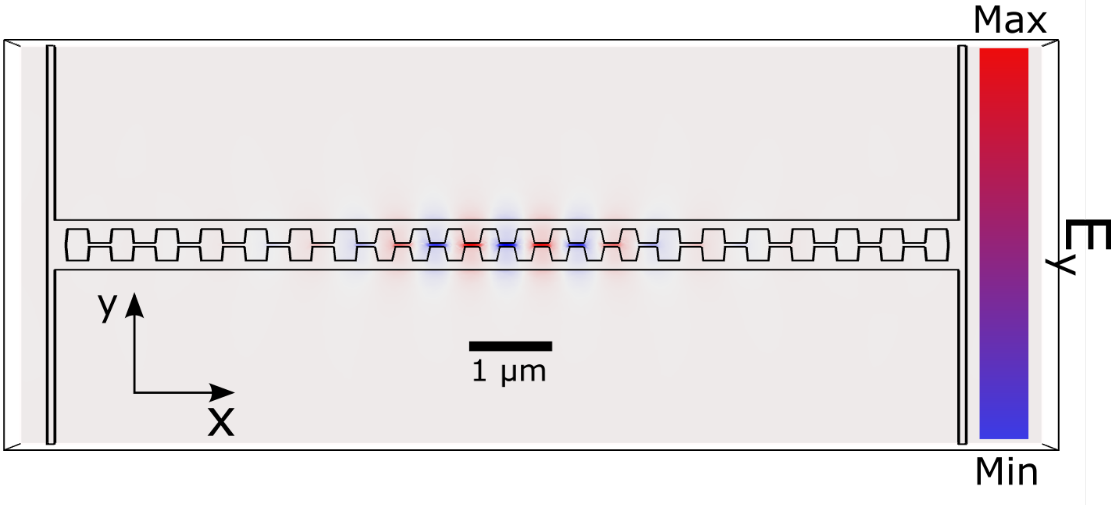

FIGURE 5 The y-axis component of the electrical field of the optical cavity mode of a similar type of structure to that of Figure 4, albeit one with shorter mirror segments and thus a higher mechanical resonance frequency. Note the confinement to the center of the beam as well as the fact the intensity maximum of the field is in the air, rather than in the silicon. From [**PI**] supplementary information, reproduced under the license CC BY 4.0.

The beam is also split lengthwise through the middle. As a result, the optical field is strongest in the gap, and we have an extremely floppy in-plane antisymmetric breathing mode with a large x_{ZPF}, as shown in Figure 6. Thus, as the optical mode is confined to the region with the largest displacement, we have strong optomechanical coupling.

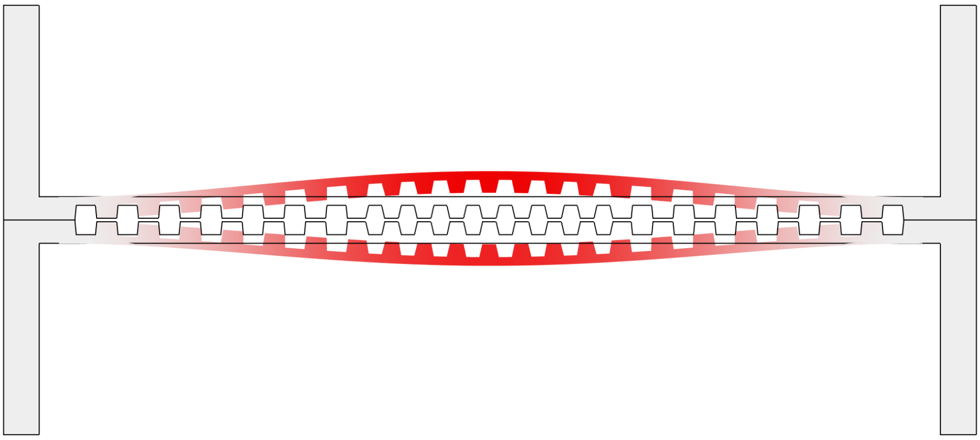

FIGURE 6 A schematic of the mechanical displacement of the breathing mode. The largest displacement is in the middle, the region of the highest optical intensity.

3 SPIN MEASUREMENTS

In this chapter, I speak of the end goal of our avenue of inquiry. While none of the papers included include a spin measurement, they all build towards one: In **[PI]**, we examine how implanting our donors — our qubits — affects the mechanism we'll use for readout. In **[PIII]**, we describe the readout mechanism and examine potential means of coupling to it. Here I go over the chain of coupling from the spin state to the mechanics and introduce the required theoretical background, before finally describing the full spin measurement and the experimental considerations with which one must concern oneself.

3.1 The two-level system

The two-level system is the simplest non-trivial quantum system and also all that is necessary for quantum computation. While a classical bit has two possible states, $|0\rangle$ or $|1\rangle$ and no other, a two-level system can be in $|0\rangle$ or $|1\rangle$ — or any superposition of the two: $\alpha\,|0\rangle + \beta\,|1\rangle$, where α and β are complex numbers that describe the probability of finding the system in each state, so that *e.g.* $|\alpha|^2$ is the probability amplitude of finding the system in the state $|0\rangle$ (and thus $0 \leq |\alpha|^2 \leq 1$). A graphical representation of this difference is presented in Figure 7. In essence, instead of only pointing up or down, the state vector can point towards any point on the surface of a sphere.

Here it must be noted that, while the state vector can exist in a superposition of $|0\rangle$ and $|1\rangle$, the outcome of a measurement can only be either $|0\rangle$ or $|1\rangle$, not a mix of the two. Proper characterization of the state vector thus involves multiple measurements for statistical analysis. State initialization, on the other hand, is made easy: all one needs to do is measure the state. If the result is the desired state of $|0\rangle$ and $|1\rangle$, nothing more needs to be done; if not, a bit-flip operation can be performed and the qubit is ready for computation.

This general treatment applies for any system with two non-degenerate states, whether it be photon polarization, electron spin, or something more exotic.

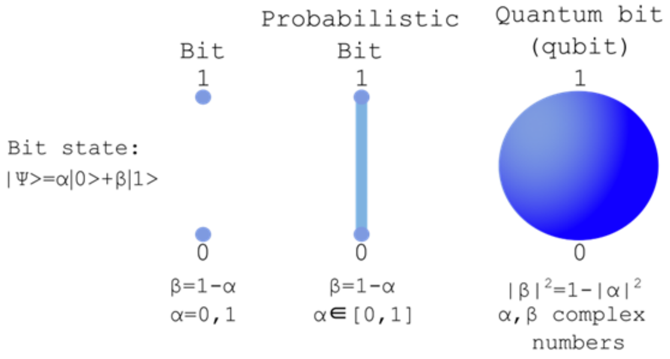

FIGURE 7 A schematic of the differences between a classical bit, a probabilistic bit, and a qubit.

Through manipulation and readout of the state by suitable means, any two-level system can be used for quantum computation. The precise system we shall turn our attention to is the spin state of a donor electron in Si, *e.g.* that from a dopant like P.

3.2 Donor spin qubits

The silicon semiconductor industry is a vast behemoth with experience purifying Si down to an impurity concentration of less than 0.1 parts per million and precisely controlling the concentration of various acceptors (*e.g.* B, Ga) and donors (*e.g.* P, As) [38]. The band structure of this doped Si is well known as well, with for *e.g.* P, when it substitutes a Si atom in the lattice, four of the P atom's five valence electrons bond with the valence electrons of neighboring Si atoms, while the fifth is raised to the conduction band. There it joins with its brethren from other P donors to increase the conductivity of the doped Si.

While the above treatment is valid at room temperature, at low temperatures, the excess electron provided by the donor is not delocalized into the conduction band, but rather localizes so that it is pinned to the donor atom with a wave function that has a radius of only a few lattice constants, allowing the treatment of the electron as a discrete system rather than a band element. In fact, at low temperatures, the P^+-e^-–system is analogous to a H atom in vacuum, with a loosely bound electron with a Bohr radius of around 2 nm [39, 40].

3.2.1 Ion implantation

Of course, while economies of scale are excellent for mass manufacture, in the research and development stage, we want something smaller and more flexible. We thus use ion implantation, where Si is bombarded with ions of the desired species so that they embed themselves in the Si lattice. Annealing will then heal the lattice damage sustained during the ion bombardment and have the donor ions be incorporated in the lattice as substitutional donors. After the anneal, devices can be fabricated on the now-doped Si.

While the full single-donor post-fabrication implantation procedure has yet to be performed, article **[PI]** deals with the effects of implantation damage on the optomechanical resonator device we use. The effects of implantation damage on the Si lattice are noticeable, but they can be healed with a post-fabrication anneal so that the optomechanical resonator works as intended afterwards. Figure 8 shows the changes induced by annealing on the mechanical resonance frequency and linewidth for two resonators at room temperature and 6K, showing the lattice healing effect. The donor species dealt with in article **[PI]** is ^{31}P, which is comparatively light; the lattice damage and thus effects of implantation will likely be more prominent with heavier donor species.

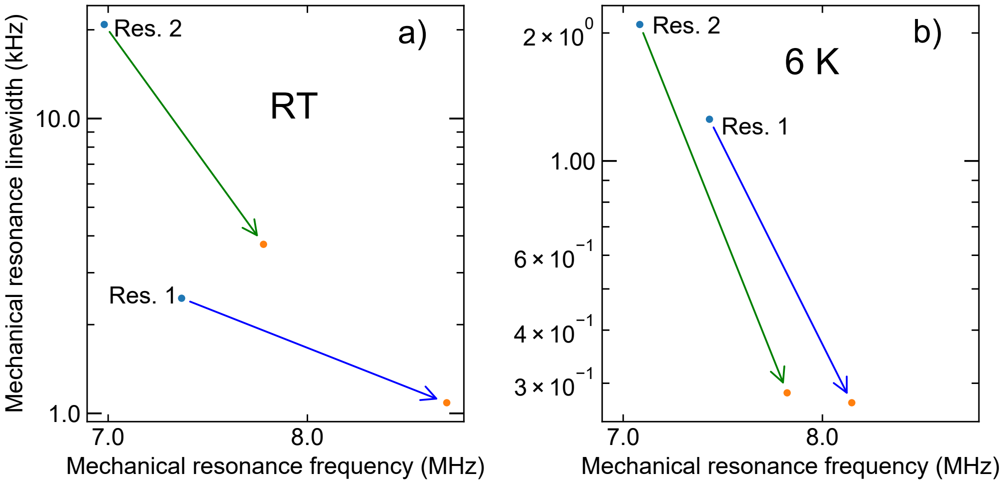

FIGURE 8 Effects of a post-fabrication anneal on the mechanical resonance frequency and linewidth of two example resonators at room temperature and 6K, showing a decrease in linewidth and increase in resonance frequency, consistent with a reduction in lattice disorder. From **[PI]**, reproduced under the license CC BY 4.0.

Pre-fabrication implantation is suitable for ensemble doping, where we probe the spin state of an ensemble of spins, rather than using a single spin as a qubit. For single spin doping, though, it is impractical to first dope the Si layer at such sparse concentrations that a resonator would on average have one donor, and then hope against hope that the fabricated resonators will by random chance happen to include a donor in a useful position. Instead, one must either implant donors in known locations and fabricate the devices, or first fabricate the devices and then implant them with a donor. The techniques to control the amount and placement of ions fall under the umbrella of deterministic ion implantation. Ion placement can be controlled by coating the ion-less regions with a mask of *e.g.* SiO_2 [41] or PMMA [42], or masklessly by implanting ions with an extremely precise focused ion beam [43]. Single ion implantation requires small enough ion emission probabilities that often a pulse has no ions in it. The presence of an ion in a pulse can be detected through electrodes on the target [44] or secondary electron emission [45], the precision of which can be further improved through statistical analysis of the detector [46].

3.2.2 Spin states

To form a qubit out of an electron bound to a P donor, we need two states at different energies. At zero magnetic field, the combined electron ($|\downarrow\rangle$, $|\uparrow\rangle$) and ^{31}P nuclear ($|\Downarrow\rangle$, $|\Uparrow\rangle$) spin system is split into two states: the singlet $|\downarrow\Uparrow\rangle$ and the triplet consisting of the degenerate states $|\uparrow\Uparrow\rangle$, $|\uparrow\Downarrow\rangle$, and $|\downarrow\Downarrow\rangle$ [47]. The magnitude of this split is the hyperfine interaction constant A. Breaking the triplet degeneracy requires the addition of a static magnetic field B_0, which induces Zeeman splitting and gives all four spin states energy levels which are tunable by adjusting the strength of B_0, as shown in Figure 9. This leads to all five spin transitions — both electron spin flip transitions, $|\downarrow\Downarrow\rangle \Leftrightarrow |\uparrow\Downarrow\rangle$ and $|\downarrow\Uparrow\rangle \Leftrightarrow |\uparrow\Uparrow\rangle$, both nuclear spin flip transitions, $|\downarrow\Downarrow\rangle \Leftrightarrow |\downarrow\Uparrow\rangle$ and $|\uparrow\Downarrow\rangle \Leftrightarrow |\uparrow\Uparrow\rangle$, and the flip-flop transition, $|\downarrow\Uparrow\rangle \Leftrightarrow |\uparrow\Downarrow\rangle$ — all having unique energy splits associated with them.

As P in Si does not have optically active transitions and we wish to have an optical readout, we must somehow couple one of these transitions to something that does have an optical readout — for instance, optomechanics, as discussed in Chapter 2. If we wish to resonantly couple the mechanical motion and the spin, we must choose a B_0 where the resulting energy splitting gives an energy splitting E that matches the mechanical resonance frequency of the device ω_m, as $E = \hbar\omega_m$.

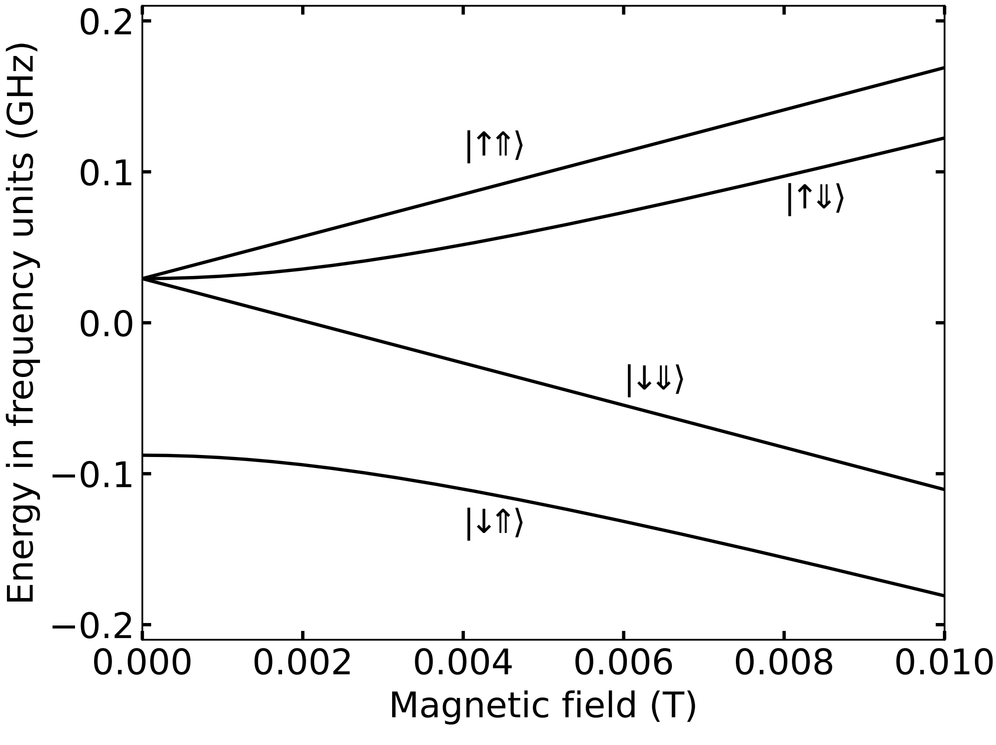

FIGURE 9 The effect of an external magnetic field along the z-axis on the energy levels of the electron and nuclear spins for a ^{31}P in Si system.

However, things aren't quite that simple. Changing the energy levels of the states involves a σ_z coupling, which means the states are not coupled to each other. Coherent exitation transfer between the spin and mechanics, on the other hand, would require the orthogonal σ_x coupling. How, then, to create one?

3.3 Dressing the qubit

Nudity is generally frowned upon in polite company. There are, however, additional benefits to dressing one's qubit.

First, let us define dressing. The average qubit is unable to wear clothes. It is, however, subject to noise, as a result of which the theoretical ideal qubit S_I is unachievable: we are always dealing with the actual qubit $S_A \neq S_I$ [48]. We can do our best to eliminate all noise sources, so that S_A approaches S_I — or we can "dress" the qubit by performing a controlled transformation on it so that the resulting S_A is sensitive to different frequencies of noise to the original qubit and also a usable qubit in itself [19]. Dressing, in effect, is an introduction of a controlled noise that lets one choose one's S_A [48]. Due to the change in noise sensitivity, dressed qubits can be made more resilient against the dominant noise in the system [49].

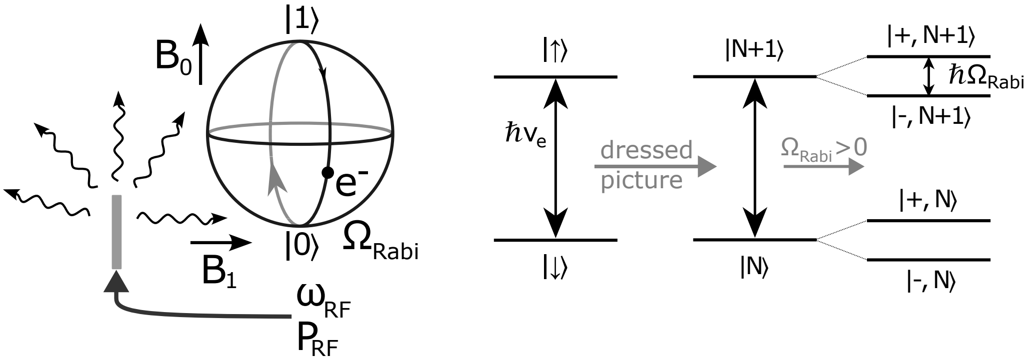

FIGURE 10 Left: A schematic of an electron in a static magnetic field B_0 experiencing Rabi oscillations due to an oscillating magnetic field B_1, with the frequency of the Rabi oscillations determined by the RF drive input to the antenna. Right: A diagram of how the energy levels change in the dressed picture, after Laucht *et al.* [19].

How, then, does dressing a qubit work in practice? While the methods depend on the platform, for a two-level system consisting of the bound electron of a P donor in Si, dressing can be done *e.g.* through a microwave drive [19]. As a microwave drive is also an excellent means of controlling a donor spin qubit, this in effect lets us kill two birds with one stone, using the same system for both dressing the spins and controlling them. A schematic of the system and its energy levels is presented in Figure 10: The energy states of $|\uparrow\rangle$ and $|\downarrow\rangle$ have been separated by a static magnetic field B_0, and the electron is made to oscillate between them at a frequency of Ω_R by an oscillating magnetic field B_1, introduced via a microwave antenna and controlled through the power P_{RF} and frequency ω_{RF} of the radio frequency signal incident to the antenna. As for the energy levels, in the absence of coupling to the dressing field, they are the degenerate $|N+1\rangle = |\downarrow, n+1\rangle, |\uparrow, n\rangle$ and $|N\rangle = |\downarrow, n\rangle, |\uparrow, n-1\rangle$ states, where n is the number of resonant photons in the dressing field and N the total number of excitations. Rabi oscillations break this degeneracy to form the states $|+, N+1\rangle = \frac{1}{\sqrt{2}}(|\downarrow, n+1\rangle + |\uparrow, n\rangle)$ and $|-, N+1\rangle = \frac{1}{\sqrt{2}}(|\downarrow, n+1\rangle - |\uparrow, n\rangle)$ from $|N+1\rangle$, and likewise $|+, N\rangle = \frac{1}{\sqrt{2}}(|\downarrow, n\rangle + |\uparrow, n-1\rangle)$ and $|-, N\rangle = \frac{1}{\sqrt{2}}(|\downarrow, n\rangle - |\uparrow, n-1\rangle)$ from $|N\rangle$. Due to the large quantity of photons in the dressing field, n is very large, and thus its value, as well as that of N, is unimportant. We are thus left with the states $|+\rangle$ and $|-\rangle$, separated by the energy $\hbar\Omega_R$.

Let us now take an excursion to look at the Hamiltonian of the initial system and how dressing changes it. We begin with the Hamiltonian of an electron experiencing Zeeman splitting:

$$H = \frac{1}{2}\hbar\gamma_e B_0 \sigma_z, \tag{46}$$

where γ_e is the electron gyromagnetic ratio, B_0 is the magnitude of the magnetic field, and σ_z is the Pauli matrix for the z axis. We have assumed that $\overrightarrow{\mathrm{B}_0} \parallel \hat{z}$.

When we add the dressing field B_1, the Hamiltonian in the laboratory coordinates becomes

$$H = \frac{1}{2}\hbar\gamma_e[B_0\sigma_z + B_1\cos(\omega_{RF}t)\sigma_x], \tag{47}$$

where ω_{RF} is the frequency of the RF drive and σ_x the Pauli matrix for the x axis. For convenience, we shall henceforth denote $\alpha = \frac{1}{2}\omega_{RF}t$.

Next, we go to the rotating frame with $\hat{U} = e^{i\alpha\sigma_z}$. The new Hamiltonian becomes $\hat{H} = \hat{U}\hat{H}_{old}\hat{U}^\dagger + i\hbar\frac{\partial\hat{U}}{\partial t}\hat{U}^\dagger$. Let us consider $i\hbar\frac{\partial\hat{U}}{\partial t}\hat{U}^\dagger$ first:

$$\begin{aligned} i\hbar\frac{\partial\hat{U}}{\partial t}\hat{U}^\dagger &= i\hbar\frac{i\alpha\sigma_z}{t}\hat{U}\hat{U}^\dagger && (48)\\ &= -\hbar\frac{\alpha}{t}\sigma_z && (49)\\ &= -\hbar\frac{\omega_{RF}}{2}\sigma_z && (50) \end{aligned}$$

We next consider $\hat{U}\hat{H}\hat{U}^\dagger$. $\hat{U} = e^{i\alpha\sigma_z}$ can, based on Euler's formula, also be written as $\cos\alpha I + i\sin\alpha\sigma_z$, from which we can see that $[\hat{U}, \sigma_z] = 0$, as I is the identity matrix. Thus for $\hat{U}\hat{H}\hat{U}^\dagger = \frac{1}{2}\hbar\gamma_e U[B_0\sigma_z + B_1\cos(2\alpha)\sigma_x]U^\dagger$, the product for the first term in square brackets is $\hat{U}[B_0\sigma_z]\hat{U}^\dagger = B_0\sigma_z$. The second term is

$$\begin{aligned}\hat{U}B_1\cos{(2\alpha)}\sigma_x\hat{U}^\dagger =& B_1\cos{(2\alpha)}\hat{U}[\sigma_x]\hat{U}^\dagger\\ =& B_1\cos{(2\alpha)}[(\cos\alpha I + i\sin\alpha\sigma_z)\sigma_x(\cos\alpha I + i\sin\alpha\sigma_z)^\dagger]\\ =& B_1\cos{(2\alpha)}[\cos^2\alpha\sigma_x + \sin^2\alpha\sigma_z\sigma_x\sigma_z\\ & - i\cos\alpha\sin\alpha\sigma_x\sigma_z + i\cos\alpha\sin\alpha\sigma_z\sigma_x]\\ =& B_1\cos{(2\alpha)}[(\cos^2\alpha - \sin^2\alpha)\sigma_x - 2\cos\alpha\sin\alpha\sigma_y]\\ =& B_1\cos{(2\alpha)}[\cos 2\alpha\sigma_x - \sin 2\alpha\sigma_y]\end{aligned}$$

where σ_y is the Pauli matrix for the y axis. As the Pauli matrices are

$$\sigma_x = \begin{pmatrix}0 & 1\\ 1 & 0\end{pmatrix}, \sigma_y = \begin{pmatrix}0 & -i\\ i & 0\end{pmatrix}, \sigma_z = \begin{pmatrix}1 & 0\\ 0 & -1\end{pmatrix},$$

we can thus write $B_1\cos{(2\alpha)}\hat{U}[\sigma_x]\hat{U}^\dagger$ as

$$B_1\cos{(2\alpha)}\hat{U}[\sigma_x]\hat{U}^\dagger = B_1\cos{(2\alpha)}\left[\begin{pmatrix}0 & \cos{(2\alpha)}\\ \cos{(2\alpha)} & 0\end{pmatrix} + \begin{pmatrix}0 & i\sin{(2\alpha)}\\ -i\sin{(2\alpha)} & 0\end{pmatrix}\right] \tag{51}$$

$$= B_1\cos{(2\alpha)}\begin{pmatrix}0 & e^{i2\alpha}\\ e^{-i2\alpha} & 0\end{pmatrix} \tag{52}$$

$$= B_1\begin{pmatrix}0 & \frac{e^{i4\alpha+1}}{2}\\ \frac{e^{-i4\alpha+1}}{2} & 0\end{pmatrix} \tag{53}$$

As $\alpha = \frac{1}{2}\omega_{RF}t$, $\lim_{t\to\infty} e^{\pm i4\alpha} = 0$, and thus we get

$$B_1\cos{(2\alpha)}\hat{U}[\sigma_x]\hat{U}^\dagger \longrightarrow B_1\begin{pmatrix}0 & \frac{1}{2}\\ \frac{1}{2} & 0\end{pmatrix} \tag{54}$$

$$= \frac{B_1}{2}\sigma_x \tag{55}$$

The full Hamiltonian in the rotating frame, $\hat{H} = \hat{U}\hat{H}_{old}\hat{U}^\dagger + i\hbar\frac{\partial\hat{U}}{\partial t}\hat{U}^\dagger$, is thus

$$\hat{H} = \hat{U}\hat{H}_{old}\hat{U}^\dagger + i\hbar\frac{\partial\hat{U}}{\partial t}\hat{U}^\dagger \tag{56}$$

$$= \frac{1}{2}\hbar\gamma_e\left[B_0\sigma_z + \frac{B_0}{2}\sigma_x\right] - \hbar\frac{\omega_{RF}}{2}\sigma_z \tag{57}$$

$$= \frac{1}{2}\hbar\gamma_e\left[\left(B_0 - \frac{\omega_{RF}}{\hbar\gamma_e}\right)\sigma_z + \frac{B_1}{2}\sigma_x\right] \tag{58}$$

$$= \frac{1}{2}\hbar\left[\left(\gamma_e B_0 - \omega_{RF}\right)\sigma_z + \Omega_R\sigma_x\right], \tag{59}$$

where we have designated the Rabi frequency as $\Omega_R = \frac{1}{2}\gamma_e B_1$. We then finally change our computational basis with a second unitary transformation with $\hat{U} = e^{-i\frac{\pi}{4}\sigma_y}$. As $\hat{U}$ has no time dependence, $i\hbar\frac{\partial\hat{U}}{\partial t}\hat{U}^\dagger = 0$. This leaves us with $\hat{U}\hat{H}_{old}\hat{U}^\dagger$:

$$\begin{aligned}
\hat{U}\hat{H}_{old}\hat{U}^{\dagger} &= \frac{1}{2}\hbar e^{-i\frac{\pi}{4}\sigma_y}\left[(\gamma_e B_0 - \omega_{RF})\,\sigma_z + \Omega_R\sigma_x\right](e^{-i\frac{\pi}{4}\sigma_y})^{\dagger} \\
&= \frac{1}{2}\hbar\left[(\gamma_e B_0 - \omega_{RF})\,e^{-i\frac{\pi}{4}\sigma_y}\sigma_z(e^{-i\frac{\pi}{4}\sigma_y})^{\dagger} + \Omega_R e^{-i\frac{\pi}{4}\sigma_y}\sigma_x(e^{-i\frac{\pi}{4}\sigma_y})^{\dagger}\right] \\
&= \frac{1}{2}\hbar\left[(\gamma_e B_0 - \omega_{RF})\,\sigma_x + \Omega_R(-\sigma_z)\right]
\end{aligned}$$

Here we have made the eigenstates of the driven system, $|+\rangle$ and $|-\rangle$, the basis states of the new Hamiltonian [19, 50], so that the Hamiltonian in the dressed basis is

$$H = \frac{1}{2}\hbar\left[(\gamma_e B_0 - \omega_{RF})\,\sigma_x - \Omega_R\sigma_z\right] \tag{60}$$

We now have a two-level system whose energy level splitting is easily tunable. This is our qubit. A variety of quantum algorithms can be performed on it through *e.g.* microwave pulses [19]. But once we have completed our calculation, how do we extract the result?

3.4 Coupling spin to mechanics

A single donor spin in an infinite slab of silicon might have its spin state forever shrouded from knowledge, but our spin need not live in such an isolated neighborhood. While several readout mechanisms have been proposed and demonstrated, such as a single electron transistor [19], we shall choose a mechanical system.

Let us begin by seeing how this coupling affects the Hamiltonian. Equation 3.3 shows the pure spin Hamiltonian; if we couple the spin to the mechanics, two new terms will appear: one for the mechanics alone and one for the spin-mechanics coupling. The mechanical term is $\hbar\omega_m\hat{b}^{\dagger}\hat{b}$ familiar from Chapter 2. Later it will be shown that the spin-mechanics coupling term is $\frac{\hbar\lambda}{2}\left(\hat{b}^{\dagger}+\hat{b}\right)\sigma_z$, where λ describes the strength of the coupling. In the rotating frame this then becomes $-\frac{\hbar\lambda}{2}\left(\hat{b}^{\dagger}+\hat{b}\right)\sigma_x$, so that the full Hamiltonian is

$$H = \frac{\hbar}{2}\left[\Omega_R\sigma_z + \Delta\nu\sigma_x + 2\omega_m\hat{b}^{\dagger}\hat{b} - \lambda\left(\hat{b}^{\dagger}+\hat{b}\right)\sigma_x\right], \tag{61}$$

where $\Delta\nu$ is the microwave detuning between the frequency of the RF drive and the bare qubit $\Delta = \omega_{RF} - \gamma_e B_0$.

Now it is time for a brief excursion on what the Pauli matrices mean in context. Coherent coupling involves σ_x, not σ_z. Consequently, for us to be able to transfer spin information to the mechanics and thence to the optics, our spin must couple through σ_x. As discussed for Equation 3.3, this requires a change in computational basis from $|\uparrow\rangle$ and $|\downarrow\rangle$ to $|+\rangle$ and $|-\rangle$.

Let us now review the possibilities of dressing. The static B_0 parts the energies of $|\uparrow\rangle$ and $|\downarrow\rangle$ and the oscillating B_1 causes the electron to nutate at the Rabi frequency Ω_R. The system is tunable: B_1 and therefore Ω_R can be changed by changing the power incident to the RF antenna.

The aforementioned tunability lets us alter Ω_R to bring it in and out of resonance with the resonance frequency of the mechanical resonator ω_m. When $\Omega_R = \omega_m$, excitations can coherently transfer between the spin state and the mechanical state. With a mechanical resonator in the ground state (*i.e.* with no excess excitations present), this could be used for excitation transfer between two spins via phonons [51]. At the dispersive limit, where $\Delta = |\omega_m - \Omega_R| > \sqrt{n_{th}}\lambda$, there is no coherent excitation transfer, but the spin state affects the mechanical resonance frequency so that there is a shift $\Delta\omega_m$, the direction of which depends on the spin state.

Of course, this picture is agnostic to the method used to couple the spins to the mechanics. We have experimentally investigated two means of achieving this coupling: strain and magnetic field gradient.

3.4.1 Strain coupling

Mechanical motion of a structure with respect to itself, such as an oscillating beam or the breathing mode of a levitating particle, involves deformation of the lattice to allow for deformation of the structure. Motion-induced strain is thus an intrinsic part of any clamped mechanical resonator. On the atomic level, the deformation of the lattice will also deform the wave function of the donor electron, as shown schematically in Figure 11. This allows us to couple the state of the electron to the mechanical motion.

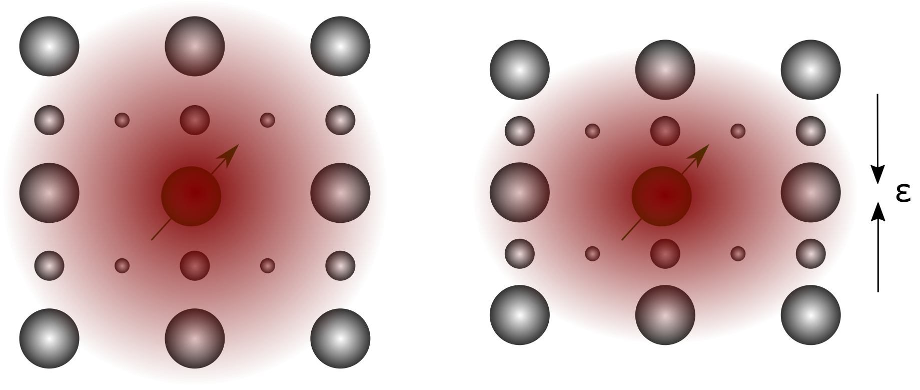

FIGURE 11 A schematic view of strain coupling that depicts how the movement of the lattice causes changes to the electron wave function. The grey circles are Si atoms, the circle in the center with an arrow through it (representing nuclear spin) is a donor atom, and the red cloud is the electron wave function. Note that in reality, the wave function stretches over four lattice constants rather than just one.

What actually happens to the electron wave function has been traditionally explained via the valley repopulation model. Si has six degenerate conduction band valleys. Under uniaxial strain, this degeneracy is lifted, so that the valleys have different energy levels and thus electron populations [52]. As a result, the doublet excited state is admixed into the singlet ground state (a change in the hyperfine constant A), which affects the resonance frequency of the electron [52]. The magnitude of this shift is dependent on the strain, and under the valley repopulation model, the shift per strain Ξ for small strains has been considered quadratically dependent on the strain, meaning that small strains lead to extremely small shifts. However, recent experimental results show that, *contra* the valley repopulation model, the shift for small strains is linear due to a hydrostatic strain contribution, leading to coupling strengths of up to $\Xi = 23$ GHz/strain for ^{31}P and up to $\Xi = 150$ GHz/strain for ^{209}Bi [53].

Let us now look at the coupling strengths achievable in a representative system. COMSOL simulations by Simeoni Ahopelto show that our devices, as introduced in Section 2.5, can be engineered to have strains of up to $\epsilon \approx 5 \times 10^{-9}$, leading to coupling rates $\lambda = \Xi\epsilon$ of around 750 Hz per ^{209}Bi donor in high-strain regions [54]. An example of such a strain engineered device can be seen in Figure 12.

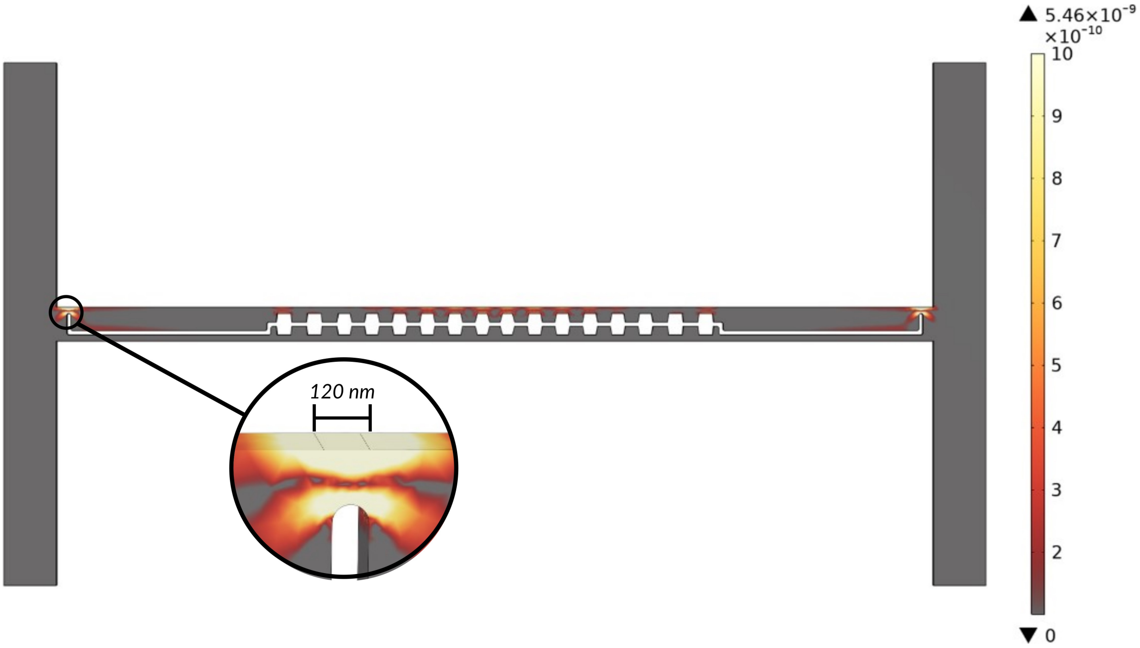

FIGURE 12 An example COMSOL strain simulation by Simeoni Ahopelto for a strain engineered structure. The beam has a mechanical resonance frequency of 5.4 MHz and maximum strain per x_{ZPF} of 5.46×10^{-9}. Inset: a close-up of the high-strain region at the end. To appear in [54].

Now let us think about the shift in mechanical resonance frequency $\Delta\omega_m$. Unfortunately, $\Delta\omega_m \neq \lambda$; instead, the frequency shift at the dispersive limit is $\Delta\omega_m = \lambda^2/4\Delta$ [55]. If the frequency detuning $\Delta \gg \sqrt{n_{th}}\lambda$, where n_{th} is the number of thermal phonons, then

$$\Delta\omega_m \propto \frac{\lambda}{\sqrt{n_{th}}}. \tag{62}$$

At the few-Kelvin temperatures we operate at, $\sqrt{n_{th}} \approx 80$. One spin would thus cause a shift of c. 9 Hz for ^{209}Bi and c. 1 Hz for ^{31}P. For a shift to be visible, however, it must be larger than the intrinsic spread of the frequency Γ_m as well as the resolution of our instrumentation; for us, the minimum detectable frequency shift $\Delta\omega_m$ is c. 500 Hz, so a single donor will not produce a signal we can detect. With a sufficient amount of donors in the high strain region, however, we could see the ensemble signal. For ensemble signals, the magnitude of the shift in the mechanical resonance frequency $\Delta\omega_m$ depends on the size of the ensemble N and the spin polarization level $\langle\sigma_z\rangle$, which depends on the temperature and the magnetic field, so that if *e.g.* $|\uparrow\rangle$ causes a shift of $\frac{\lambda^2}{\Delta}$, an ensemble of N spins would cause a shift of $\Delta\omega_m = \frac{N\lambda^2}{\Delta}\langle\sigma_z\rangle$, as per the Tavis-Cummings model. The spin polarization level $\langle\sigma_z\rangle$ depends on the temperature T and the energy levels E of the spin, so that if the probability of finding the spin in state $p_i = e^{-E_i k_B T}/\sigma_j e^{-E_j/k_B T}$, where k_B is the Boltzmann constant, then the spin polarization level for an electron is

$$\begin{aligned}\Big(p_{|\uparrow\Downarrow\rangle} + p_{|\uparrow\Uparrow\rangle}\Big) &- \Big(p_{|\downarrow\Downarrow\rangle} + p_{|\downarrow\Uparrow\rangle}\Big) \\ &= \frac{\left(e^{-E_{|\uparrow\Downarrow\rangle}/k_BT} + e^{-E_{|\uparrow\Uparrow\rangle}/k_BT}\right) - \left(e^{-E_{|\downarrow\Downarrow\rangle}/k_BT} + e^{-E_{|\downarrow\Uparrow\rangle}/k_BT}\right)}{e^{-E_{|\uparrow\Downarrow\rangle}/k_BT} + e^{-E_{|\uparrow\Uparrow\rangle}/k_BT} + e^{-E_{|\downarrow\Downarrow\rangle}/k_BT} + e^{-E_{|\downarrow\Uparrow\rangle}/k_BT}}\end{aligned} \tag{63}$$

At a temperature of 3 K and a magnetic field of 0.7 T, $\langle\sigma_z\rangle = -0.16$, *i.e.* there are more electron spins in $|\downarrow\rangle$ than $|\uparrow\rangle$. Our region of highest strain is of the order of 10^{-15} cm^3; a high doping level of 10^{18} Bi ions/cm^3 would give us $N = 10^3$ donor spins in this region and thus, for the strain-engineered device above, a frequency shift $\Delta\omega_m = \frac{N\lambda}{\sqrt{n_{th}}}\langle\sigma_z\rangle = \frac{10^3\times750}{80} \times (-0.16)$ Hz $= -1.5$ kHz. Our current resonator designs have a strain ϵ and thus coupling λ an order of magnitude smaller, which would still lead to a potentially observable frequency shift of $\Delta\omega_m = -150$ Hz.

However, after two years of measurements on a variety of samples, we have yet to see a shift in the mechanical resonance frequency caused by the spin state. We cannot fully rule out experimental limitations, *e.g.* line losses or fabrication issues in the RF cavity, discussed more in detail in Section 3.5. It is also possible that, as we are working with ensemble doped samples, we are running into the spin dephasing rate, where the presence of a large quantity of spins causes inhomogenous broadening, where their coherence time is reduced by the spins all experiencing slightly different environments, leading to them all having slightly different resonance frequencies and thus the ensemble having a large linewidth. In addition, increasing the number of spins increases the influence of other broadening mechanisms, *e.g.* dipole-dipole interactions between the spins [56], so that the coherence time becomes so much less than the measurement time that we do not see the signal.

3.4.2 Magnetic field gradient coupling

We thus turned our sights on another coupling method: magnetic field gradient coupling. This time, the coupling comes from the physical motion of the resonator, rather than the strain this motion causes. A micromagnet is placed on a balcony next to the center of the resonator so that spins there will be in a region of strong magnetic field gradient. As the resonator moves, the spins within it will experience a magnetic field that depends on $\hat{x}$, thus coupling the spin state to the mechanical motion.

The strength of this coupling depends on the zero point fluctuation amplitude x_{ZPF} of the resonator (*i.e.* the amplitude generated by a single mechanical exitation) and the magnetic field gradient, so that $\lambda = \gamma_e \nabla \overrightarrow{B} x_{ZPF}$. The maximization of both $\nabla \overrightarrow{B}$ and x_{ZPF} through device design to improve the coupling is discussed more in Chapter 4. For now, it suffices to say that with values currently achievable through fabrication, we get coupling strengths of up to 1 kHz, on the boundary of being sufficient for single spin readout, but definitely adequate for readout of an ensemble small enough not to suffer from inhomogenous broadening, unlike with strain coupling.

3.5 Experimental concerns

It is all well and good to perform a gedankenexperiment in the cradle of one's mind, free of noise sources and with no limitations to equipment or funding save for the bounds of one's imagination. Reality, however, is rarely that simple or straightforward. Thus the experiment must overcome a number of stumbling blocks as it matures from thought to practice.

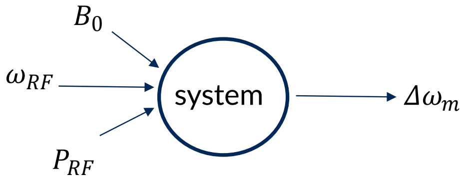

FIGURE 13 A black box model of the spin state measurement.

At its simplest, the spin measurement of ours can be thought of as a black box system, as described in Figure 13. The input parameters are the static magnetic field B_0 and the frequency ω_{RF} and power P_{RF} of the microwave drive used to drive the Rabi oscillations. The correct combination of these will yield a shift in the mechanical resonance frequency ω_m. The parameter field is thankfully not wholly open: ω_{RF} is determined by the resonance frequency of the RF antenna — it is useless to input off-resonance signal, as it will simply be reflected back — and ideal scenario values for B_0 and P_{RF} can be calculated.

The static magnetic field B_0 induces Zeeman splitting that separates the energy levels of $|\uparrow\rangle$ and $|\downarrow\rangle$. This is comparatively simple to validate experimentally.

By introducing a reference material, such as DPPH [57], to our sample space and then doing an electron paramagnetic resonance (EPR) measurement, it is possible to calibrate the value of the magnetic field. The required value of the field can be calculated from the electron gyromagnetic ratio $\gamma_e \approx 28$ GHz/T so that if the resonance frequency of the antenna is *e.g.* 14 GHz, then the value of B_0 that will lead to the microwave field being able to induce Rabi oscillations is $B_0 = \frac{\gamma_e}{f_{RF}} = \frac{28}{14} = 0.5$ T. A more easily achievable 0.3 T would correspond to a frequency of 8.4 GHz.

The necessary value for the power of the RF drive P_{RF}, on the other hand, requires more thought. The purpose of the RF drive is to induce an oscillating magnetic field B_1 which drives the spins at a frequency Ω_R dependent on the amplitude of B_1 and thus the value of P_{RF}. The key figure of merit is the power-to-field conversion factor C_p of the RF delivery mechanism, defined as $C_p = B_1/\sqrt{P_{RF}}$ [58]. The resulting Rabi frequency can be calculated with $\Omega_R = \frac{1}{\sqrt{2}}\gamma_e B_1 = \frac{1}{\sqrt{2}}\gamma_e C_p \sqrt{P_{RF}}$, where γ_e is the electron gyromagnetic ratio [59]. The Rabi frequency thus depends linearly on B_1, which depends on the square root of P_{RF} with a scaling constant C_p; to double the Rabi frequency, one must increase the power incident in the antenna fourfold.

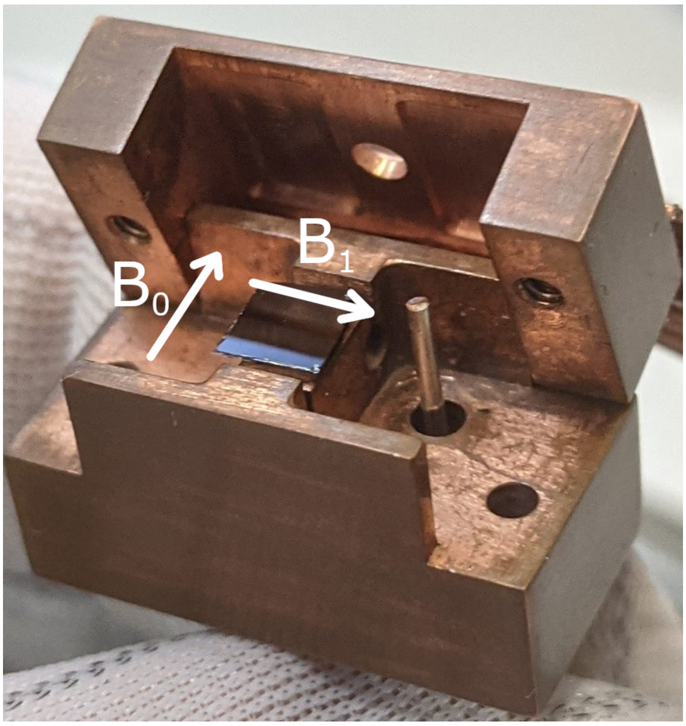

FIGURE 14 A photograph of the RF cavity with a test chip within it. The directions of the external magnetic field B_0 and cavity magnetic field B_1 have been drawn. Photograph taken by James Slack-Smith at UNSW.

So far, so good. However, we now encounter practical issues: depending on the RF cavity's C_p and the mechanical frequency ω_m we wish to match, the RF power P_{RF} required to achieve $\Omega_R \approx \omega_m$ might be prohibitively large. Changing this on the one end — lowering ω_m or increasing C_p — would require fabricating an entirely new sample or RF cavity. On the other end, unless one wishes to invest dearly in a high power RF source, one could buy a power amplifier in addition to ensuring that line losses from source to sample are minimal.

In addition to limitations in device specifications, there is also the matter of inhomogenity. For instance, a B_1 field inhomogenous over the sample space would give the donor spins different Rabi frequencies. This would mean that all the spins are constantly going in and out of phase with each other, causing dephasing noise. We suspect that this is currently the main noise source in our measurements and possibly the reason we have yet to see a signal from the spins.

4 FABRICATION

Anything that wishes to become reality must first pass the proof of concept stage with a prototype, and all prototypes must first be made. While not all the samples presented in the articles have been fabricated by me or even in Jyväskylä, our research, especially article [**PIII**], has been towards creating a sample for demonstrating magnetic field gradient mediated optomechanical readout of the spin state. I have thus chosen to dedicate a chapter to device fabrication, including as much detail and as many numbers as reasonable so as to aid the work of any future experimentalist struggling on the same path.

4.1 Device design

While there are many forms of optomechanical structure, we use a sliced nanobeam photonic cavity, as shown in Figure 15. The antisymmetric "breathing" mode of the two halves of the beam has a large optomechanical coupling of up to 53 MHz in simulations [60], with experimental realizations of 25 MHz [61, 62]. These beams can be made extremely floppy with a large x_{ZPF} of the range of 43 fm [61]. As the magnetic field gradient coupling explained in Chapter 3.3 depends upon the x_{ZPF}, this is an extremely useful property to have.

Our target optical resonance is at 1550 nm (193.4 THz) for ease of integrating the final devices with telecom networks, enabling long-distance data transfer. This central cavity is bounded by two Bragg mirrors, to which there is a smooth transition. The mechanical frequency of the resonator can be controlled by choosing the length of the beam.

The structures are fabricated on a silicon on insulator (SOI) wafer, which consists of, top to bottom, a Si device layer, for us typically 220 nm thick, a 3 μm buried layer of SiO_2 (the titular insulator), and a handle layer of Si some hundreds of μm thick. Due to the lattice mismatch between Si and SiO_2, the device layer is under constant strain [63, 64]. This strain is not useful for the aforementioned strain coupling method, as the strain we desire there is localized strain

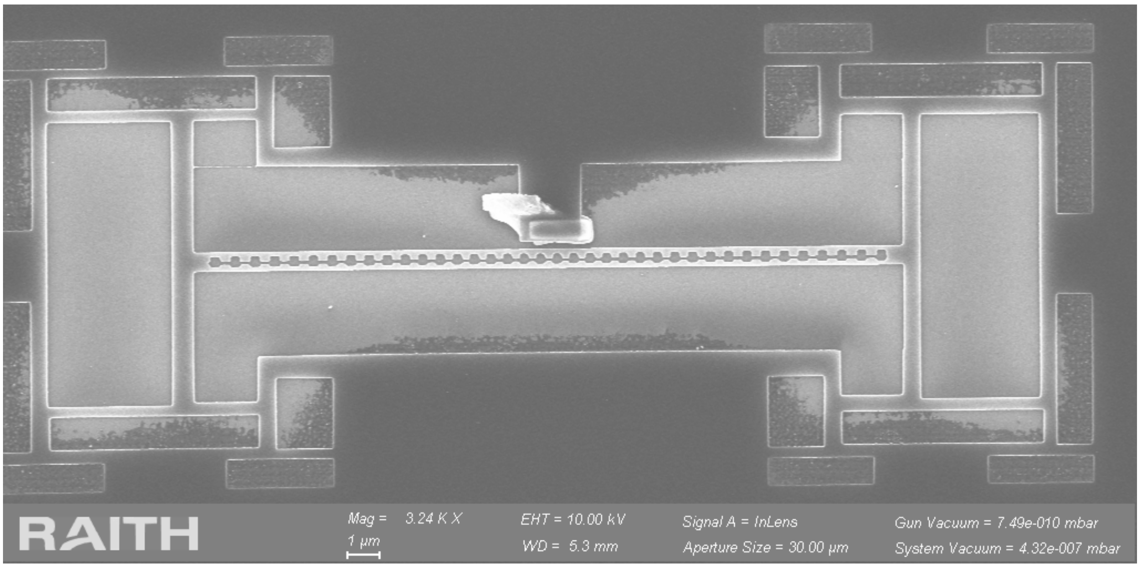

FIGURE 15 A SEM image of a split photonic crystal nanobeam with a magnet, as used in [**PIII**].

that depends on the phase of the nanobeam's mechanical motion, not homogenous constant strain that is liable to cause buckling in the nanobeams. As a result, to mitigate the effects of this undesired strain, we must utilize soft clamping, where the ends of the beam are not attached directly to the support, but rather to a branching binary tree, each end of which eventually attaches to the support [65]. Our realization of such a structure can be seen in Figures 4 and 15.

Of course, this is not the end of the story. In addition to the strain relief structure, our structures have several parts we can adjust. The core is a one-dimensional photonic crystal structure, whose geometric properties (such as periodicity) affect the optical resonance frequency of the cavity. On each end is a Bragg mirror, which is a photonic crystal with a band gap sufficiently offset from that of the central cavity so that light of the resonance frequency of the central cavity is reflected back to the center. To minimize losses, the transition in cavity characteristics between core and mirror is not abrupt, but gradual. The grading from cavity to mirror is currently done by grading the periodicity of the photonic crystal, when one can receive better optical quality factors $Q = \frac{\omega_c}{\kappa}$ through keeping the phase velocity $v = \frac{\omega}{k} = \frac{\omega}{\pi a}$ and thus the periodicity a constant by grading *e.g.* the width of the beam instead [66]. This, as well as methods for increasing x_{ZPF}, will be dealt with more in depth in the upcoming Master's thesis of Simeoni Ahopelto [54].

For the magnetic field gradient coupling, we obviously also need a magnetic field source near the beam. Micromagnets are a convenient way of introducing an on-chip source of magnetic field. As the magnet cannot levitate, we need to include a Si balcony in our designs to bring it close to the beam.

In Figure 16 I show COMSOL simulations (performed by Teemu Loippo) on the effects of the magnet geometry and thickness on the magnetic field gradient. The geometry with the highest magnetic field gradient was the humble and easy to fabricate rectangle. Values of the gradient for select thicknesses of square magnet are shown in Figure 16b. As there was no major change to the magnetic field gradient between a thickness of 210 nm and 310 nm, a target thickness of c. 250 nm was chosen to solidly land in the intermediate range.

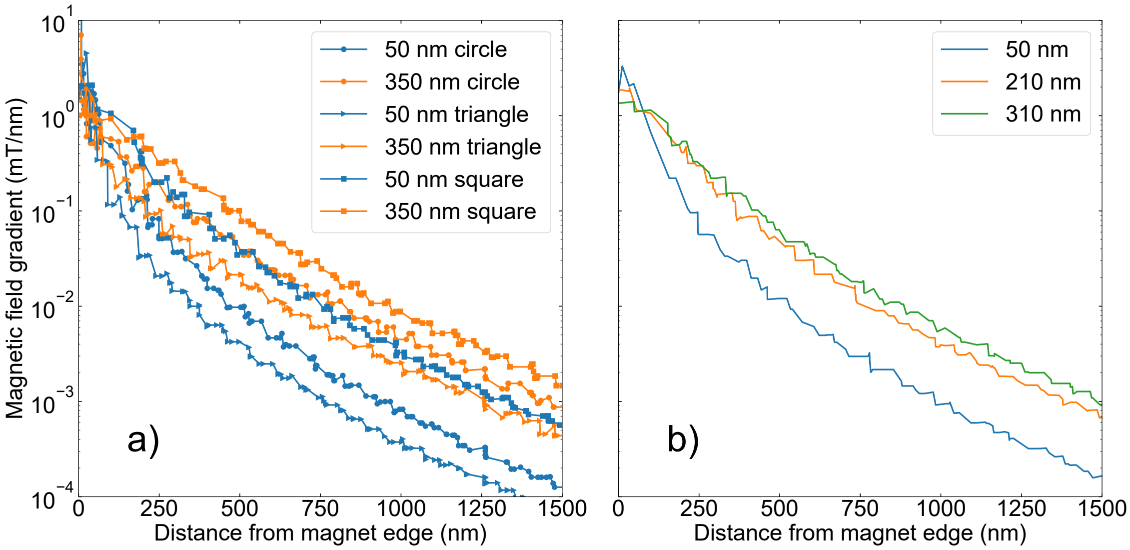

FIGURE 16 a) The magnetic field gradient at select magnet thicknesses for three magnet geometries: rectangle, circle, and triangle (apex pointing toward increasing distance). b) The magnetic field gradient as a distance from the edge of a square 500 nm by 500 nm Ni magnet for three representative thicknesses of magnet. For both figures, the gradient is taken at the bottom plane of the magnet/top plane of the Si.

As the beam needs to move with respect to the magnet, there are limitations to how close to the magnet the beam can be placed. A realistic minimum distance of 150 nm would give a gradient $\nabla \overrightarrow{B}$ of 1 mT/nm for a magnet in our target thickness range. Coupled with an x_{ZPF} of 80 fm [60], this would give us couplings $\lambda = \gamma_e \nabla \overrightarrow{B} x_{ZPF}$ of up to 2.23 kHz per spin, an order of magnitude higher than for strain coupling. This coupling would give a change in mechanical resonance frequency $\Delta\omega_m = \lambda/\sqrt{n_{th}}$ of 28 Hz.

For the magnet itself, we obviously needed a magnetic material. We chose nickel due to its availability and nontoxic nature, though other ferromagnetic substances would also work for the purpose. Had we known how long it would take to fabricate working samples, we probably would have ordered something with a higher magnetic permeability to begin with, *e.g.* permalloy. Geometry-wise, there is little improvement available; future increases in the magnetic field gradient will have to come from magnet material choice and placing the magnet closer to the nanobeam.

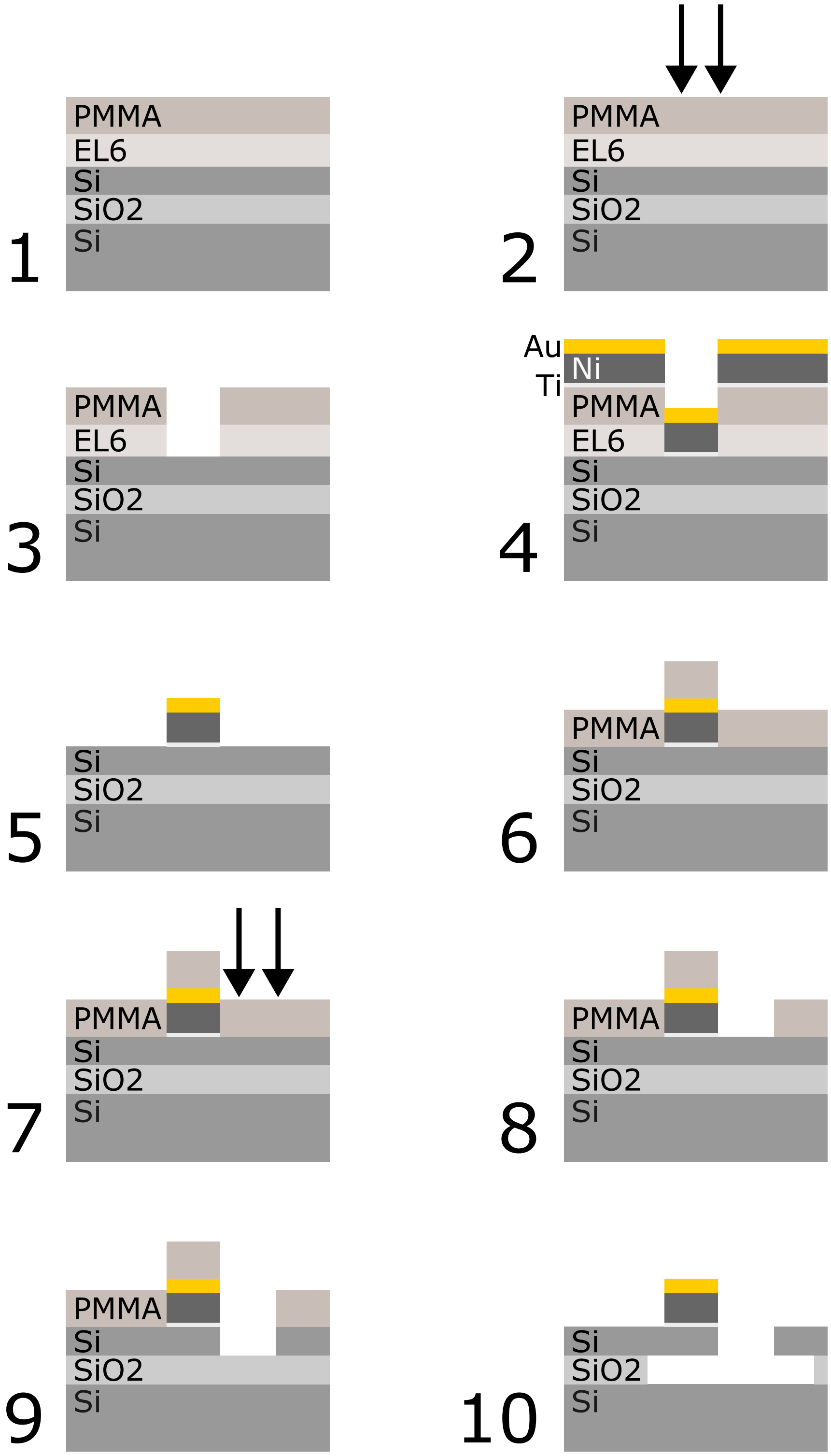

FIGURE 17 Stepwise schematic of the full magnet sample fabrication procedure. 1. Resist spinning for the magnet patterning (Electra not shown). 2. EBL patterning of magnets. 3. Development. 4. Metal deposition. 5. Liftoff. 6. Resist spinning for the beam patterning (Electra not shown). 7. EBL patterning of beams. 8. Development. 9. Si etch. 10. Structure release by HF etch of buried SiO_2.

4.2 Micromagnet fabrication

Any multi-phase fabrication procedure must think about optimizing not just each step of each phase, but the order of phases. Here we have two phases of fabrication: the nanobeam and the micromagnet. If we fabricate the magnets first, then the issue will be protecting the metal from the HF we use to suspend the beams. If we fabricate the beams first, then the issue becomes depositing the resist necessary for magnet fabrication. While there is a method to backfill resist beneath suspended structures [67], we chose not to use it due to concerns that our beams might not survive the spinning necessary for acquiring an even layer of resist. We thus unusually for the field fabricate the magnets first and only then pattern the Si. The schematic of the full fabrication procedure can be found in Figure 17. The magnet fabrication consists of steps 1 through 5.

The fabrication thus begins with spinning resist on the silicon chip (step 1) and patterning the magnets (step 2). As the magnet will be thick, we want a thick layer of layer of resist for ease of lift-off. We use a c. 200 nm layer of EL6 copolymer on the bottom, followed by a c. 220 nm layer of 950k PMMA A4. As the magnets are relatively large in feature size, this is sufficient for patterning; however, the thick layer of polymer means that the electron beam used for patterning causes a great deal of charging effects, making focusing and stigmating the electron beam incredibly annoying. As a result, we also spin a thin layer of Allresist Electra 92 on top to help with charge carrier mobility.

We then use the SEM for electron beam lithography (EBL) and draw alignment markers and magnets on the chip. In addition to a large central alignment marker and a square marker to the side to clearly break mirror symmetry, each array of beams (each block) has its own, smaller alignment markers. All of these are then drawn with a dose of 180 $\mu C/cm^2$, though this process is not terribly dose-sensitive.

After exposure, the Electra is rinsed off with deionized water and the resist stack developed (step 3) first with 20 s in a MIBK:IPA solution to develop the PMMA and then 10 s in developer 2, with developement stopped with 1 min in an IPA bath after each stage.

Next comes the metal deposition (step 4). An issue we had early on was that all our Ni, magnets included, would float off during the liftoff rather than leave or remain as desired. Currently, we have solved this by beginning our metal deposition by depositing a c. 5 nm layer of Ti to promote adhesion, so that the Ni is not grown directly on the Si. Before the deposition, we also place the chip in a reactive ion etcher (RIE) and exposing it to O_2 plasma for 30 s to remove residual PMMA and EL6 from the bottom of the mask so that the Ti is deposited directly on the Si substrate. We investigated a number of other means to promote adhesion in cooperation with the Ti adhesion layer, such as increasing the dosage or development time, or stripping the Si of its native oxide with a HF bath before spinning the resists on it, but none of them improved liftoff selectivity.

Then we deposit our actual magnets, a c. 250 nm thick Ni layer. Because we

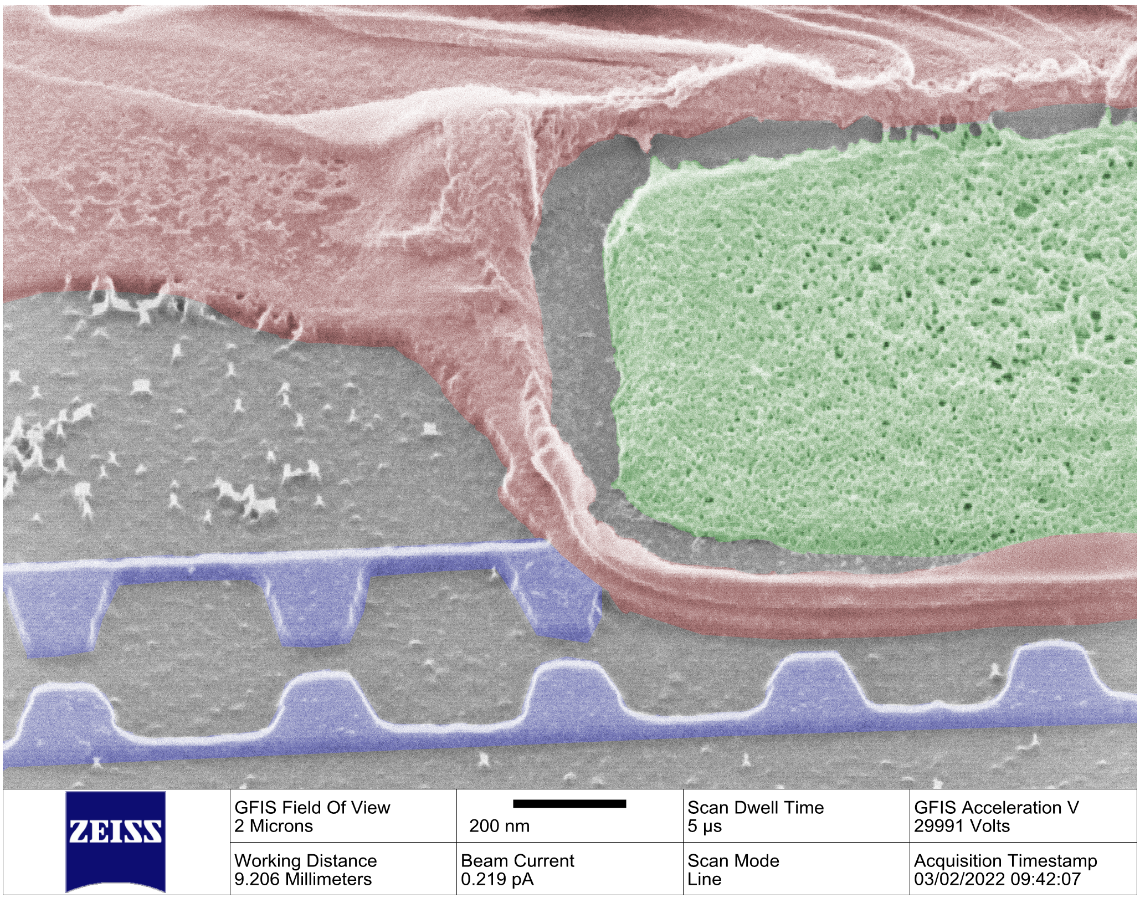

FIGURE 18 A false color tilted HIM image of a failed fabrication run with multiple issues. The nanobeam (blue) is misaligned and partially beneath the magnet, the nanobeam is overexposed and would not be able to support itself if suspended, the ICP-RIE etch process has not etched through the Si layer, meaning that the HF did not access the SiO_2 layer and the beams are not suspended, and the Ni micromagnet (green), here without an Au passivation layer on top, has become porous and shrunk dramatically, as seen in the gap between it and the balcony structure (red).

fabricate our magnets first and only then our nanobeams, the release of which involves immersing the chip in HF, we must passivate our magnets lest they be etched away or turn porous, as demonstrated in Figure 18. To do this, we cap our metal deposition with c. 25 nm of Au. The chip is then removed from the metal evaporator and left to sit. The liftoff procedure (step 5) to remove the resist and all the excess metal atop it is performed the following morning. The chip is immersed in warm acetone until the metal layer begins to flake off. At that point, a syringe may be used to squirt warm acetone from the side of the chip to speed up the process, though following the overnight rest, liftoff is usually quite painless.

All chips were checked with an optical microscope following liftoff to check for *e.g.* missing magnets or alignment markers, excess retained metal, or other defects, like the metal leaving a comet-like tail, as seen in Figure 15. There would usually be some excess metal in the corners of the chip and possibly strips attached to the alignment markers, but on the whole nothing interfering with beam fabrication.

4.3 Nanobeam fabrication

With the magnets done, we move on to fabricating the suspended nanobeams with EBL. This is shown in Figure 17, steps 6 through 10.

Again we begin by spin coating our chip, this time with a single layer of c. 220 nm of 950k PMMA A4 (step 6). As the beams involve small-scale details, ameliorating charging effects and the electron displacement they would cause is a must. For that, we spin on a thin layer of Allresist Electra 92 on top of the PMMA. We then do the EBL patterning (step 7). Depending on the mood of the SEM, doses between 135 and 150 $\mu C/cm^2$ proved successful in creating the beams. At 135 $\mu C/cm^2$ the edges of the large areas retained some residual Si, visible as ragged dark intrusions in Figures 4 and 15, but the shape of the beams best matched the design.

The introduction of the magnet generates some additional concerns for the beam patterning. For one, the presence of the balcony means there is less overall area dose in the center of the structure, necessitating the addition of an invisible box of double dosage opposite to the balcony so as to ensure that the beam is not shut in the center. Additionally, as the metal not only guards the Si beneath it from the RIE process but also Si in a small halo around it, an extra strip of double dosage is required to detach the balcony and thus the magnet from the nanobeam.

The EBL step is easily reproducible when the SEM works, but for the beams, the next step is an annoying piece of handicrafts — the development (step 8). We rinse off the Electra with deionized water and develop the resist in a MIBK:IPA solution for 30 s, after which development is stopped by a 1 min immersion in IPA. However, the beams are very sensitive to dose and development time, and while the vial of MIBK:IPA mixture has a lid on it, the IPA evaporates preferentially, increasing the concentration of the MIBK in the solution and thus making it more and more potent. As a result, the beams become overdeveloped. (With the magnets, this is less of an issue, as they have no fiddly details and are consequently less sensitive to the dose.) The times and values given above are valid for a fresh MIBK:IPA solution. For older solutions, I had to lower the development time first to 25 s and then 20 s.

At this point I would check the developed resist with an optical microscope to see whether there was anything obviously wrong. If the alignment and dosage were appropriate, the optical microscope image would look like Figure 19. While moderate overdevelopment was not visible with any of the objectives, it was possible to see if the beams were drawn adjacent to the magnets, or partially on top of them, resulting in a situation like that shown in Figure 18. The split between the beam halves is not visible, but the trapezoids between the teeth of the beam can be faintly observed on the highest magnification, as seen in Figure 19.

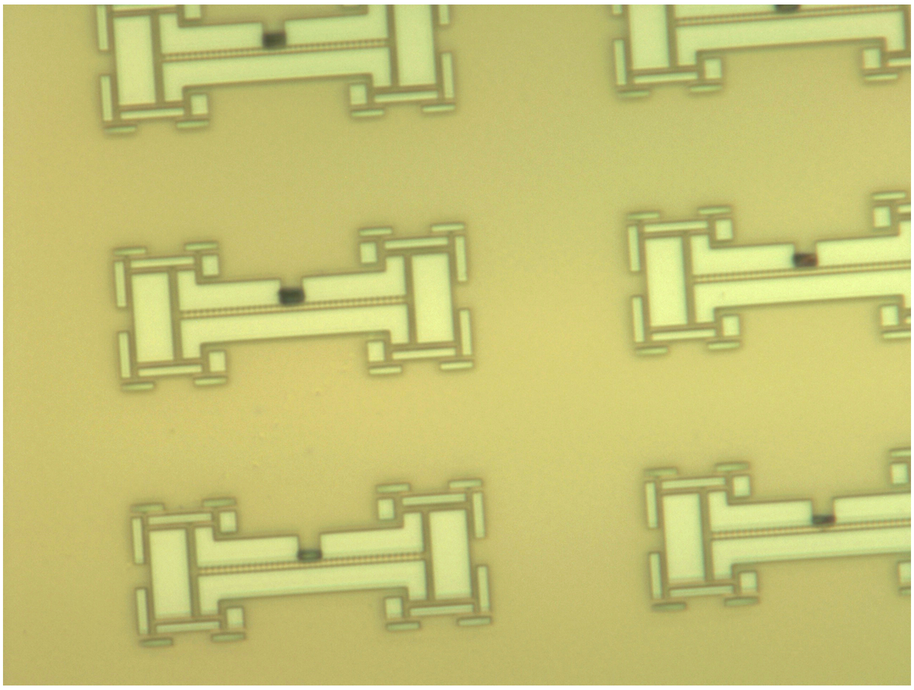

FIGURE 19 A color adjusted optical microscope image of an exposed and developed resist from step 7 in Figure 17. The beams are properly aligned with respect to the magnets, which are visible as dark smudges.

After development and checking, the Si from the exposed areas is etched with an inductively couple plasma reactive ion etcher (ICP-RIE) (step 9). The ICP-RIE is cooled down to $-100°C$ with the aid of liquid nitrogen so that we can use a cryogenic SF_6 etch, which has good vertical selectivity and smooth edges. Before etching the chip, we would first condition the chamber and carrier wafer with a 5 min etch, after which the chip would be brought into the chamber on the carrier wafer and etched for 10 min.

The last step (step 10) is the release. The chip is immersed in 48% liquid HF for 3 min to etch away the 3 µm of SiO_2 beneath the Si device layer and release the nanobeams from the substrate so that they are suspended. After the HF immersion, the chip was cleaned with four baths of deionized water before being placed in an ethanol bath for transport to a critcal point dryer. The critical point dryer is necessary lest the beam glue itself shut due to the interfacial forces generated by the drying liquid [68]. While my predecessor in fabrication managed to fabricate some devices in the $\omega_m \approx 8$ MHz range just by blowing the chip dry with a nitrogen gun, I found that without the critical point dryer, the fabrication yield for the longer, floppier 1 MHz devices was zero due to the aforementioned stiction.

5 CONCLUSION

Experimental science is, at its heart, a collection of people raising the seabed of the ocean of the unknown. We have the maps of the mountains raised behind us and the notes of our colleagues at the forefront of knowledge. Each patch of land exposed to the light of humanity's gaze might be either exactly as predicted or something revolutionary. I do not know if the ocean can ever be wholly dried — certainly not in my lifetime — but the siren call of the seabed to be raised to the surface is something I have no desire to resist.

The land reclamation project presented herein is very much a work in progress. I have charted the paths to the section targeted, but have yet to be able to lay my hands on it. Depending on how the next rounds of device design and fabrication go, the hands that first touch it might not include mine, but rather those of my successor in the group, while I abscond to different shores. Nonetheless, I hope you have found this tale of a goal that just evades the fingertips a worthwhile read and are ready to read the publications on the path towards it, presented after the references. It would be a lie to say I enjoyed every moment of walking it — I could certainly have done without any of the equipment malfunctions — but the successes have been satisfying, and there is something viscerally thrilling about rooting around in unknown territory.

To step out of the realm of metaphor, this introductory text describes a vision for a novel type of qubit optical readout mechanism and the scientific principles upon which it is based. Each paper examines a complication from the ideal.

Ion implantation, the means by which we introduce our qubits to the Si matrix, is inherently a destructive process, introducing lattice defects. Article **[PI]** deals with the effects of this deformed lattice on the optomechanical resonator design we hope to use for spin state readout. For bulk doping, this can be bypassed by having the implantation and implantation damage healing happen before fabrication, but for eventual deterministically implanted single-spin samples, implantation and thus healing the implantation damage will have to happen after fabrication.

Another intrinsic part of our system is the means by which we couple our spin state to mechanical motion. Article **[PIII]** discusses two methods, strain and magnetic field gradient, by which this can be achieved. We considered methods of optimising the coupling for both methods separately and for the micromagnets we use to create a magnetic field gradient, we investigated how much of an issue their presence would cause for the optical part of the optomechanical cavity.

Finally, article [**PII**] deals with something encountered along the way: photothermal effects. As we will be operating at high optical powers for ease of readout, absorption will occur, potentially enough to create confounding photothermal effects. While our example resonators do not have significant photothermal effects, it would be possible to design a resonator where the photothermal and radiation pressure forces exactly counteract each other, eliminating the shape of the optical spring. As this should still be responsive to spin-induced shifts of mechanical resonance frequency, this would provide an avenue for removing the confounding effect of shifts in the mechanical resonance frequency originating in the optical spring effect, caused by potential drifts in the optical resonance frequency.

Now I shall leave you to the articles, reproduced after the references. I hope you enjoy this journey of detours.

REFERENCES

[1] Jonathan P. Dowling and Gerard J. Milburn. “Quantum technology: the second quantum revolution”. en. In: *Philosophical Transactions of the Royal Society of London. Series A: Mathematical, Physical and Engineering Sciences* 361.1809 (Aug. 2003). Ed. by A. G. J. MacFarlane, pp. 1655–1674. DOI: 10.1098/rsta.2003.1227.

[2] Alan Seabaugh. “The Tunneling Transistor”. In: *IEEE Spectrum* 50.10 (Oct. 2013). Conference Name: IEEE Spectrum, pp. 35–62. DOI: 10.1109/MSPEC.2013.6607013.

[3] A. L. Schawlow and C. H. Townes. “Infrared and Optical Masers”. en. In: *Physical Review* 112.6 (Dec. 1958), pp. 1940–1949. DOI: 10.1103/PhysRev.112.1940.

[4] T. H. Maiman. “Stimulated Optical Radiation in Ruby”. en. In: *Nature* 187.4736 (Aug. 1960), pp. 493–494. DOI: 10.1038/187493a0.

[5] Jeff Hecht. “Short history of laser development”. In: *Optical Engineering* 49.9 (Sept. 2010). Publisher: SPIE, p. 091002. DOI: 10.1117/1.3483597.

[6] John G. Sulewski. “Historical Survey of Laser Dentistry”. en. In: *Dental Clinics of North America* 44.4 (Oct. 2000), pp. 717–752. DOI: 10.1016/S0011-8532(22)01317-9.

[7] Lars Jaeger. *The Second Quantum Revolution: From Entanglement to Quantum Computing and Other Super-Technologies*. en. Cham: Springer International Publishing, 2018. DOI: 10.1007/978-3-319-98824-5.

[8] James E. Tomayko. *Computers in Spaceflight: the NASA Experience*. Tech. rep. NAS 1.26:182505. NTRS Author Affiliations: Wichita State Univ. NTRS Document ID: 19880069935 NTRS Research Center: Headquarters (HQ). Wichita, Kansas: Wichita State University, Mar. 1988.

[9] Michela Paganini, Luke de Oliveira, and Benjamin Nachman. “CaloGAN: Simulating 3D high energy particle showers in multilayer electromagnetic calorimeters with generative adversarial networks”. In: *Physical Review D* 97.1 (Jan. 2018). Publisher: American Physical Society, p. 014021. DOI: 10.1103/PhysRevD.97.014021.

[10] Richard P. Feynman. “Simulating Physics with Computers”. en. In: *International Journal of Theoretical Physics* 21.12 (June 1982), pp. 467–488. DOI: 10.1007/BF02084157.

[11] Peter W. Shor. “Polynomial-Time Algorithms for Prime Factorization and Discrete Logarithms on a Quantum Computer”. In: *SIAM Review* 41.2 (Jan. 1999). Publisher: Society for Industrial and Applied Mathematics, pp. 303–332. DOI: 10.1137/S0036144598347011.

[12] Lov K. Grover. "Quantum Computers Can Search Arbitrarily Large Databases by a Single Query". In: *Physical Review Letters* 79.23 (Dec. 1997). Publisher: American Physical Society, pp. 4709–4712. DOI: 10.1103/PhysRevLett.79.4709.

[13] Frederic Magniez et al. "Search via quantum walk". In: *Proceedings of the thirty-ninth annual ACM symposium on Theory of computing*. STOC '07. New York, NY, USA: Association for Computing Machinery, June 2007, pp. 575–584. DOI: 10.1145/1250790.1250874.

[14] Juha T. Muhonen et al. "Storing quantum information for 30 seconds in a nanoelectronic device". en. In: *Nature Nanotechnology* 9.12 (Dec. 2014), pp. 986–991. DOI: 10.1038/nnano.2014.211.

[15] Lilian Childress and Ronald Hanson. "Diamond NV centers for quantum computing and quantum networks". en. In: *MRS Bulletin* 38.2 (Feb. 2013). Publisher: Cambridge University Press, pp. 134–138. DOI: 10.1557/mrs.2013.20.

[16] T.A. Kennedy et al. "Single-Qubit Operations with the Nitrogen-Vacancy Center in Diamond". en. In: *physica status solidi (b)* 233.3 (2002), pp. 416–426. DOI: 10.1002/1521-3951(200210)233:3<416::AID-PSSB416>3.0.CO;2-R.

[17] Florian Hilser and Guido Burkard. "All-optical control of the spin state in the NV^- center in diamond". In: *Physical Review B* 86.12 (Sept. 2012). Publisher: American Physical Society, p. 125204. DOI: 10.1103/PhysRevB.86.125204.

[18] David A. Hopper, Henry J. Shulevitz, and Lee C. Bassett. "Spin Readout Techniques of the Nitrogen-Vacancy Center in Diamond". en. In: *Micromachines* 9.9 (Sept. 2018). Number: 9 Publisher: Multidisciplinary Digital Publishing Institute, p. 437. DOI: 10.3390/mi9090437.

[19] Arne Laucht et al. "A dressed spin qubit in silicon". en. In: *Nature Nanotechnology* 12.1 (Jan. 2017), pp. 61–66. DOI: 10.1038/nnano.2016.178.

[20] H. Büch et al. "Spin readout and addressability of phosphorus-donor clusters in silicon". en. In: *Nature Communications* 4.1 (June 2013). Number: 1 Publisher: Nature Publishing Group, p. 2017. DOI: 10.1038/ncomms3017.

[21] M. Steger et al. "Quantum Information Storage for over 180 s Using Donor Spins in a 28Si "Semiconductor Vacuum"". In: *Science* 336.6086 (June 2012). Publisher: American Association for the Advancement of Science, pp. 1280–1283. DOI: 10.1126/science.1217635.

[22] C. C. Lo et al. "Hybrid optical–electrical detection of donor electron spins with bound excitons in silicon". en. In: *Nature Materials* 14.5 (May 2015). Number: 5 Publisher: Nature Publishing Group, pp. 490–494. DOI: 10.1038/nmat4250.

[23] M.R. Hogg et al. "Single-Shot Readout of Multiple Donor Electron Spins with a Gate-Based Sensor". In: *PRX Quantum* 4.1 (Feb. 2023). Publisher: American Physical Society, p. 010319. DOI: 10.1103/PRXQuantum.4.010319.

[24] Johannes Kepler. *De cometis libelli tres*. Typis Andreae Apergiri, 1619.

[25] Albert Einstein. "Zur quantentheorie der stralung". In: *Phys. Ges. Zurich.* 18 (1916), p. 47.

[26] Gerard J. Milburn and Warwick P. Bowen. *Quantum Optomechanics*. Boca Raton: CRC Press, Dec. 2015. DOI: 10.1201/b19379.

[27] Colin Robert McInnes. "Solar radiation pressure". en. In: *Solar Sailing: Technology, Dynamics and Mission Applications*. Ed. by Colin Robert McInnes. Astronomy and Planetary Sciences. London: Springer, 1999, pp. 32–55. DOI: 10.1007/978-1-4471-3992-8_2.

[28] Markus Aspelmeyer, Tobias J. Kippenberg, and Florian Marquardt. "Cavity optomechanics". en. In: *Reviews of Modern Physics* 86.4 (Dec. 2014), pp. 1391–1452. DOI: 10.1103/RevModPhys.86.1391.

[29] A. A. Clerk et al. "Introduction to quantum noise, measurement, and amplification". In: *Reviews of Modern Physics* 82.2 (Apr. 2010). Publisher: American Physical Society, pp. 1155–1208. DOI: 10.1103/RevModPhys.82.1155.

[30] Dries Van Thourhout and Joris Roels. "Optomechanical device actuation through the optical gradient force". en. In: *Nature Photonics* 4.4 (Apr. 2010). Number: 4 Publisher: Nature Publishing Group, pp. 211–217. DOI: 10.1038/nphoton.2010.72.

[31] K. Karrai, I. Favero, and C. Metzger. "Doppler Optomechanics of a Photonic Crystal". In: *Physical Review Letters* 100.24 (June 2008). Publisher: American Physical Society, p. 240801. DOI: 10.1103/PhysRevLett.100.240801.

[32] Mehdi Abdi and Ali Reza Bahrampour. "Improving the optomechanical entanglement and cooling by photothermal force". en. In: *Physical Review A* 85.6 (June 2012), p. 063839. DOI: 10.1103/PhysRevA.85.063839.

[33] M. Abdi, A. R. Bahrampour, and D. Vitali. "Quantum optomechanics of a multimode system coupled via a photothermal and a radiation pressure force". In: *Physical Review A* 86.4 (Oct. 2012). Publisher: American Physical Society, p. 043803. DOI: 10.1103/PhysRevA.86.043803.

[34] André G. Primo et al. "Accurate modeling and characterization of photothermal forces in optomechanics". In: *APL Photonics* 6.8 (Aug. 2021), p. 086101. DOI: 10.1063/5.0055201.

[35] B. D. Hauer et al. "Dueling dynamical backaction in a cryogenic optomechanical cavity". en. In: *Physical Review A* 99.5 (May 2019), p. 053803. DOI: 10.1103/PhysRevA.99.053803.

[36] Constanze Metzger et al. "Optical self cooling of a deformable Fabry-Perot cavity in the classical limit". In: *Physical Review B* 78.3 (July 2008). Publisher: American Physical Society, p. 035309. DOI: 10.1103/PhysRevB.78.035309.

[37] R. Kubo. "The fluctuation-dissipation theorem". en. In: *Reports on Progress in Physics* 29.1 (Jan. 1966), p. 255. DOI: 10.1088/0034-4885/29/1/306.

[38] W. C. O'Mara, L. P. Hunt, and R. B. Herring. *Handbook of Semiconductor Silicon Technology*. English. 1st edition. William Andrew, Jan. 1990.

[39] J. S. Smith et al. "Ab initio calculation of energy levels for phosphorus donors in silicon". en. In: *Scientific Reports* 7.1 (July 2017). Number: 1 Publisher: Nature Publishing Group, p. 6010. DOI: 10.1038/s41598-017-06296-8.

[40] Belita Koiller, Xuedong Hu, and S. Das Sarma. "Exchange in Silicon-Based Quantum Computer Architecture". en. In: *Physical Review Letters* 88.2 (Dec. 2001), p. 027903. DOI: 10.1103/PhysRevLett.88.027903.

[41] Jessica van Donkelaar et al. "Single atom devices by ion implantation". en. In: *Journal of Physics: Condensed Matter* 27.15 (Mar. 2015). Publisher: IOP Publishing, p. 154204. DOI: 10.1088/0953-8984/27/15/154204.

[42] David N. Jamieson et al. "Deterministic doping". In: *Materials Science in Semiconductor Processing*. Advanced doping methods in semiconductor devices and nanostructures 62 (May 2017), pp. 23–30. DOI: 10.1016/j.mssp.2016.10.039.

[43] J. L. Pacheco et al. "Ion implantation for deterministic single atom devices". In: *Review of Scientific Instruments* 88.12 (Dec. 2017), p. 123301. DOI: 10.1063/1.5001520.

[44] Alexander M. Jakob et al. *Deterministic Single Ion Implantation with 99.87% Confidence for Scalable Donor-Qubit Arrays in Silicon*. arXiv:2009.02892 [cond-mat, physics:physics, physics:quant-ph]. Sept. 2020. DOI: 10.48550/arXiv.2009.02892.

[45] Harald Jacobsson and G. Holmén. "The dependence of Si and SiO2 electron emission on the angle of ion incidence". In: *Journal of Applied Physics* 74.10 (Nov. 1993), pp. 6397–6400. DOI: 10.1063/1.355165.

[46] K. Stockbridge et al. "Using non-homogeneous point process statistics to find multi-species event clusters in an implanted semiconductor". en. In: *Journal of Physics Communications* 4.1 (Jan. 2020). Publisher: IOP Publishing, p. 015010. DOI: 10.1088/2399-6528/ab6049.

[47] M. Steger et al. "Optically-detected NMR of optically-hyperpolarized 31P neutral donors in 28Si". In: *Journal of Applied Physics* 109.10 (May 2011), p. 102411. DOI: 10.1063/1.3577614.

[48] L.-A. Wu and D. A. Lidar. "Dressed Qubits". In: *Physical Review Letters* 91.9 (Aug. 2003). Publisher: American Physical Society, p. 097904. DOI: 10.1103/PhysRevLett.91.097904.

[49] Gatis Mikelsons et al. "Universal set of gates for microwave dressed-state quantum computing". en. In: *New Journal of Physics* 17.5 (May 2015). Publisher: IOP Publishing, p. 053032. DOI: 10.1088/1367-2630/17/5/053032.

[50] Reetu Inkilä. *Spin-mekaniikka-kytkennän numeerinen mallintaminen käyttäen Python QuTiP -pakettia*. fi. 2023.

[51] J. Majer et al. “Coupling superconducting qubits via a cavity bus”. en. In: *Nature* 449.7161 (Sept. 2007). Number: 7161 Publisher: Nature Publishing Group, pp. 443–447. DOI: 10.1038/nature06184.

[52] D. K. Wilson and G. Feher. “Electron Spin Resonance Experiments on Donors in Silicon. III. Investigation of Excited States by the Application of Uniaxial Stress and Their Importance in Relaxation Processes”. en. In: *Physical Review* 124.4 (Nov. 1961), pp. 1068–1083. DOI: 10.1103/PhysRev.124.1068.

[53] J. Mansir et al. “Linear Hyperfine Tuning of Donor Spins in Silicon Using Hydrostatic Strain”. In: *Physical Review Letters* 120.16 (Apr. 2018). Publisher: American Physical Society, p. 167701. DOI: 10.1103/PhysRevLett.120.167701.

[54] Simeoni Ahopelto. “Optomechanical Simulations for Optimizing Spin-Phono-Photon Coupling in a Silicon Nanobeam”. MA thesis. University of Jyväskylä, Apr. 2024.

[55] Serge Haroche and Jean-Michel Raimond. *Exploring the quantum: atoms, cavities, and photons*. eng. Oxford graduate texts. Oxford: Oxford University Press, 2006.

[56] Alexei M. Tyryshkin et al. “Electron spin coherence exceeding seconds in high-purity silicon”. en. In: *Nature Materials* 11.2 (Feb. 2012). Number: 2 Publisher: Nature Publishing Group, pp. 143–147. DOI: 10.1038/nmat3182.

[57] R. A. Butera and D. H. Waldeck. “An EPR Experiment for the Undergraduate Physical Chemistry Laboratory”. In: *Journal of Chemical Education* 77.11 (Nov. 2000). Publisher: American Chemical Society, p. 1489. DOI: 10.1021/ed077p1489.

[58] Stefan Weber. “Transient EPR”. en. In: *eMagRes*. John Wiley & Sons, Ltd, 2017, pp. 255–270. DOI: 10.1002/9780470034590.emrstm1509.

[59] Hyma H. Vallabhapurapu et al. “Fast Coherent Control of a Nitrogen-Vacancy-Center Spin Ensemble Using a K Ta O 3 Dielectric Resonator at Cryogenic Temperatures”. en. In: *Physical Review Applied* 16.4 (Oct. 2021), p. 044051. DOI: 10.1103/PhysRevApplied.16.044051.

[60] Rick Leijssen and Ewold Verhagen. “Strong optomechanical interactions in a sliced photonic crystal nanobeam”. en. In: *Scientific Reports* 5.1 (Nov. 2015), p. 15974. DOI: 10.1038/srep15974.

[61] Rick Leijssen et al. “Nonlinear cavity optomechanics with nanomechanical thermal fluctuations”. en. In: *Nature Communications* 8.1 (July 2017), ncomms16024. DOI: 10.1038/ncomms16024.

[62] Juha T. Muhonen et al. “State Preparation and Tomography of a Nanomechanical Resonator with Fast Light Pulses”. en. In: *Physical Review Letters* 123.11 (Sept. 2019), p. 113601. DOI: 10.1103/PhysRevLett.123.113601.

[63] Haotian Yang et al. “Characterization of Residual Stress in SOI Wafers by Using MEMS Cantilever Beams”. en. In: *Micromachines* 14.8 (Aug. 2023). Number: 8 Publisher: Multidisciplinary Digital Publishing Institute, p. 1510. DOI: 10.3390/mi14081510.

[64] Tsutomu Iida et al. “Residual lattice strain in thin silicon-on-insulator bonded wafers: Thermal behavior and formation mechanisms”. In: *Journal of Applied Physics* 87.2 (Jan. 2000), pp. 675–681. DOI: 10.1063/1.371925.

[65] M. J. Bereyhi et al. “Hierarchical tensile structures with ultralow mechanical dissipation”. en. In: *Nature Communications* 13.1 (Dec. 2022), p. 3097. DOI: 10.1038/s41467-022-30586-z.

[66] Qimin Quan, Parag B. Deotare, and Marko Loncar. “Photonic crystal nanobeam cavity strongly coupled to the feeding waveguide”. In: *Applied Physics Letters* 96.20 (May 2010), p. 203102. DOI: 10.1063/1.3429125.

[67] Zhu Diao et al. “Stiction-free fabrication of lithographic nanostructures on resist-supported nanomechanical resonators”. In: *Journal of Vacuum Science & Technology B* 31.5 (Sept. 2013). Publisher: American Vacuum Society, p. 051805. DOI: 10.1116/1.4821194.

[68] Ijaz H. Jafri, Heinz Busta, and Steven T. Walsh. “Critical point drying and cleaning for MEMS technology”. In: ed. by Russell A. Lawton et al. Santa Clara, CA, Aug. 1999, pp. 51–58. DOI: 10.1117/12.359371.

ORIGINAL PAPERS

PI

THE EFFECTS OF ION IMPLANTATION DAMAGE TO PHOTONIC CRYSTAL OPTOMECHANICAL RESONATORS IN SILICON

by

Cliona Shakespeare, Teemu Loippo, Henri Lyyra and Juha T Muhonen

Materials for Quantum Technology **1**, 045003 2021.

IOP Publishing Mater. Quantum Technol. 1 (2021) 045003 https://doi.org/10.1088/2633-4356/ac3e42

Materials for Quantum Technology

CrossMark

OPEN ACCESS

RECEIVED
12 October 2021

REVISED
22 November 2021

ACCEPTED FOR PUBLICATION
29 November 2021

PUBLISHED
17 December 2021

PAPER

The effects of ion implantation damage to photonic crystal optomechanical resonators in silicon

Cliona Shakespeare, **Teemu Loippo**, **Henri Lyyra** and **Juha T Muhonen***
Department of Physics and Nanoscience Center, University of Jyväskylä, PO Box 35, FI-40014 University of Jyväskylä, Finland
* Author to whom any correspondence should be addressed.

E-mail: juha.t.muhonen@jyu.fi

Keywords: photonic crystal, ion implantation, optomechanics, silicon, nanomechanical resonator

Supplementary material for this article is available online

Abstract

Optomechanical resonators were fabricated on a silicon-on-insulator substrate that had been implanted with phosphorus donors. The resonators' mechanical and optical properties were then measured (at 6 K and room temperature) before and after the substrate was annealed. All measured resonators survived the annealing and their mechanical linewidths decreased while their optical and mechanical frequencies increased. This is consistent with crystal lattice damage from the ion implantation causing the optical and mechanical properties to degrade and then subsequently being repaired by the annealing. We explain these effects qualitatively with changes in the silicon crystal lattice structure. We also report on some unexplained features in the pre-anneal samples. In addition, we report partial fabrication of optomechanical resonators with neon ion milling.

1. Introduction

Ion implantation is a widely-used technology for doping of semiconductors with applications varying from microchips [1, 2], to solar panels [3], to quantum computing [4]. As ion implantation is a somewhat destructive method, basically bombarding the substrate with high-energy ions, the process inevitably damages the crystal structure of the substrate. This problem is especially acute with silicon, as it is easily damaged and can become amorphous [5].

The implantation damage is usually healed with a post-implantation anneal [6] that both allows the crystal to repair itself and activates any substitutional donor atoms as they can then take their place in the crystal structure. Here we study the effects of the implantation damage and subsequent annealing to the mechanical and optical properties of suspended photonic crystal nanobeams.

The degradation of the mechanical properties of the suspended silicon structures we observe will be of importance to any studies combining implanted ions and mechanical systems (such as hybrid structures combining donor spin qubits [7, 8] with phonon buses [9]). The changes in the optical properties might be of importance to any devices combining ion implantation and photonic crystals in silicon, a field that is expected to grow in importance as single-photon emitters in silicon are being actively investigated [10–13].

2. Structures

The resonators we study, as shown in figure 1, are sliced photonic crystal nanobeams, the general design of which was presented in reference [14] and similar structures were also used in later studies [15, 16]. Details of the exact design studied here are shown in the supplementary material [17]. The photonic crystal pattern in the centre of the nanobeam supports different optical modes than the photonic crystals on the sides, which work as Bragg reflectors for the targeted cavity mode. Note that here we do not have a tapering region between the mirrors and the cavity, although it has been shown to decrease the optical linewidth considerably [15]. The cavity optical mode has an electric field maximum at the centre of the silicon beam. The small vacuum gap

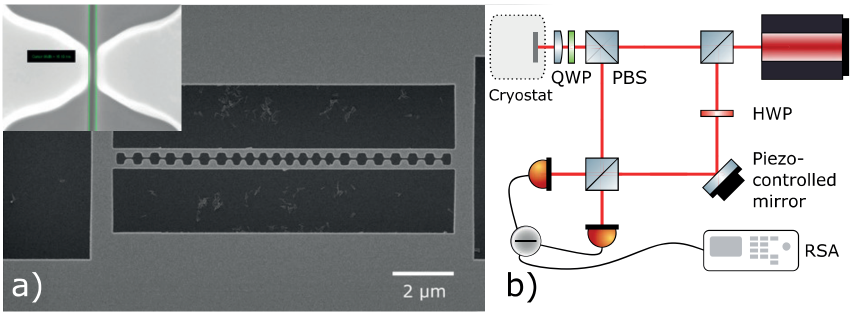

Figure 1. (a) HIM image of a nanobeam with same design as the ones studied here (from the same chip). Grey parts are free hanging silicon and the dark parts show the substrate 3 μm below. The optical cavity is located at the centre of the silicon nanobeam where the photonic crystal lattice constant is smaller. The two beam halves have been separated by a small gap. Inset: a SEM image of the gap between nanobeam teeth showing the roughly 20 nm separation before suspension that was defined with neon ion milling. (b) Schematic of the interferometer used for measurements; QWP refers to a quarter-wave-plate, HWP to a half-wave-plate, PBS to a polarizing beam splitter and RSA to a realtime spectrum analyzer.

between the two beam halves leads to strong field confinement in the gap, and a large frequency dependence of the optical mode on the gap size. This gives strong optomechanical coupling for the mechanical mode where the two beam halves move asymmetrically in-plane (breathing mode).

The samples were fabricated on a silicon-on-insulator wafer with 220 nm device layer and 3 μm buried oxide. The device layer was implanted with phosphorus ions. The ion implantation [18] aimed for a constant donor density of 10^{17} ions cm^{-3} in the device layer and was done in three steps: 110 keV energy with a dose of 1.5×10^{12} ions cm^{-2}, 40 keV with 5×10^{11} ions cm^{-2} and 20 keV with 1.5×10^{11} ions cm^{-2}. The wafer was not annealed after implantation, leaving any potential lattice damage intact.

The wafer was then diced and optomechanical resonators were fabricated on chips. The chips were spin coated first with Microchem 950 k PMMA A4 resist, which was then baked for 3 min on a hotplate at 160°C, then with Allresist AR-PC 5090.02 (Electra 92), which was baked for 1 min at 80°C on a hotplate. The resist was patterned with a Raith eLine electron beam lithography tool. The PMMA was developed for 20 s in a 2:1 mixture of IPA and MIBK. Before development, the Electra 92 resist was washed off. The etching was done with an Oxford Plasmalab 80 reactive ion etcher with 80 sccm SF_6 and 20 sccm O_2 at 30 mTorr at −100°C using liquid nitrogen cooling.

The gap between the beam halves was afterward milled through with 28 keV neon ions in a Zeiss Orion NanoFab helium ion microscope (HIM). Simulations of the neon milling with SRIM [19] (28 keV ion energy, 3–4 pA ion current, 7.5 nC µm^{-2} area dose) show a lateral ion path of up to 30 nm, so there should be only a moderate amount of neon ions in the silicon nanobeams from the milling. Finally the optomechanical structures were released by wet etching the oxide layer with 48% HF for 4 min. An example of a released structure is shown in figure 1(a).

A picture of the milled gap between the beam halves is shown in the inset of figure 1(a) where the high resolution enabled by neon milling is demonstrated as the gap is only 20 nm wide. This would be beneficial for optomechanical applications as the optomechanical coupling strength in these devices grows with decreasing gap size. However, scanning electron micrograph (SEM) images taken after the HF release show an opening of roughly 50 nm. This could be due to the beam halves bending outwards from stress or charging but requires further study.

3. Measurements

The samples were placed inside a Montana instruments C2 s50 cryostat and measured with a balanced homodyne interferometer (schematic in figure 1(b)) using near infrared wavelengths. The optical cavity was coupled into from above with a free space laser beam and the reflected light was interfered with a reference laser beam. The interference signal as a function of laser wavelength was measured with a subtracting detector and a spectrum analyzer. Lorentzian line shapes were fitted to the brightest mechanical peak visible in each spectrum (using the Python package SciPy [20]) and the optical and mechanical resonance frequencies and linewidths were extracted from these fits. As we do not lock the phase of the interferometer but average over all the phases by sweeping a piezo mirror in the local oscillator arm, our mechanical peaks split with the frequency of the a sweep (c. 100 Hz). The effective optical linewidth is also modified. We account for both of these effects in our fitting procedures.

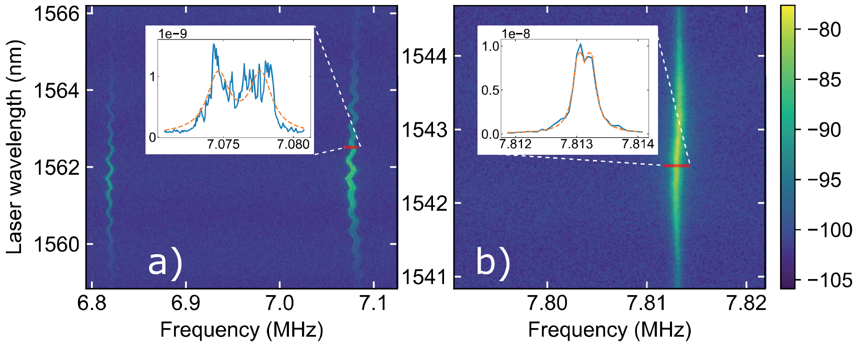

Figure 2. Resonator 2 spectrogram measured at 6 K before (a) and after (b) annealing as a function of the laser wavelength. The colorbar shows the power of the interferometer signal in dB. Crosscuts of the spectra (on a linear scale) are shown in the insets with Lorentzian fits (dashed line). The post-anneal sample exhibits much clearer Lorentzian resonance. The pre-anneal sample has two unexpected features: the oscillation of the resonance frequency and the splitting of the mode into two separate peaks separated by few kHz. Note that the small splitting in the post-anneal sample (by 100 Hz) is caused by the phase averaging in the measurement (see text). In the pre-anneal sample there is another mechanical mode visible at around 6.8 MHz which also shows the oscillations.

After measuring the resonators at both room temperature and 6 K, the samples were taken out and annealed in a tube furnace for 30 min at 600°C and 15 s at 1000°C, after which they were put to 500°C for 5 min before taken out of the oven. The last step was included for a gentler cool down process. All annealing was done in an argon atmosphere with 1 atm pressure. The chip was left to cool overnight, after which the chip was loaded into the cryostat and the measurements at room temperature and 6 K repeated.

4. Results and discussion

All data presented has been measured from two different resonators on the same chip, which we name resonator 1 and resonator 2. They are nominally identical in design, except that resonator 2 has been scaled in two dimensions by a factor of 1.04 compared to resonator 1. (The thickness is defined by the substrate and cannot be scaled.) We note that the differences we observe between the two samples stem mainly from fabrication imperfections [17] as we elaborate below.

The wavelength dependent spectrogram of the interferometer signal from resonator 2 is shown in figure 2. Similar data from resonator 1 is shown in the supplementary material [17]. The thermally driven mechanical vibrations are visible in the interferometer signal when the laser wavelength is close to the optical cavity resonance frequency. An unexpected phenomenon was the oscillation of the mechanical resonance frequency as a function of the laser wavelength in the pre-anneal samples at 6 K, as shown in figure 2(a). This effect was present in both resonators though much more noticeable in resonator 2 and disappeared after annealing. The oscillation was consistent between consecutive measurements (meaning the same wavelength would produce same response) but varied when the laser spot position (with regards to the silicon nanobeam) was moved. Changing the laser power by a factor of 5 had no significant effect on the phenomenon, implying it is not a thermal effect. Also, the mechanical resonances in the pre-anneal samples seemed to occasionally split to two modes separated by a few kHz but this varied with both laser wavelength and time. This splitting was visible only at 6 K temperatures. When extracting the parameters below, we fit this data assuming two modes.

After annealing the mechanical resonance frequencies increased consistently by ∼10% for both samples at both temperatures, as pictured in figure 3, with pre-anneal frequencies lying in the range of 7–8 MHz. An increase in resonance frequency implies a stiffer resonator, i.e., a higher Young's modulus. The Young's modulus for silicon depends on crystal orientation [21] and is higher for crystalline silicon in the fabrication direction of our device (166 GPa for crystal direction [110]) than for polycrystalline silicon (155 GPa). This means that the shift in resonance frequency can at least qualitatively be explained by the lattice structure being damaged by the ion implantation—making it in effect more polycrystalline-like—and then being reconstructed by the annealing.

To study the effect further, we made COMSOL simulations of the beams' mechanical resonance frequencies using both polycrystalline silicon and single-crystalline silicon with the same crystal direction as our sample. The details of the COMSOL simulation are presented in the supplementary material [17]. The simulated resonance frequencies for resonator 1 were 6.6 MHz for polycrystalline silicon and 6.8 MHz for single-crystalline silicon. For resonator 2 the values were 6.4 MHz and 6.6 MHz, respectively. This is in qualitative agreement with the measurements but the measured shifts are consistently higher than this effect alone would predict.

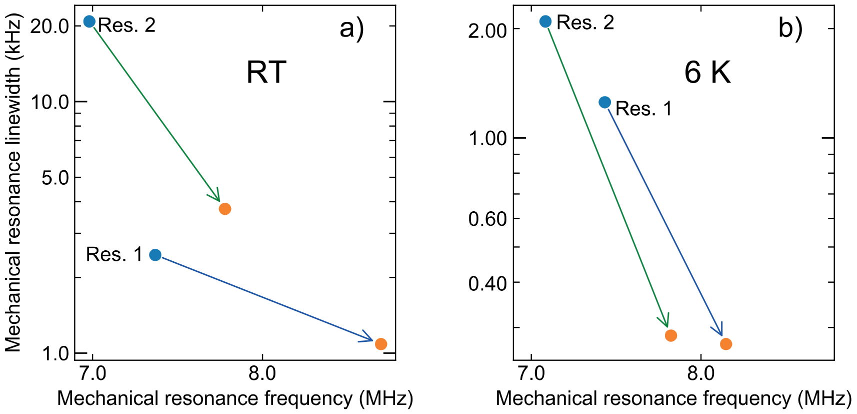

Figure 3. Plots of the resonators' mechanical resonance frequencies and linewidths before (blue) and after (orange) the annealing at room temperature (a) and 6 K (b). The values before and after annealing have been connected with blue (resonator 1) and green (resonator 2) arrows for clarity.

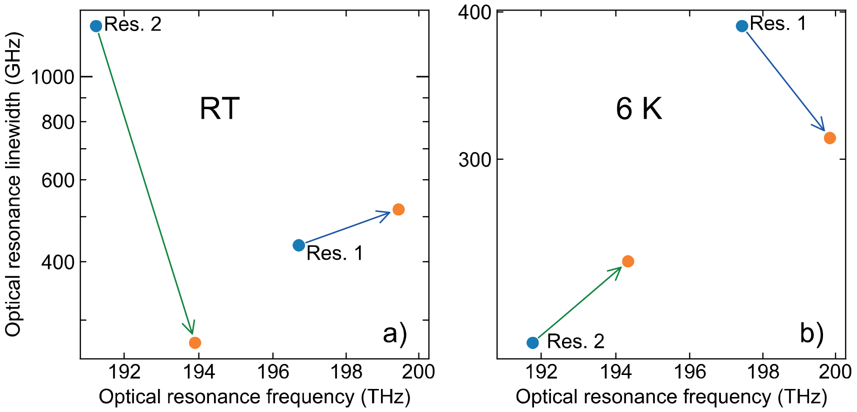

Figure 4. Plots of the resonators' optical resonance frequencies and linewidths before (blue) and after (orange) the annealing at room temperature (a) and 6 K (b). The values before and after annealing have been connected with blue (resonator 1) and green (resonator 2) arrows for clarity.

The mechanical linewidths for both resonators decreased after the anneal. Interestingly all measured modes (including unshown less bright modes) ended up with a linewidth of 0.2–0.3 kHz at cryogenic temperatures after the anneal, possibly indicating a limit where some mechanism not related to temperature or crystal damage is determining the linewidth (such as clamping losses). In room temperature measurements resonator 1's linewidth improved by a factor of 2 whereas resonator 2 had an improvement by factor of 6. The trend is consistent with the lattice structure healing from implantation damage during the annealing, as lattice defects can cause mechanical damping [22].

We note that the changes in the mechanical frequencies and linewidths between room temperature and 6 K are a known feature with these kinds of structures and are presumably related to the stress/strain of the samples changing during the cooldown (due to the mismatch in thermal expansion between the silicon device layer and the underlying silicon dioxide).

The changes in the optical properties during annealing are presented in figure 4. The optical cavity resonance frequency and cavity linewidth can be extracted from the strength of the optomechanical signal as a function of the laser wavelength. The optical resonance frequencies increased by $\sim$1% during the anneal. Here there are two effects that might be playing a role: (i) a decrease in the effective refractive index or (ii) change in the equilibrium gap size between the beams due to mechanical reasons. We unfortunately cannot completely untangle these effects. The refractive index of polycrystalline silicon is higher than that of single-crystal silicon [23]. Thus recrystallization of the silicon lattice could lead to a lowering of refractive index and a resonance shift toward higher optical frequencies in accordance with our results. We also imaged the sample with SEM before and after annealing and saw no visible change in the gap size. Note that the doping concentration should not affect the effective refractive index at these wavelengths and doping levels [24].

For the optical linewidth we did not recover any consistent trend. We note that there could be two competing factors here. Silicon crystal lattice damage can be expected to cause photon losses to increase, and polycrystalline silicon also has a higher coefficient of absorption at these wavelengths [25], which means that annealing should decrease the linewidth. On the other hand, doping activation during annealing would be expected to cause photon losses to increase.

We presume that the fact that there is a considerable difference between the two resonators in their optical properties (before and after annealing) is due to fabrication imperfections. The fabrication procedure for the samples here is somewhat non-conventional as we did not use an ICP-RIE (but a regular RIE) and we milled the gap between the two beams with neon milling. The relatively large differences in the optical quality are most likely explained by the neon milling which required drawing the milling line ‘by hand’ when looking at the neon ion image, so the alignment accuracy is poor. There are also some charging effects in play that cause variations in the milling. Overall, this is still a very experimental way to fabricate these devices and leads to large variability in the parameters.

5. Conclusions

In conclusion, we have shown that post-implantation annealing has a significant effect on the optical and especially the mechanical properties of silicon photonic crystal nanobeams. The exact mechanisms of the effects we demonstrated still require further study but can qualitatively be explained by implantation damage making the silicon more polycrystalline-like and annealing then recovering the single-crystalline structure. These findings will have relevance to any nanophotonic device that combines ion implantation with photonic crystal structures, particularly the emerging field of spin-photonics in silicon as well as to any structures combining ion implantation and mechanical devices in silicon. The pre-anneal samples exhibited several unexplained features that could bear further investigation.

Acknowledgments

We acknowledge Luke Antwis and Roger Webb for help with the ion beam implantations. This project has received funding from the European Research Council (ERC) under the European Union’s Horizon 2020 research and innovation programme (Grant Agreement No. 852428), from Academy of Finland Grant No. 321416 and Jenny and Antti Wihuri Foundation.

Data availability

The data that support the findings of this study are available upon reasonable request from the authors.

ORCID iDs

Cliona Shakespeare https://orcid.org/0000-0002-3654-2229
Teemu Loippo https://orcid.org/0000-0001-7545-0936
Henri Lyyra https://orcid.org/0000-0002-9218-4657
Juha T Muhonen https://orcid.org/0000-0001-6520-6999

References

[1] Poate J M and Saadatmand K 2002 *Rev. Sci. Instrum.* **73** 868–72
[2] Rubin L and Poate J 2003 *Ind. Phys.* **9** 12 https://web.archive.org/web/20071011192314/http://aip.org/tip/INPHFA/vol-9/iss-3/p12.html
[3] Rohatgi A, Meier D L, McPherson B, Ok Y-W, Upadhyaya A D, Lai J-H and Zimbardi F 2012 *Energy Procedia* **15** 10–9
[4] van Donkelaar J *et al* 2015 *J. Phys.: Condens. Matter.* **27** 154204
[5] Williams J S 1998 *Mater. Sci. Eng.* A **253** 8–15
[6] Ziegler J F 1985 *Nucl. Instrum. Methods Phys. Res.* B **6** 270–82
[7] Pla J J, Tan K Y, Dehollain J P, Lim W H, Morton J J L, Jamieson D N, Dzurak A S and Morello A 2012 *Nature* **489** 541–5
[8] Muhonen J T *et al* 2014 *Nat. Nanotechnol.* **9** 986–91
[9] Patel R N, Wang Z, Jiang W, Sarabalis C J, Hill J T and Safavi-Naeini A H 2018 *Phys. Rev. Lett.* **121** 040501
[10] Chen S, Raha M, Phenicie C M, Ourari S and Thompson J D 2020 *Science* **370** 592–5
[11] Bergeron L *et al* 2020 *PRX Quantum* **1** 020301
[12] Weiss L, Gritsch A, Merkel B and Reiserer A 2021 *Optica* **8** 40–1
[13] Durand A *et al* 2021 *Phys. Rev. Lett.* **126** 083602

[14] Leijssen R and Verhagen E 2015 *Sci. Rep.* **5** 15974
[15] Leijssen R, La Gala G R, Freisem L, Muhonen J T and Verhagen E 2017 *Nat. Commun.* **8** ncomms16024
[16] Muhonen J T, La Gala G R, Leijssen R and Verhagen E 2019 *Phys. Rev. Lett.* **123** 113601
[17] See supplemental material at (https://stacks.iop.org/MQT/1/045003/mmedia)
[18] Implantation was carried out in the ion beam centre of University of Surrey.
[19] Ziegler J F, Ziegler M D and Biersack J P 2010 *Nucl. Instrum. Methods Phys. Res.* B **268** 1818–23
[20] Virtanen P *et al* (SciPy 1.0 Contributors) 2020 *Nat. Methods* **17** 261–72
[21] Hopcroft M A, Nix W D and Kenny T W 2010 *J. Microelectromech. Syst.* **19** 229–38
[22] Shin J, Choi K, Shiko S, Choi H and Bae D 2015 *Composites* B **77** 194–8
[23] Jones R E and Wesolowski S P 1984 *J. Appl. Phys.* **56** 1701–6
[24] Auslender M and Hava S 2017 *Single-Crystal Silicon: Electrical and Optical Properties* (Berlin: Springer)
[25] Harbeke G, Krausbauer L, Steigmeier E F, Widmer A E, Kappert H F and Neugebauer G 1984 *J. Electrochem. Soc.* **131** 675–82

PII

THERMAL RELAXATION TIME AND PHOTOTHERMAL OPTOMECHANICAL FORCE IN SLICED PHOTONIC CRYSTAL SILICON NANOBEAMS

by

Cliona Shakespeare, Arvind S. Kumar and Juha T Muhonen

Manuscript (2024).

Thermal relaxation time and photothermal optomechanical force in sliced photonic crystal silicon nanobeams

CLIONA SHAKESPEARE,[1] ARVIND S. KUMAR,[1] AND JUHA T. MUHONEN [1,*]

[1] *Department of Physics and Nanoscience Center, University of Jyväskylä, P.O. Box 35, FI-40014 University of Jyväskylä, Finland*
[*] *juha.t.muhonen@jyu.fi*

Abstract: Optomechanical devices based on sliced silicon photonic crystal nanobeams could have several use cases in future quantum technologies, especially as quantum transducers between different quantum systems. To create the required pure mechanical states at low temperatures, understanding of photon absorption, thermal relaxation, and the associated photothermal force is crucial. Here, we characterize the strength of the photothermal force in a sliced silicon nanobeam resonators. Novelly, we extract the thermal relaxation time separately from phonon ray tracing simulations, allowing us to study the strength of the photothermal optomechanical effect without the uncertainty from the thermal relaxation time. With this information we can put strict upper bounds to the photothermal force and photon absorption (β parameter) in the devices, without knowledge of the cavity photon population. The methods we employ can easily be adapted to other geometries and devices for the study of the photothermal effects.

1. Introduction

Cavity optomechanics [1] is a mature field studying the interaction between mechanical motion and optical cavity fields. Major milestones of the field include ground state cooling [2–4] and entanglement generation [5,6]. In the near future, the field is expected to contribute significantly especially to precision metrology [7] and to quantum transduction between different quantum states [8,9], such as between microwave and optical photons [10] or between defect qubits and optical light [11].

While the optomechanical interaction is typically described through the radiation pressure force, there are also other forces at play. The photothermal (or bolometric) force, caused by absorbed photons inducing temperature gradients and thus thermal strain in the structure, can cause optomechanical effects similar to those caused by the radiation pressure force [12, 13]. The photothermal effect is usually modeled as a time-lagged force proportional to the number of photons in the cavity, similarly to the radiation pressure force from a detuned laser. All the phenomena caused by the radiation pressure induced "dynamical backaction" are thus also present in photothermal dominant optomechanics. Perhaps the most striking example of this is the fact that this "heating" can be used to cool down the mode of interest [12, 14, 15]. The crucial difference is that the lag is offset compared to the usual radiation pressure detuning dependence, and hence can work to either increase or suppress the radiation pressure effects.

In most cases the photothermal force can be hard to control and thus introduces an element to the system that is not necessarily consistent across devices. Hence even though it can in some cases be used to one's advantage [16, 17], it is generally an unwanted effect when moving towards applications. One increasing application area for optomechanical systems is as a transducing element between different quantum systems, such as microwave and optical photons, or spins in solid state and optical photons. These applications will increasingly depend on both low bath temperatures and relatively high optical powers to achieve high quantum cooperativities, placing stringent requirements to the tolerated heating effects. This gives topicality to the study of the thermal effects in optomechanical devices which show promise for the quantum transduction purposes.

Most of the milestones of optomechanics mentioned above have been achieved with systems operating at the resolved sideband regime, where the mechanical resonance frequency ω_0 is greater than the optical cavity linewidth κ, and the energy exchange between the two subsystems can be modeled as Stokes and anti-Stokes scattering events. The opposite regime where $\omega_0 \ll \kappa$, on the other hand, allows for instantaneous measurements of the mechanical motion, enabling taking advantage of differing phenomena such as measurement based feedback control [18, 19] and pulsed measurements [20–22], for controlling and creating non-classical mechanical states. A promising geometry working in this 'bad cavity' regime are the sliced silicon nanobeam resonators [23] which have been demonstrated to have exceptionally large optomechanical coupling rates and single-photon cooperativities [24], but so far no literature exists on their photothermal characteristics. Here, we study the photon absorption and the induced photothermal effect in these structures at cryogenic temperatures.

Specifically, we model and experimentally measure the photothermal force from photon absorption in a sliced silicon photonic crystal device, shown in Fig. 1a. Several treatments of the photothermal force exist in the literature, and analysis of the effects has been done through both the equations of motion [25] and thermal modal analysis [26]. Generally the effects are hard to model from first principles, and the photothermal force is instead modeled via two phenomenological parameters. The first one is the the magnitude of photon absorption (and its transduction into excitations of the mechanical mode of interest), characterized with the so-called β-parameter, which can be both positive or negative [27, 28], depending on whether the thermal force increases or suppresses the radiation pressure force. In addition, the photothermal phenomena depend strongly on the thermal relaxation time of the structures τ. Both of these parameters, but especially the latter, vary according to the exact geometry of the device [29–31], and analytical solutions for calculation of the thermal decay only exist for simple geometries. Here, we solve this problem by using phonon ray tracing simulations to simulate the expected thermal decay time of the structures.

Using the simulated thermal relaxation time and simple formulae derived for the photothermal effect at the bad cavity limit we can put strict upper bounds on β by simply looking at the ratio of changes in the mechanical damping and the mechanical frequency as a function of laser detuning. Notably, our method does not need any calibration of the input optical power, making it a straightforward method for characterization of the photothermal effect.

2. Photothermal force at the linear response regime

A detailed treatment of the optomechanical effects caused by photothermal forces has been done in previous literature, and we will not repeat that extensively here. We refer the reader especially to Refs. [25, 28]. For the analysis below, we need to only consider the classical limit of the optomechanical equations of motion with both the radiation pressure and the photothermal force

$$m\ddot{x}(t) + m\gamma\dot{x}(t) + m\omega_0^2 x(t) = F_0(t) + \hbar G|\alpha(t)|^2 + F_{pt}(\alpha(t)) \tag{1}$$

$$\dot{\alpha}(t) = -\frac{\kappa}{2}\alpha(t) + i(\Delta + Gx(t))\alpha(t) + \sqrt{\kappa_{ex}}\alpha_{in}(t). \tag{2}$$

Here, α is the amplitude of the cavity field, x is the displacement of the mechanical oscillator, γ is the mechanical damping rate, m is the mechanical resonator mass, F_0 is the stochastic thermal driving force, G is the optomechanical coupling rate, Δ is the detuning between the optical cavity resonance frequency and the laser frequency, and $\sqrt{\kappa_{ex}}\alpha_{in}(t)$ is the input laser field. For the photothermal force, we follow previous literature, setting

$$F_{pt}(\alpha(t)) = \frac{\hbar G\beta}{\tau}\int_{-\infty}^{t} e^{-\frac{t-t'}{\tau}}|\alpha(t')|^2 dt'. \tag{3}$$

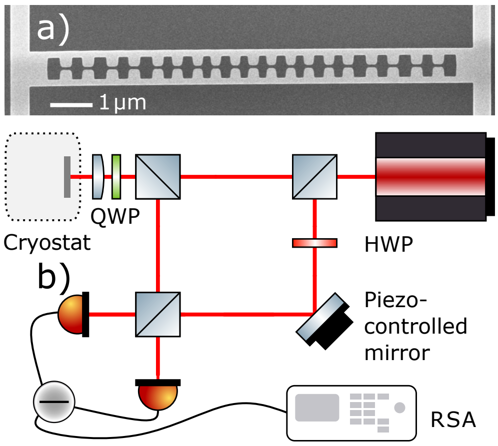

Fig. 1. a) A scanning electron microscope (SEM) image of a nanobeam similar to the device measured in this paper. The light gray areas are suspended silicon and the dark gray is the substrate 3 μm below. The holes in the silicon nanobeam form a photonic cavity in the middle of the beam, while the mechanical mode is the asymmetric ("breathing") mode of the two beam halves moving in-plance. More details in the text, and previous work on similar devices is presented in Refs. [22, 24]. b) A schematic of the interferometer used to measure the device. QWP refers to a quarter wave plate, HWP to a half wave plate, and RSA to a realtime spectrum analyzer.

This equation describes a force with a time delay controlled by the thermal relaxation rate τ and strength β. Note that if $\alpha(t)$ would be a constant in time, $F_{pt} = \beta F_{rad}$, where $F_{rad} = \hbar G|\alpha|^2$.

One can solve these equations in frequency space after a Fourier transform. However, this cannot be done directly due to the nonlinear terms $x(t)\alpha(t)$ and $|\alpha(t)|^2$. As usual, we linearize these equations by writing $\alpha = \bar{\alpha} + \delta\alpha$ describing the average value of the optical cavity amplitude and its fluctuations, respectively, and neglect all terms proportional to fluctuations squared. Inputting these and Fourier transforming we recover optomechanical equations with the photothermal component

$$x(\omega) = \frac{F_0 + \left[\hbar G\left(1 + \frac{\beta}{1-i\omega\tau}\right)\right]\left(\bar{\alpha}^\star \delta a(\omega) + \bar{\alpha}\delta a^\star(\omega)\right)}{m(\omega_0^2 - \omega^2 + i\gamma\omega)} \tag{4}$$

$$\delta a(\omega) = \frac{iG\bar{\alpha}x(\omega)}{\frac{\kappa}{2} + i(\omega - \Delta)}, \tag{5}$$

where $\bar{\alpha} = \frac{\sqrt{\kappa_{ex}}\alpha_{in}}{\kappa/2 - i\Delta}$, and below we define $\chi_m = [m(\omega_0^2 - \omega^2 + i\gamma\omega)]^{-1}$.

Substituting Eq. (5) to Eq. (4), and using $\delta a^\star(\omega) = [\delta a(-\omega)]^\star$ and the fact that x is a hermitian, the equation for x reads [1, 28]

$$x(\omega) = \chi_m F_0 + \chi_m\left(1 + \frac{\beta}{1 - i\omega\tau}\right)\Sigma(\omega)x(\omega) \tag{6}$$

$$\Sigma(\omega) = \hbar G^2|\bar{\alpha}|^2\left(\frac{1}{(\omega - \Delta) - i\kappa/2} - \frac{1}{(\omega + \Delta) - i\kappa/2}\right). \tag{7}$$

Solving for $x(\omega)$ this result can then be conviently expressed as an effective susceptibility

$$x(\omega) = \frac{F_0}{\chi_m^{-1} - \left(1 + \frac{\beta}{1-i\omega\tau}\right)\Sigma(\omega)} \equiv \chi_{\text{eff}}F_0. \tag{8}$$

Below, we fit the change of the mechanical resonance frequency as a function of the laser detuning, i.e., optical spring. For this we define that $\chi_{\mathrm{eff}} \equiv [m(\omega_0^{\prime 2} - \omega^2 + i\gamma^{\prime}\omega)]^{-1}$, where $\omega_0^{\prime} = \omega_0 + \delta\omega_0$ and $\gamma^{\prime} = \gamma + \delta\gamma$. Assuming a high-Q resonator we write

$$\begin{aligned}\delta\omega_0 &= \frac{\Re\left[\left(1+\frac{\beta}{1-i\omega_0\tau}\right)\Sigma(\omega_0)\right]}{2m\omega_0} \\ &= g^2\left[\left(1+\frac{\beta}{1+\omega_0^2\tau^2}\right)\left(\frac{\omega_0-\Delta}{\frac{\kappa^2}{4}+(\omega_0-\Delta)^2}+\frac{\omega_0+\Delta}{\frac{\kappa^2}{4}+(\omega_0+\Delta)^2}\right)\right. \\ &\left.-\left(\frac{\beta\omega_0\tau}{1+\omega_0^2\tau^2}\right)\left(\frac{\frac{\kappa}{2}}{\frac{\kappa^2}{4}+(\omega_0-\Delta)^2}-\frac{\frac{\kappa}{2}}{\frac{\kappa^2}{4}+(\omega_0+\Delta)^2}\right)\right], \end{aligned} \tag{9}$$

where we have used the relation $\hbar G^2|\bar{\alpha}|^2 = 2m\omega_0 g^2$, and $g^2 = |\bar{\alpha}|^2 g_0^2$. This formula is used in fits below. Note that we made the approximation that $\delta\omega_0 \ll \omega_0$.

The above formula gets an especially simple form if we assume the bad cavity limit so that basically at all points we can approximate $\Delta \pm \omega \approx \Delta$. Then in Eq. (9) the latter term cancels out and the first term reads

$$\delta\omega_0 \approx g^2\left(1+\frac{\beta}{1+\omega_0^2\tau^2}\right)\left(\frac{-2\Delta}{\frac{\kappa^2}{4}+\Delta^2}\right). \tag{10}$$

This is the usual term for the optical spring at the bad cavity limit [1], but with the addtion of the β-term. We note especially, that as β can be negative, there exists a value $\beta = -1 - \omega_0^2\tau^2$, where the optical spring gets completely cancelled out (for a high-Q mechanical oscillator). This could be an interesting regime for e.g. sensing applications.

The other parameter of interest is the change in the mechanical damping rate due to optomechanical forces $\gamma^{\prime} = \gamma + \delta\gamma$

$$\begin{aligned}\delta\gamma &= \frac{\Im\left[\left(1+\frac{\beta}{1-i\omega_0\tau}\right)\Sigma(\omega_0)\right]}{m\omega_0} \\ &= 2g^2\left[\left(1+\frac{\beta}{1+\omega_0^2\tau^2}\right)\left(\frac{\kappa/2}{\frac{\kappa^2}{4}+(\omega_0-\Delta)^2}-\frac{\kappa/2}{\frac{\kappa^2}{4}+(\omega_0+\Delta)^2}\right)\right. \\ &\left.+\left(\frac{\beta\omega_0\tau}{1+\omega_0^2\tau^2}\right)\left(\frac{\omega_0-\Delta}{\frac{\kappa^2}{4}+(\omega_0-\Delta)^2}-\frac{\omega_0+\Delta}{\frac{\kappa^2}{4}+(\omega_0+\Delta)^2}\right)\right], \end{aligned} \tag{11}$$

which then again in the bad cavity limit simplifies to

$$\delta\gamma \approx 2g^2\left(\frac{\beta\omega_0\tau}{1+\omega_0^2\tau^2}\right)\left(\frac{-2\Delta}{\frac{\kappa^2}{4}+\Delta^2}\right). \tag{12}$$

Hence, if $\beta = 0$, one expects no changes in the mechanical damping rate.

For the analysis below, we will crucially note that as we are deep in the bad cavity limit, we can write down the ratio of the expected changes in the damping rate and the mechanical frequency

$$\frac{\delta\gamma}{\delta\omega_0} = \frac{2\beta\omega_0\tau}{1+\omega_0^2\tau^2+\beta}. \tag{13}$$

As we will extract τ below separately, this ratio allows us to put bounds on β based solely on the magnitude of the two changes we see, without any uncertainty in calibration of g_0 or number of photons in the cavity.

3. The thermal decay rate

From the above equations, it is clear that an important parameter for the photothermal effect is the thermal relaxation rate τ, and especially it's relation to the mechanical resonance frequency $\omega_0\tau$. Here we will model τ quantitatively, allowing us to make more solid conclusions on the magnitude of β based on our data.

The dominant thermal transport channel at low temperatures in silicon is phonon transport, the efficiency of which can be characterized by the mean free path of phonons before any scattering event. At room temperature the mean free path is limited by phonon-phonon scattering and is diffusive but at low temperatures the bulk phonon transport becomes ballistic, and the dominant phonon scattering in nanoscale structures is the scattering from the device boundaries. At this regime, the phonon mean free path Λ is determined by the structure's dimensions [32] and the specularity of the surface scattering, i.e., the roughness of the surfaces. The regime where scattering is fully dominated by surface scattering and is completely non-specular is known as the Casimir ballistic transport (CBT) regime [33, 34]. When the phonon wavelengths start to be comparable to the surface roughness, the specularity of the scattering will increase leading to an increase in the effective free mean path of the phonons. This regime is known as the Ziman regime [34].

Analytical solutions for τ exist for simple geometries at the Casimir and Ziman regime. In the Casimir regime (non-specular scattering), the phonon mean free path for rectangular beams depends on the cross sectional area of the beam A, so that the mean free bath $\Lambda_{\text{cas}} = 1.12\sqrt{A}$ [35]. From this, one can calculate the thermal relaxation time τ for ballistic transport [28]

$$\tau = \frac{3l^2}{\pi^2 c_s \Lambda_{\text{cas}}}, \tag{14}$$

where c_s is the average speed of sound in the material and l the length of the beam. A possible increase in the specularity of the scattering s can the be modelled with the Ziman equation [34]. The increase in specularity will increase the effective mean path as $\Lambda_{\text{zim}} = \frac{1+s}{1-s}\Lambda_{\text{cas}}$, hence decreasing τ.

In more complicated geometries such as our "toothed" beam, an exact analytical calculation is not possible. We can still do estimates based on the formulae above. The devices are 220 nm thick and have a width of 123 nm (gaps) to 318 nm (teeth), with an average width of 227 nm, as shown schematically in Fig. 2a. This would, using the narrower dimension for the width, give us a casimir mean free path of c. 180 nm and a value for τ of 17.9 ns. The average width, on the other hand, would give a mean free path of c. 250 nm and a τ of 13.2 ns. Interestingly, this would mean our $\omega_0\tau$ ratio is below but comparable to one. However, as we show below the more detailed simulated values for τ differ from these predictions by up to a factor of 2, and the effects of specularity do not follow the naive Ziman prediction.

To get a more realistic value for τ we use a ray tracing model to simulate the phonon transport and therefore heat conduction through the structure. Specifically, we use an open source Monte Carlo phonon ray tracing simulator [36] to trace the phonon paths. To get enough statistics, we simulate a total of 400 000 phonon paths. As we are working in cryogenic temperatures (4 K) and with structures where both transverse dimensions are of the order of 10^{-7} m, we can safely assume the scattering will be dominated by the surfaces and we use an effectively infinite bulk mean free path. (Other values are considered in the Supplement.) The surface specularity, which describes the probability of specular reflection at a given surface, can be set individually for each surface in the code. A value of 1 means that the surface behaves in a mirror-like fashion, whereas a value of 0 means that when encountering the surface, a phonon scatters randomly to

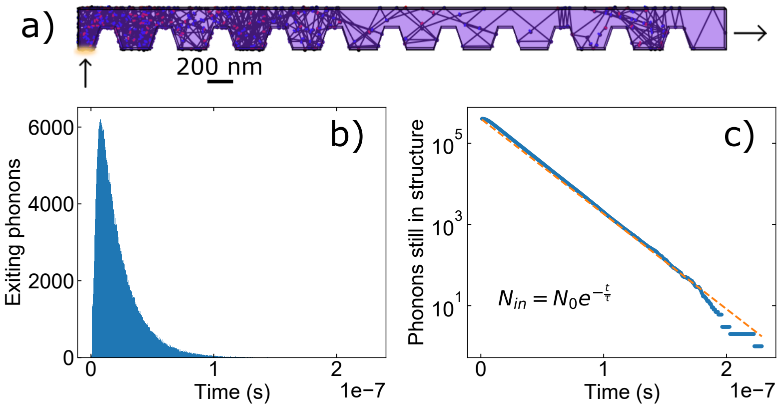

Fig. 2. An example of how we extract the τ value from the Monte Carlo simulations. a) The path of an example phonon, which enters from the inlet, where the optical intensity is at its maximum (bottom left, yellow circle), and exits through the outlet (right) where the part connects to the bulk silicon. As the beam is symmetrical, we only need to simulate one half of it and can do so by setting $s = 1$ for the surface over which the structure is mirrored. We show here a 2D projection from the 3D simulation. The travel time for all of these phonons is then compiled into a histogram (b) from which we calculate the number of phonons still in the structure at a given time (c) and fit this with an exponential decay curve $e^{-t/\tau}$).

any direction (the Casimir regime). We used a single value for all surfaces, calculated as [37]

$$s(\lambda) = \exp\left[-16\pi^2 \left(\frac{R}{\lambda}\right)^2\right], \tag{15}$$

where R is the RMS surface roughness and λ is the wavelength of normally incident scattered phonons. For our samples, we measured a surface roughness of 0.81 nm for the top surface with atomic force microscope. We use this value for all the surfaces. When using Eq. (15), we approximate the phonon wavelength to be the dominant phonon wavelength $\lambda_{dom} = c_s/\nu_{dom}$, where $\nu_{dom} = 4.25 k_B T/h$ [38] is the temperature-dependent dominant phonon frequency. For the lowest temperature of 4 K, this gives $\lambda_{dom} \approx 17$ nm and a specularity of $s \approx 0.7$. For higher temperatures, λ_{dom} decreases, as does specularity. The next-lowest temperature in our dataset is 7 K, for which $s \approx 0.3$. For higher temperatures, scattering off the walls of the structure is wholly non-specular, *i.e.* $s = 0$ for all surfaces.

To model the photon absorption heating of our beams, we assume a local heating point at the maximum of the electrical field of the optical cavity, and that phonons enter at a (uniformly distributed) random angle through a defined surface in the structure. They are then followed in a ray tracing manner, with the behavior at boundary reflections defined by the specularity, until they exit the structure through a surface that connects our device to the bulk of the silicon. The simulation gives the time each phonon spends in the structure. From this, we can calculate how many phonons are still in the structure at any given time after a heating pulse (assumed to happen at $t = 0$). This will be an exponential decay, with the decay constant given by τ. This process is illustrated in Fig. 2. We receive a value of 21.4 ns for τ with a surface specularity of 0.7 (corresponding to a temperature of 4 K), 32.3 ns with 0.3 (7 K), and 38.9 ns for wholly diffusive scattering (15 K, 30 K, and 70 K). All simulation results are plotted in Fig. 3.

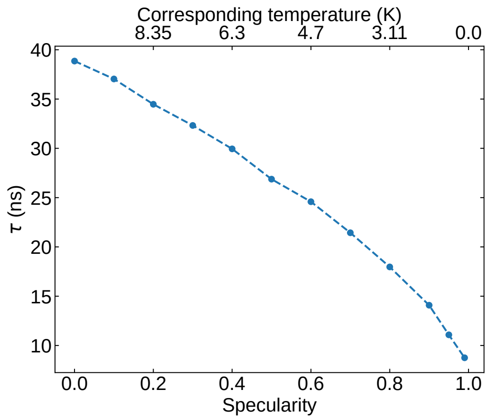

Fig. 3. A plot of the τ values simulated for a range of specularities. The points show the actual simulation results, while the dashed line is a guide for the eye. The top axis shows the corresponding temperature using the surface roughness mentioned in the text. Note that for $s = 0$, the corresponding temperature asymptotically approaches infinity and is thus not labeled.

4. Experimental results

A SEM image of a sliced photonic crystal nanobeam similar to the measured is shown in Fig. 1a. The devices have an optical cavity defined by the 1D photonic crystal structure with resonance frequencies around the telecom band of 1550 nm and typically have mechanical resonance frequencies between 5 and 10 MHz. The mechanical mode is the in-plane vibrational mode of the two beam halves moving with respect to each other. The optical cavity linewidth in these devices is of the order 100 GHz, placing them deep in the non-resolved sideband regime. Optomechanical measurements were done using a homodyne interferometer setup, whose schematic is shown in Fig. 1b, and the mechanical displacement spectrum and cavity linewidth were extracted through quadrature-averaged measurements [39] that were performed by tuning the laser wavelengths across the cavity resonance. At each laser detuning we extract the mechanical spectrum and fit it to a lorentzian lineshape, extracting the mechanical resonance frequency and linewidth. We report data on 2 devices at several different temperatures.

Figure 4 shows the measurement results from one of the resonators at bath temperature of 4 K. In order to extract quantitatively the photothermal effects one needs to be able to separate between them and the radiation pressure induced effects. As the two can be qualitatively similar (as shown in Fig. 4a), this can require a precise determination of the optomechanical parameters in order to model the radiation pressure effects and pinpoint the discrepancies. In our case, however, we see that there is a clear optical spring effect in the resonance frequency of the device (Fig. 4a) , whereas the mechanical damping rate shows no clear detuning dependance (Fig. 4b). As noted above in Eq. (12), this is consistent with having no photothermal force, and allows us to put strict upper limits to the value of β in these structures.

Specifically we take conservative estimates on the maximum value of $\delta\gamma$, as shown with lines in Fig. 4b, and use these together with the extracted values for $\delta\omega$ to calculate a bound for beta based on Eq. (13) without any uncertainty in determining cavity parameters like g_0 or number of photons in cavity. As we have also extracted τ from the ray tracing simulations, we have no free parameters. This value is shown at different temperatures for the two different resonators in Fig. 5b. In Fig. 5a we also plot the extracted beta from Eq. (13) point-by-point as a function of detuning, limiting the data to the points where $\delta\omega > 1$ kHz. This shows that our general limits,

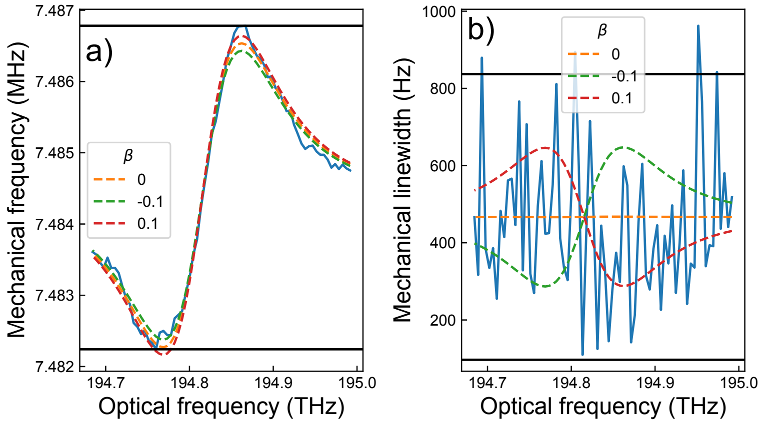

Fig. 4. (a) The mechanical frequency of the resonator extracted from experiment (blue line), plotted as a function of optical frequency of the laser, at bath temperature of 4 K. The dashed lines show fits to optical spring with different β values, demonstrating how beta can be hard to extract from the optical spring data alone. (b) Mechanical linewidth of the resonator extracted from the same experiment (blue line), plotted as a function of the optical frequency. The dashed lines show the optical damping fit with different β values. Solid black lines show limits of $\delta\gamma$ used to extract bounds for β.

shown by lines, include well all these data points.

From Fig. 5b, we see that throughout the temperature range, $|\beta| \lesssim 0.3$, indicating that the photothermal effects are small for these structures, with the input powers used here. Although we do not have a precise knowledge of the input coupling efficiency and so cannot estimate the cavity photon number reliably, we are using large enough powers to give a significant signal-to-noise ratio for the optomechanical experiments. Hence, the small β is promising news for the usage of these structures in quantum applications.

5. Conclusions

In conclusion, we have demonstrated a method to quantify the photothermal β parameter with aid of thermal transport simulations. The method should be easily applicable to other geometries. Our example resonator works deep in the non-resolved sideband limit, which allows us to place strict bounds on β just by comparing the ratio of changes in the mechanical damping rate and mechanical frequency. We demonstrate that the sliced photonic crystal nanobeams show no signs of photothermal effects, even at 4 K temperatures and with optical powers large enough to give a very clear optomechanical signal.

Acknowledgments. The authors wish to thank Amy Navarathna (née van der Hel) and Ewold Verhagen for sample fabrication, Tuomas Puurtinen for help with the phonon simulation code, and Charles Rambo for performing the AFM measurement of sample surface roughness. This project has received funding from the European Research Council (ERC) under the European Union’s Horizon 2020 research and innovation program (Grant Agreement No. 852428) and from Academy of Finland (Grant No. 321416).

Disclosures. The authors declare no conflicts of interest.

Data Availability. Data underlying the results presented in this paper are not publicly available at this time but may be obtained from the authors upon reasonable request.

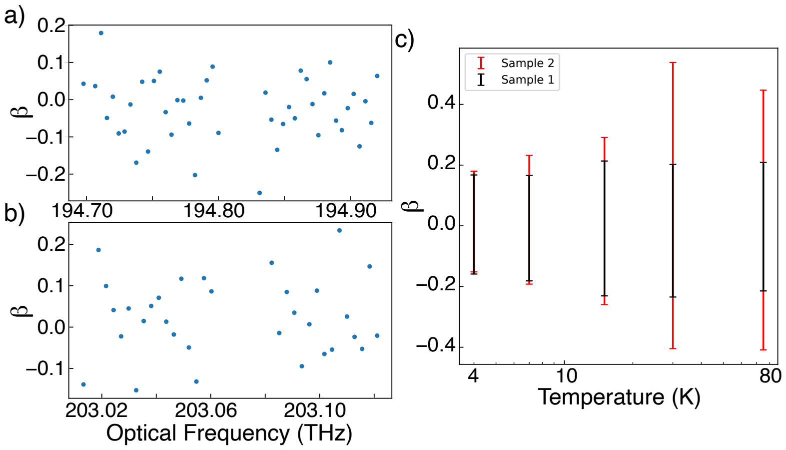

Fig. 5. β values extracted from the ratio of $\delta\omega$ and $\delta\gamma$ values at 4 K for (a) Sample 1 and (b) Sample 2, plotted as a function of optical frequency. Only points where $\delta\omega > 1$ kHz are plotted here. (c) Bounds for β, extracted from the limits of $\delta\omega$ and $\delta\gamma$ (as seen in th solid black lines in Figure 4), plotted as a function of the bath temperature.

Supplemental document. See Supplement 1 for supporting content.

References

1. M. Aspelmeyer, T. J. Kippenberg, and F. Marquardt, “Cavity optomechanics,” Rev. Mod. Phys. **86**, 1391–1452 (2014).
2. A. D. O’Connell, M. Hofheinz, M. Ansmann, *et al.*, “Quantum ground state and single-phonon control of a mechanical resonator,” Nature **464**, 697 (2010).
3. J. Chan, T. P. M. Alegre, A. H. Safavi-Naeini, *et al.*, “Laser cooling of a nanomechanical oscillator into its quantum ground state,” Nature **478**, 89 (2011).
4. J. D. Teufel, T. Donner, D. Li, *et al.*, “Sideband cooling of micromechanical motion to the quantum ground state,” Nature **475**, 359 (2011).
5. R. Riedinger, A. Wallucks, I. Marinković, *et al.*, “Remote quantum entanglement between two micromechanical oscillators,” Nature **556**, 473–477 (2018).
6. C. F. Ockeloen-Korppi, E. Damskägg, J.-M. Pirkkalainen, *et al.*, “Stabilized entanglement of massive mechanical oscillators,” Nature **556**, 478–482 (2018).
7. C. Degen, F. Reinhard, and P. Cappellaro, “Quantum sensing,” Rev. Mod. Phys. **89**, 035002 (2017).
8. A. Laucht, F. Hohls, N. Ubbelohde, *et al.*, “Roadmap on quantum nanotechnologies,” Nanotechnology **32**, 162003 (2021).
9. S. Barzanjeh, A. Xuereb, S. Gröblacher, *et al.*, “Optomechanics for quantum technologies,” Nat. Phys. **18**, 15–24 (2022).
10. N. J. Lambert, A. Rueda, F. Sedlmeir, and H. G. L. Schwefel, “Coherent Conversion Between Microwave and Optical Photons—An Overview of Physical Implementations,” Adv. Quantum Technol. **3**, 1900077 (2020).
11. K. Stannigel, P. Rabl, A. S. Sørensen, *et al.*, “Optomechanical transducers for quantum-information processing,” Phys. Rev. A **84**, 042341 (2011).
12. C. H. Metzger and K. Karrai, “Cavity cooling of a microlever,” Nature **432**, 1002–1005 (2004).
13. C. Metzger, M. Ludwig, C. Neuenhahn, *et al.*, “Self-Induced Oscillations in an Optomechanical System Driven by Bolometric Backaction,” Phys. Rev. Lett. **101**, 133903 (2008).
14. R. A. Barton, I. R. Storch, V. P. Adiga, *et al.*, “Photothermal Self-Oscillation and Laser Cooling of Graphene Optomechanical Systems,” Nano Lett. **12**, 4681–4686 (2012).
15. G. I. Harris, D. L. McAuslan, E. Sheridan, *et al.*, “Laser cooling and control of excitations in superfluid helium,” Nat. Phys. **12**, 788–793 (2016).
16. H. Fu, C. Liu, Y. Liu, *et al.*, “Selective photothermal self-excitation of mechanical modes of a micro-cantilever for force microscopy,” Appl. Phys. Lett. **99**, 173501 (2011).
17. M. Abdi and A. R. Bahrampour, “Improving the optomechanical entanglement and cooling by photothermal force,” Phys. Rev. A **85**, 063839 (2012).

18. D. J. Wilson, V. Sudhir, N. Piro, *et al.*, "Measurement-based control of a mechanical oscillator at its thermal decoherence rate," Nature **524**, 325–329 (2015).
19. M. Rossi, D. Mason, J. Chen, *et al.*, "Measurement-based quantum control of mechanical motion," Nature **563**, 53–58 (2018).
20. M. R. Vanner, I. Pikovski, G. D. Cole, *et al.*, "Pulsed quantum optomechanics," Proc. National Acad. Sci. **108**, 16182–16187 (2011).
21. M. R. Vanner, J. Hofer, G. D. Cole, and M. Aspelmeyer, "Cooling-by-measurement and mechanical state tomography via pulsed optomechanics," Nat. Commun. **4**, 2295 (2013).
22. J. T. Muhonen, G. R. La Gala, R. Leijssen, and E. Verhagen, "State preparation and tomography of a nanomechanical resonator with fast light pulses," Phys. Rev. Lett. **123**, 113601 (2019).
23. R. Leijssen and E. Verhagen, "Strong optomechanical interactions in a sliced photonic crystal nanobeam," Sci. Reports **5**, 15974 (2015).
24. R. Leijssen, G. R. La Gala, L. Freisem, *et al.*, "Nonlinear cavity optomechanics with nanomechanical thermal fluctuations," Nat. Commun. **8**, ncomms16024 (2017).
25. J. Restrepo, J. Gabelli, C. Ciuti, and I. Favero, "Classical and quantum theory of photothermal cavity cooling of a mechanical oscillator," Comptes Rendus Physique **12**, 860–870 (2011).
26. A. G. Primo, C. M. Kersul, R. Benevides, *et al.*, "Accurate modeling and characterization of photothermal forces in optomechanics," APL Photonics **6**, 086101 (2021).
27. C. Metzger, I. Favero, A. Ortlieb, and K. Karrai, "Optical self cooling of a deformable Fabry-Perot cavity in the classical limit," Phys. Rev. B **78**, 035309 (2008).
28. B. D. Hauer, T. J. Clark, P. H. Kim, *et al.*, "Dueling dynamical backaction in a cryogenic optomechanical cavity," Phys. Rev. A **99**, 053803 (2019).
29. G. Jourdan, F. Comin, and J. Chevrier, "Mechanical Mode Dependence of Bolometric Backaction in an Atomic Force Microscopy Microlever," Phys. Rev. Lett. **101**, 133904 (2008).
30. M. Hossein-Zadeh and K. J. Vahala, "An Optomechanical Oscillator on a Silicon Chip," IEEE J. Sel. Top. Quantum Electron. **16**, 276–287 (2010).
31. E. Gil-Santos, D. Ramos, V. Pini, *et al.*, "Optical back-action in silicon nanowire resonators: bolometric versus radiation pressure effects," New J. Phys. **15**, 035001 (2013).
32. H. Casimir, "Note on the conduction of heat in crystals," Physica **5**, 495–500 (1938).
33. M. Maldovan, "Transition between ballistic and diffusive heat transport regimes in silicon materials," Appl. Phys. Lett. **101**, 113110 (2012).
34. O. Bourgeois, D. Tainoff, A. Tavakoli, *et al.*, "Reduction of phonon mean free path: From low-temperature physics to room temperature applications in thermoelectricity," Comptes Rendus. Physique **17**, 1154–1160 (2016).
35. J. S. Heron, T. Fournier, N. Mingo, and O. Bourgeois, "Mesoscopic Size Effects on the Thermal Conductance of Silicon Nanowire," Nano Lett. **9**, 1861–1865 (2009).
36. T. Puurtinen, "Monte carlo phonon ray tracing simulator for 3d geometries," `https://gitlab.com/nanopnc/phonon_rt` (2023).
37. Y. Tian, T. A. Puurtinen, Z. Geng, and I. J. Maasilta, "Minimizing Coherent Thermal Conductance by Controlling the Periodicity of Two-Dimensional Phononic Crystals," Phys. Rev. Appl. **12**, 014008 (2019).
38. T. Klitsner and R. O. Pohl, "Phonon scattering at silicon crystal surfaces," Phys. Rev. B **36**, 6551–6565 (1987).
39. G. R. La Gala, A. S. Kumar, R. Leijssen, *et al.*, "Quadrature-Averaged Homodyne Detection for Estimating Cavity Parameters," Phys. Rev. Appl. **19**, 064006 (2023).

Supplemental document for article ”Thermal relaxation time and photothermal optomechanical force in sliced photonic crystal silicon nanobeams”

Cliona Shakespeare,[1] Arvind S. Kumar,[1] and Juha T. Muhonen[1]

[1]*Department of Physics and Nanoscience Center, University of Jyväskylä,*
P.O. Box 35, FI-40014 University of Jyväskylä, Finland

(Dated: June 25, 2024)

PHONON SIMULATIONS

In our plot of τ versus specularity (main article), we set a maximum specularity of 0.99. This is because at higher specularities, the fundamental assumption we make when fitting for τ — that the number of phonons still in the structure decays exponentially — breaks down, as shown in Figure S1. This is potentially due to the diameter mismatch and angling of the teeth ”trapping” the phonons in a tooth, or, once they have left the tooth through which they enter, preventing them from entering other teeth due to geometrical limitations and thus reducing the effective volume of the structure. (Imagine an arrowhead where the phonons arrive from the arrow shaft and exit through the point of the arrow. If the slopes of the arrowhead are at such an angle that phonons can only specularly reflect towards the point, then at $s = 1$ the phonons will never be found in the sections of the arrowhead ”behind” the entry point. On the other hand, diffuse reflection off the side walls at $s < 1$ will enable the phonons to reach the full volume of the arrowhead.)

Ziman relation

In addition to investigating the effect of the surface specularity on τ, we compared these results to the trend given the Ziman formula. To do that, we first converted each simulated τ value to an effective mean free path Λ, according to Equation S1

$$\Lambda = \frac{3l^2}{\pi^2 c_s \tau} \tag{S1}$$

We then declare that the value of Λ for $s = 0$ is the Casimir mean free path Λ_{cas} and use Equation S2 [1] to acquire the Ziman projection for the effect of small increases in specularity on Λ.

$$\Lambda_{\text{zim}} = \frac{1+s}{1-s}\Lambda_{\text{cas}} \tag{S2}$$

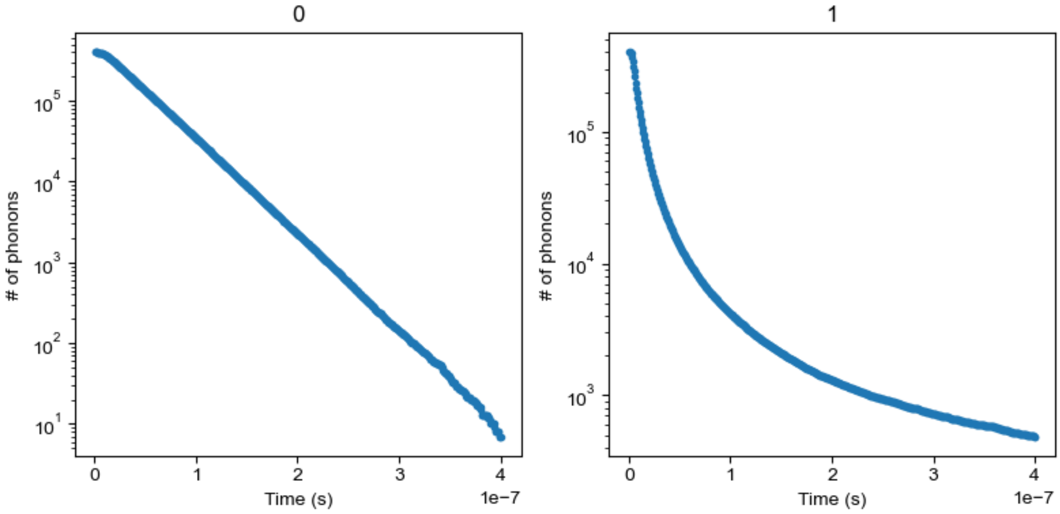

FIG. S1. The number of phonons still in the structure as a function of time for the specularities 0 and 1, plotted on a logarithmic y-axis. Notice the sharper than exponential decay when $s = 1$.

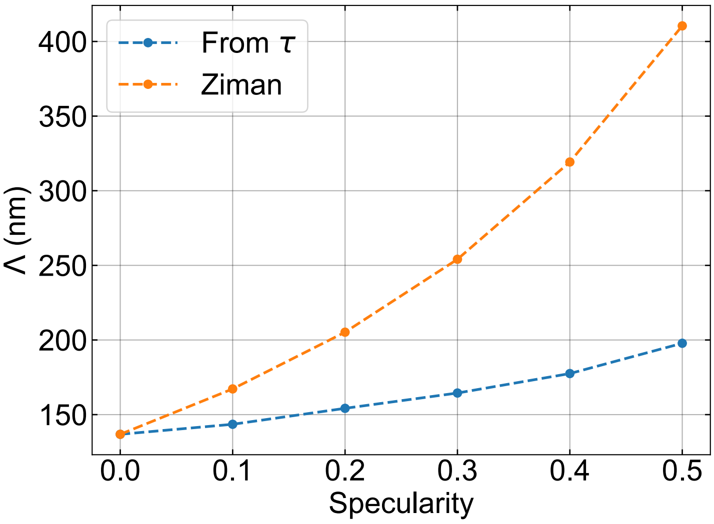

FIG. S2. A comparison of the back-calculated Λ (from τ via Equation S1) and the Ziman projection of the growth in Λ at small increases of specularity.

However, as we can see in Figure S2, the Ziman prediction is not a very good match for our simulated data. This is probably due to the shape of our structure, with dramatic changes in cross-sectional area, retarding the rate of growth in Λ.

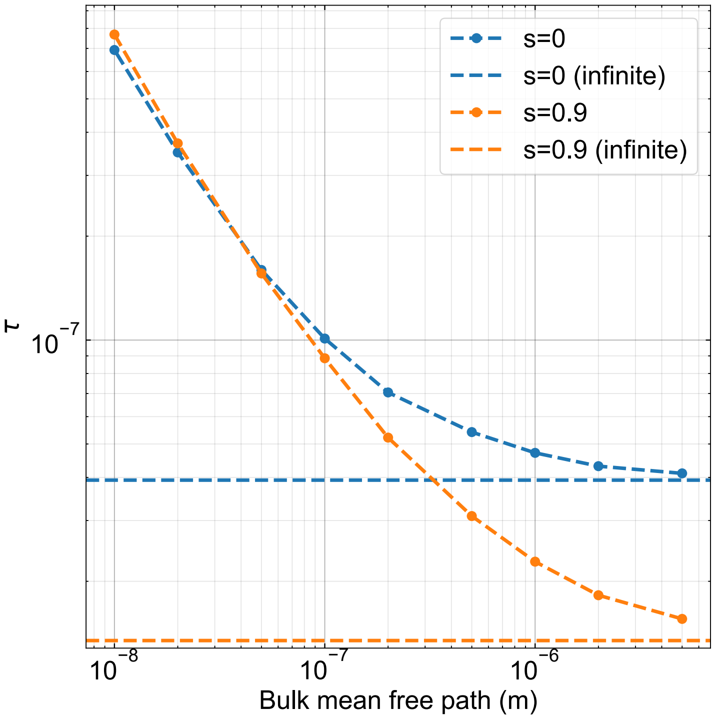

FIG. S3. The effect of the bulk mean free path Λ_B on τ at two different specularities. The horizontal dashed lines represent the infinite bulk mean free path values.

Effects of bulk mean free path

We additionally investigated the effect of the bulk mean free path Λ_B (average distance between scattering events not associated with boundary collisions) on the thermal decay rate τ at two different specularities: 0 (wholly diffusive) and 0.9 (mostly specular). The higher specularity was chosen as 0.9, rather than 1, due to the aforementioned issues associated with wholly specular reflection meaning that an infinite bulk MFP τ value was not available for a specularity of 1.

The bulk MFP value depends on the presence of scatterers in the material. Potential scatterers present in our samples include impurity atoms, dislocations, and other phonons; as the temperature increases, the amount of phonon-phonon scattering increases, so that a decrease in bulk MFP corresponds to an increase in temperature.

As seen in Figure S3, the effect of internal scattering is to increase the time phonons spend in the structure. As expected, once the bulk scattering begins to dominate over the boundary collision scattering (or lack thereof), the two curves converge. Surface roughness thus matters less when phonon transport begins to shift from ballistic to diffusive.

However, while the phonon bulk mean free path Λ_B decreases with temperature, it is not a single

(a) Sample 1

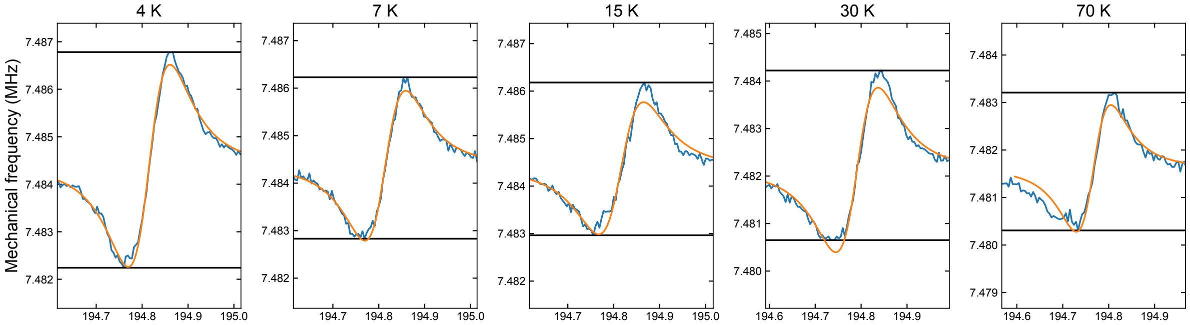

(b) Sample 2

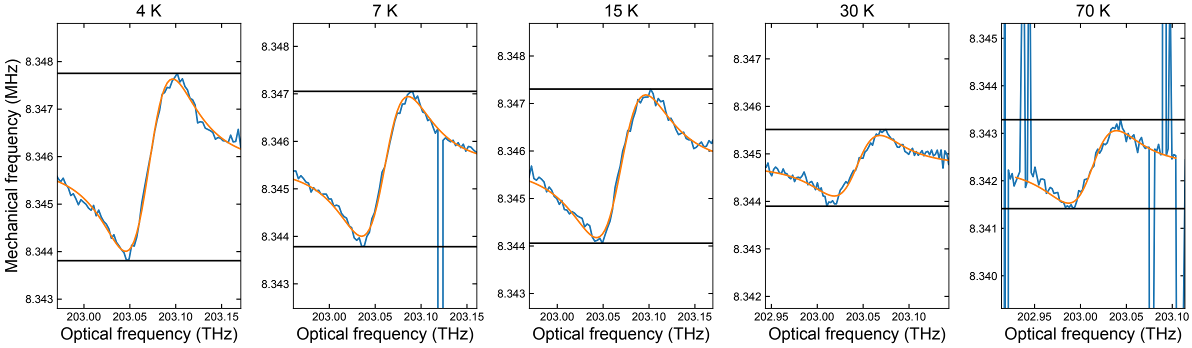

FIG. S4. The optical spring data (blue) and the $\beta = 0$ fit (orange) for both samples at temperatures of T $\leq$ 70K.

value, but rather a density distribution that can be calculated from first principles [2]. At 100 K, 50% of thermal conduction comes from phonons with a bulk mean free path above 4 µm; for for 200 K, the value is 500 nm and for 300K, 200 nm [2]. Using these 50% values as an approximation and approximating the 150 K MFP as the average of 100 K and 200 K (MFP 2 µm, for which τ is 43.1 ns) and 275 K and 295 K as 300 K (70.5 ns).

These values could be used to perform an equivalent fit for β. At higher temperatures, however, the optomechanical nonlinearity of this type of resonator increases [3], so that the linearization we have performed to receive the equations for $\delta\omega_m$ and $\delta\gamma$ is not necessarily valid. As such, the shape of the fits is more uncertain and we are unable to give a confident estimate for β.

OPTOMECHANICAL MEASUREMENTS

For the sake of completeness, we present in Figures S4 and S5 the extracted optical spring and optomechanical damping for both samples at the temperatures used in the main article.

(a) Sample 1

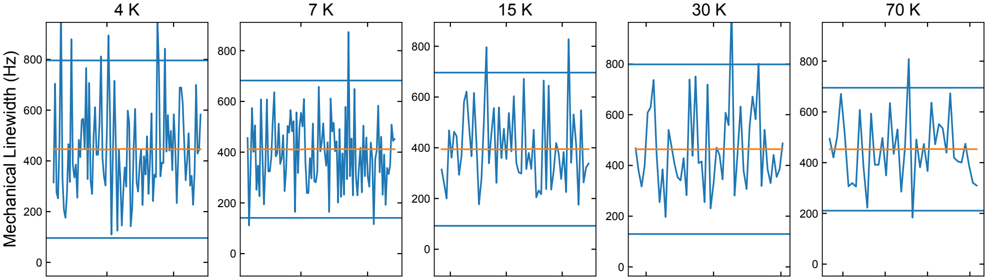

(b) Sample 2

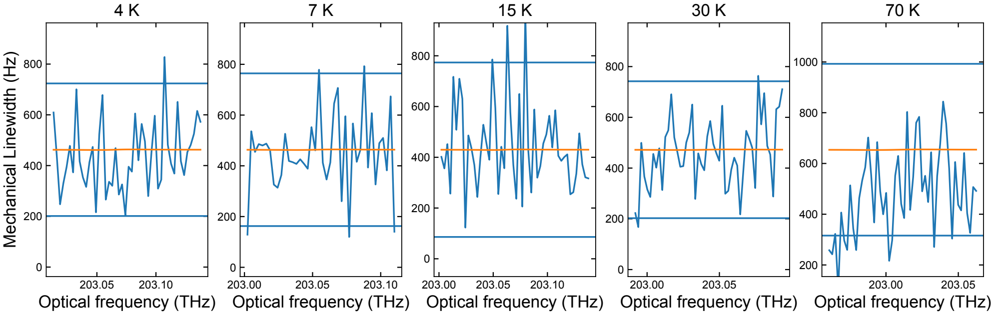

FIG. S5. The optical damping data (blue) and the $\beta = 0$ fit (orange) for both samples at temperatures of T $\leq$ 70K.

[1] O. Bourgeois, D. Tainoff, A. Tavakoli, Y. Liu, C. Blanc, M. Boukhari, A. Barski, and E. Hadji, Reduction of phonon mean free path: From low-temperature physics to room temperature applications in thermoelectricity, Comptes Rendus. Physique **17**, 1154 (2016).

[2] J. Garg, *Thermal conductivity from first-principles in bulk, disordered, and nanostructured materials*, Thesis, Massachusetts Institute of Technology (2011), accepted: 2011-08-18T19:12:49Z.

[3] R. Leijssen, G. R. La Gala, L. Freisem, J. T. Muhonen, and E. Verhagen, Nonlinear cavity optomechanics with nanomechanical thermal fluctuations, Nature Communications **8**, ncomms16024 (2017).

PIII

OPTOMECHANICAL QUANTUM BUS FOR DONOR SPINS IN SILICON

by

Henri Lyyra, Cliona Shakespeare, Simeoni Ahopelto, Teemu Loippo, Reetu Inkila, Pyry Runko, and Juha Muhonen

Manuscript (2024).

Request a copy from author.